Boiling Heat Transfer Characteristics of Steam Generator U-Tube Fouling Deposits

by

Jennifer L. Uhle

B.S. Nuclear Engineering
Massachusetts Institute of Technology, 1991

Submitted to the Department of Nuclear Engineering in Partial Fulfillment of the Requirements for the Degree of
Doctor of Philosophy

at the

Massachusetts Institute of Technology

February 1997

Signature of Author:_____
Department of Nuclear Engineering
October 16, 1996

Certified by:_____
Ronald M. Latanision
Professor of Materials Sciences and Engineering
Thesis Supervisor

Certified by:_____
Neil E. Todreas
Professor of Nuclear Engineering
Thesis Supervisor

Accepted by:_____
Jeffrey P. Friedberg
Professor of Nuclear Engineering
Chairman, Committee for Graduate Studies

Boiling Heat Transfer Characteristics of Steam Generator U-Tube Fouling Deposits

by

Jennifer L. Uhle

Submitted to the Department of Nuclear Engineering
on October 15, 1996 in Partial Fulfillment of the
Requirements for the Degree of Doctor of Philosophy in
Nuclear Engineering

ABSTRACT

The boiling heat transfer characteristics of steam generator u-tube fouling deposits were identified by developing a boiling heat transfer model and determining its accuracy through the comparison of calculated and experimental results. Magnetite deposits were fabricated in the laboratory and were characterized using a variety of techniques. Heat transfer measurements were then taken, so that the effect of deposit parameters, including pore size distribution, porosity, permeability and thickness, as well as the effect of mass flux, heat flux and steam quality were investigated. The model predictions were consistent with the experimental results, differing by an average of ±17.5%.

Over the range of parameters studied, pore size distribution dominated the deposit heat transfer. It was found that some fabricated deposits improved the heat transfer of the u-tubes, whereas others hindered it. The data were consistent with that of fouled u-tubes pulled from CANDU steam generators. The conditions of the heat transfer measurements and the fabricated deposits were similar to those of US and Canadian steam generators. Therefore, the conclusions drawn in this study are presumed to apply to the steam generators used in the Canadian and US industries.

Thesis Supervisor: Ronald Latanision
Title: Professor of Materials Science and Engineering

Acknowledgments

This work was sponsored by the US Nuclear Regulatory Commission Graduate Fellowship Program and the CANDU Owners Group. All laboratory work was performed at Atomic Energy of Canada, Limited (AECL), Chalk River, under the technical guidance of Dr. Carl Turner, Head of the Fouling Section, Heat Exchanger Technology Branch. The magnetite and deposits were fabricated with the help of Ms. Pamela Lavoie. Mr. Michel Brideau performed the heat transfer measurements, supervised by Mr. Stan Klimas. The AECL staff provided invaluable support throughout this collaborative effort. The MIT thesis committee was comprised of Professor Ronald Latanision, thesis supervisor, Professor Neil Todreas, thesis reader, Professors Ronald Ballinger, Peter Griffith and John Meyer.

Dedication

For Mom, Dad, Maria, Eric and Scooby, your support made this whole process bearable. I love you very much. For Professor Norm Rasmussen, who inspired me to attempt this goal. Most especially for my husband, Eric, meeting you put all of this in perspective. Thank you.

Table of Contents

List of Figures

List of Tables

Nomenclature

A	cross-sectional area [m^2]
C	coefficient of permeability
Ca	capillary number
c_{pl}	specific heat of the liquid [J/kg-K]
D	hydraulic diameter [m]
D_s	diameter of the nucleation site [m]
f_{lo}	liquid only friction factor
$f(r)$	incremental pore size distribution [m^{-1}]
F	incremental pore size distribution relation [m^2]
$F(X_{tt})$	Martinelli parameter relation for Chen correlation
g_c	gravitational constant [m/s^2]
G	mass flux [kg/m^2-s]
h	heat transfer coefficient [W/m^2-K]
h_c	Chen heat transfer coefficient [W/m^2-k]
h_{fg}	latent heat of vaporization [J/kg]
h_{mac}	macroscopic component of the Chen correlation [J/kg]
h_{mic}	microscopic component of the Chen correlation [J/kg]
k_d	thermal conductivity of the deposit [W/m-K]
k_l	thermal conductivity of the liquid [W/m-K]
k_m	thermal conductivity of the magnetite [W/m-K]
k_v	thermal conductivity of the vapor [W/m-K]
K	permeability [m^2]
K_l	permeability of liquid [m^2]
K_v	permeability of vapor [m^2]
L	length of ID setup [m]
M	molarity [mol/l]
P_b	pressure of the bulk flow [Pa]
P_c	capillary pressure [Pa]
P_l	liquid pressure [Pa]
P_s	saturation pressure [Pa]
P_v	vapor pressure [Pa]
Pr_l	Prandtl number of the liquid
q''	heat flux [W/m^2]
q'''	volumetric heat rate [W/m^3]
Q	volumetric flow rate [kg/m^3-s]
r	pore radius [m]
r_2	Thom correlation coefficient for loss due to acceleration
r_3	Thom correlation coefficient for loss due to friction
r_4	Thom correlation coefficient for loss due to gravity
r_i	u-tube inner radius [m]
r_m	thermocouple midpoint location [m]
r_{max}	maximum pore radius [m]
r_{min}	minimum pore radius [m]

r_o	u-tube outer radius [m]
r_{ti}	thermocouple inner radius location [m]
r_{to}	thermocouple outer radius location [m]
$\Re$	gas constant
R^*	radius of liquid/vapor boundary [m]
Re_l	Reynolds number of the liquid
Re_{tp}	two-phase Reynolds number
S	suppression factor
t_d	deposit thickness [m]
T_b	bulk temperature [°C]
T_d	deposit temperature [°C]
T_s	saturation temperature [°C]
T_w	wall temperature [°C]
v_l	liquid velocity [m/s]
v_v	vapor velocity [m/s]
x	position [m]
x_v	vapor quality
X_{tt}	Martinelli parameter

Greek

α_{ph}	heat transfer coefficient at phase change [W/m^2-K]
α^v_{vol}	volumetric heat transfer coefficient [W/m^3-K]
β	angle of the ID setup with the vertical [°]
δ	radius of interaction of surface tension [m]
Δh_C	change in heat transfer coefficient of the clean tube [W/m^2-K]
Δh_F	change in heat transfer coefficient of the fouled tube [W/m^2-K]
θ	contact angle [°]
μ_l	viscosity of liquid [Pa-s]
μ_v	viscosity of vapor [Pa-s]
ν_l	kinematic viscosity of liquid [m^2/s]
ν_v	kinematic viscosity of vapor [m^2/s]
Π	porosity
σ	surface tension [N/m]
φ	cumulative pore size distribution

1 INTRODUCTION

1.1 Goal of Research

The goal of this study was to identify the boiling heat transfer characteristics of steam generator u-tube fouling deposits by developing a boiling heat transfer model and determining its accuracy through the comparison of calculated results to experimental values. It was found that some fabricated deposits improved the heat transfer of the u-tubes, whereas other hindered it. The data were consistent with that of fouled u-tubes pulled from CANDU steam generators.

A FORTRAN code was created to solve the model equations, yielding the temperature drop across the deposit to the steam generator secondary side bulk flow. The result is a function of the secondary side flow conditions, and deposit characteristics Inputs to the code therefore include: bulk flow mass flux, quality, pressure, liquid contact angle, deposit thickness, composition, permeability, porosity, pore size distribution and applied heat flux. The model is presently solved for the experimental conditions of constant heat flux. A listing of the code is given in Appendix A.

There exist a variety of heat transfer models for boiling in porous media, most based on the wick boiling phenomenon [B-2][C-4][J-1][K-1][K-2][K-3][M-1][M-2][M-4][M-5][S-2][S-5]. However, most models lack the incorporation of deposit characteristics. Heat transfer measurements have been performed at Atomic Energy of Canada, Limited (AECL) in Chalk River, Ontario, on fouled u-tubes pulled from a variety of CANDU steam generators. A wide range of results have been obtained [T-4]. For similar deposit thicknesses and composition, the deposits both improved and hindered the heat transfer of the u-tubes. The knowledge of what deposit characteristics govern the heat transfer of a fouled u-tube is required

to determine the impact of fouling on steam generator secondary side thermal hydraulics. If successful, the model can be used in thermal hydraulic codes to determine the steam generator conditions in cases when the u-tubes are fouled. Furthermore, the model calculates the temperature drop across the deposit and yields the vaporization rate at each radial location in the deposit. It therefore can be readily coupled with a mass transfer model to determine the concentration rate of non-volatile species in the deposit, so that hideout and fouling rates can be modeled in detail.

The model can be directly used to estimate the heat transfer coefficient of fouled steam generator u-tubes. The deposit pore size distribution was found to dominate the heat transfer of the deposit, as is described in Chapter 6. Therefore, without detailed deposit characterization, the model can predict the deposit temperature drop by assuming average values of steam generator mass flux, pressure and quality, estimating the deposit composition (the deposit composition affects the heat transfer by determining the thermal conductivity of the deposit skeleton), thickness, porosity and permeability and liquid contact angle and measuring the pore size distribution. It was found that a surface Scanning Electron Microscope (SEM) micrograph of a deposit depicted the pores reasonably well and verified the results obtained with mercury porosimetry. Therefore, a surface SEM micrograph can be used to quickly estimate the pore size distribution, although mercury porosimetry is strongly recommended.

When estimating the deposit characteristics, it is suggested that the following values be assumed: porosity of 50%, permeability of 5E-15 m^2, a composition comprised of 100% magnetite (30% copper content is found in deposits of systems with brass condensers), thickness measuring 25 μm and a contact angle of 30°.

1.2 Research Plan

1.2.1 Model Development

The model is one-dimensional, implying that the heat flux is transferred perpendicular to the axis of the u-tube. The temperature of the deposit varies in this direction only. Steady conditions of evaporation exist in the deposit. Therefore, the liquid/vapor interfaces are constant, and the mass flux of liquid into the deposit is equal to the mass flux of vapor exiting. Capillary forces drive the fluid flow. Wick boiling and the characteristics of the deposit determine the amount and location of vaporization in the deposit, based on work done by Kovalev [K-1][K-2][K-3][S-4]. The remainder of the applied heat flux that is not vaporized is then transferred to the steam generator secondary side bulk flow (with mass flux, G, and quality, x_v) at the deposit/bulk flow interface. The heat transfer at the interface is found from the Chen correlation [C-2]. The model calculates the temperature drop across the deposit to the bulk flow. Figure 1.1 depicts the arrangement, where q", G and x_v represent the heat flux transferred from the primary to the secondary side, the mass flux and steam quality, respectively. The bulk flow is assumed parallel to the u-tube, so that the model applies the vertical free-span regions of the steam generator.

1.2.2 OD Deposit Fabrication and Characterization

Simulated steam generator u-tube fouling deposits were prepared at AECL, Chalk River. The deposits were fabricated with magnetite prepared in the laboratory and sintered onto the outside of I-600 u-tube sections, according to procedures developed at AECL [L-2][T-2]. Throughout the text, they are referred to as OD (outside diameter) deposits. An attempt was made to fabricate deposits that varied in characteristics with an aim to identify those characteristics that govern boiling heat transfer. The deposits were well characterized by a variety of techniques and

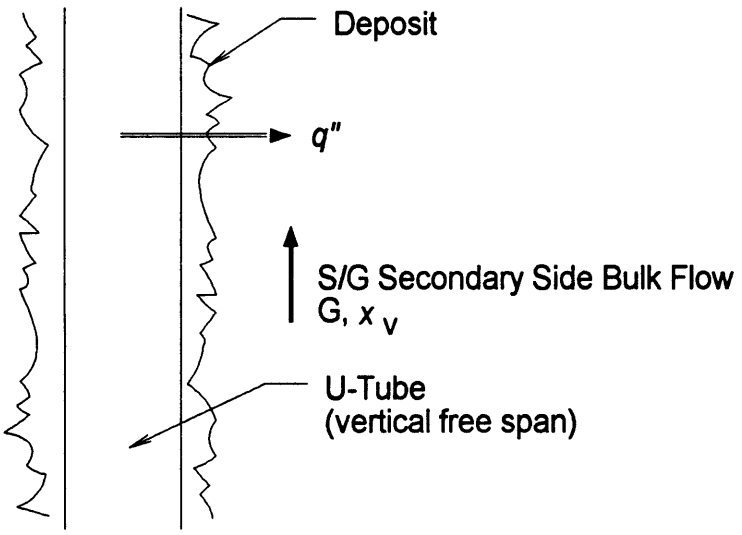

Figure 1.1: The Modeled System Arrangement

were seemingly similar to deposits found on CANDU u-tubes [T-6]. The water/air/magnetite contact angle was also measured.

1.2.3 Experimentation

The temperature drop across the OD deposits under boiling conditions at heat fluxes ranging from 4.92E4 to 7.37E4 W/m^2 were measured with 5% quality and mass fluxes of 5, 125 and 250 kg/m^2-s at a pressure of 4.4 MPa. Subcooled measurements were also taken to determine the thermal conductivity of the deposit, a parameter used in the model.

It was not convenient to operate the OD setup at higher quality levels. Therefore, measurements were done on an ID (inner diameter) deposit to determine the effects of quality and mass flux on boiling heat transfer. The qualities ranged from negative values to 30% along the length of the setup; the mass fluxes were 185 and 273 kg/m^2-s; the pressure was set at 4.9 MPa, and the heat flux was 2.1E5 W/m^2.

1.2.4 Comparison of Experimental and Theoretical Results

The results of the OD experiments were compared to those predicted by the model to determine the model's accuracy. In addition, the effects of the deposit characteristics, heat flux, mass flux and quality on the boiling heat transfer found by both the ID and OD experiments were compared to those determined by the model.

1.3 Applicability of the Study Results

Typical recirculating steam generators in the US industry operate at 7 MPa, with qualities ranging from 0 to 25%, mass fluxes and heat fluxes on the order of 300 kg/m^2-s and 1E5 W/m^2, respectively. CANDU steam generators operate with the same quality range and heat flux but at 5 MPa with mass flux levels of approximately 500 kg/m^2-s [P-1][T-5]. Therefore, the conditions of the experiments were similar to those in US and Canadian steam generators.

In both the ID and OD experiments, the heat transfer loop contained distilled water with 0.001 volume fraction of morpholine. Generally, both the US and Canadian industries use all-volatile chemistry control. Amines such as ammonia or morpholine maintain the pH to desired levels, and hydrazine is used to scavenge oxygen to ensure a reducing rather than an oxidizing environment. The u-tubes are fabricated from either I-800 or I-600. Replacement steam generators contain I-690 u-tubes. Deposits found on the u-tubes of CANDU steam generators are mainly comprised of magnetite and are similar to those produced in this study (in porosity and pore size). The morphology of the CANDU deposits is discussed in Chapter 3. Therefore, the water chemistry and deposits were typical of US and Canadian steam generators.

Since the heat fluxes, mass fluxes, qualities, water chemistry and deposits used in the measurements are generally representative of steam generator conditions, the conclusions drawn in this study apply to the Canadian and US industries.

2 MAGNETITE

2.1 Introduction

Colloidal magnetite was prepared in the laboratory, according to the method outlined by Sugimoto [S-6] and further developed at AECL, Chalk River [L-1][T-1]. The particles produced by this technique are spherical and have a narrow size distribution. The process incorporates the hydrolysis of a ferrous sulphate solution to precipitate $Fe(OH)_2$. Two-thirds of the ferrous ions in the precipitate are then oxidized to produce magnetite (Fe_3O_4) (complete oxidation of the ions would yield maghemite (γ-Fe_2O_3)). The details of the procedure are outlined in section 2.2. The particle size of the magnetite was controlled through variations in reaction stoichiometry and sintering temperature as described in section 2.3.

2.2 Procedure

The reaction must occur with minimal contamination. Therefore, glassware was cleaned with Clarke's solution [C-6].

To inhibit the oxidation of the iron ions, the reaction and the solutions must be de-aerated. Distilled water was de-aerated with high purity argon (Ar). The Ar was bubbled through a glass tube with a fritted end submerged in the water container. The gas flow rate used was 2 l/min for 30 min per litre of water.

The de-aerated distilled water was used to prepare the KOH/KNO_3 solution and $FeSO_4 \cdot 7H_2O$ solution. The molarity (M) and quantity of the solutions are discussed in section 2.3.

A 3 litre, 3-necked round bottom flask was placed into a covered heating mantle. A mechanical stirrer was inserted into one neck. Ar was supplied into another neck through a rubber stopper with an opening for the fritted glass tube. A thermometer was inserted through a rubber stopper which sealed the remaining neck. Therefore, the flask was flushed with Ar.

The stirrer was energized, and the $FeSO_4 \cdot 7H_2O$ solution was added to the flask. Approximately one-half of the KOH/KNO_3 solution was added and mixed thoroughly. Aliquots of the solution were added every five minutes until all the solution was used.

The heating mantle heated the solution after the addition of the solutions was completed. A temperature controller was set to monitor the thermometer temperature at 90 °C. The heating mantle was connected to the temperature controller through a variable transformer. Therefore, the reaction temperature was limited to 90 °C. The solution, now a magnetite suspension, was continuously stirred and heated for two hours to ensure the reaction was complete.

The suspension was allowed to cool and removed from the Ar cover to a 4 litre beaker. A magnet was applied to the underside of the beaker to enhance the settling rate of the particles (magnetite is magnetic). The supernatant was decanted and an equivalent volume of distilled water was added. The washing of the suspension was continued until the conductivity of the supernatant dropped to about 20 μsiemens.

2.3 Control of Particle Size

The goal of this study necessitated control of the magnetite deposit characteristics, including pore size distribution, permeability and porosity. It was thought

improbable that all three could be independently varied. Therefore, the work focused on control of the particle size, which presumably would yield batches of magnetite with varying pore size. Sugimoto found that the magnetite particle size could be controlled with stoichiometry.

The particle size was determined by the excess Fe^{2+} or OH^- ion concentrations. Particles with a mean diameter of approximately 0.4 μm were produced with 0.1 or greater excess Fe^{2+} M, whereas a mean diameter of 0.1 μm was produced with 0.1 or greater excess OH^- M. The largest particles with a mean diameter of 1.0 μm were produced with an excess Fe^{2+} M of approximately 0.01. The particle size distribution was small in each case.

To yield a 0.1 molar excess of OH^-, 1.00 litre of 0.5 M $FeSO_4 \cdot 7H_2O$ solution was added to 1.10 litres of 1.0 M KOH/KNO_3 solution. A molar excess of 0.1 and 0.01 Fe^{2+} were produced by combining 1.20 and 1.02 litres of 0.5 M $FeSO_4 \cdot 7H_2O$ solution, respectively, to 1.00 litre of 1.0 M KOH/KNO_3 solution.

The work of Sugimoto was reproduced in several test runs to validate the control of particle size. Three batches of magnetite were prepared for the fabrication of the deposits. Batch 3 (B3), shown in Figure 2.1, had a mean diameter of 0.4 μm, but was not spherical as expected. The origin of the dendritic structure was unknown. Batch 4 (B4), shown in Figure 2.2, had a mean diameter of 0.1 μm. The shape was not completely spherical but slightly cubic, as expected with excess KOH.

Another batch, B5, was produced having a mean diameter of approximately 1.0 μm. However, the deposits chipped in the heat transfer experiments so that data were not obtained. In an effort to produce another particle size distribution, B4 was sintered at a lower temperature than the other batches. This batch was denoted B4(7). The coating and sintering process is discussed in Chapter 3.

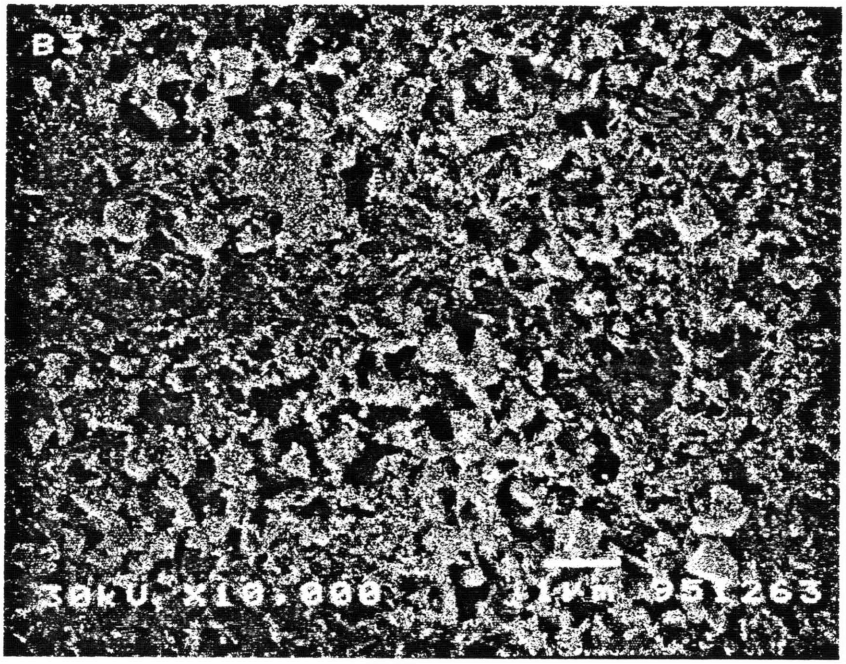

Figure 2.1: SEM Micrograph of B3

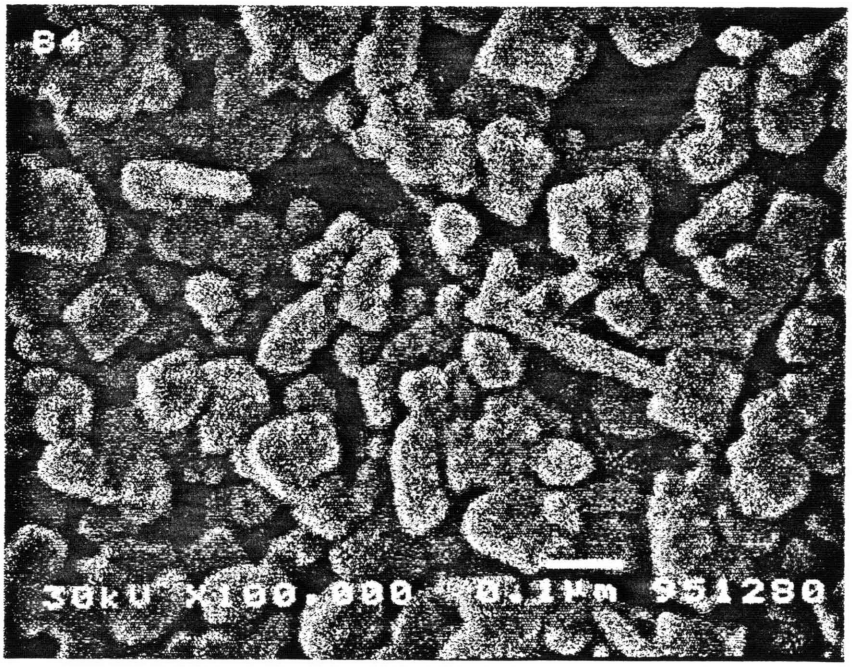

Figure 2.2: SEM Micrograph of B4

3 OD DEPOSIT FABRICATION AND CHARACTERIZATION

3.1 Introduction

Since the goal of the research was to develop and determine the accuracy of a boiling heat transfer model for magnetite deposits that incorporated deposit characteristics, a critical step involved the preparation and characterization of the deposits. This chapter discusses these processes.

The outside of I-600 u-tubes were coated with magnetite according to procedures developed at AECL, Chalk River [L-2][T-2]. The procedure is discussed in section 3.2. The deposits were characterized using a variety of techniques, outlined in section 3.3. The results are summarized in Table 3.1. The deposits are compared to typical CANDU steam generator deposits and sludge in section 3.4.

3.2 OD Deposit Fabrication

In order to determine the effect of deposit thickness, three thicknesses of each batch of magnetite were produced. Therefore, a total of 9, 15 cm sections of I-600 u-tube were cut. The surface of the u-tubes was one factor in determining the adherence of the deposits. Each u-tube was sanded with 240 grit silicon carbide polishing paper and finished with 600 grit. The tubes were then treated with an I-600 etching solution (40 ml glycerol, 10 ml HNO_3, 20 ml HCl) for 2 min and allowed to dry. Methanol was then used to remove any oil from the surface of the u-tubes.

The magnetite colloid was well mixed prior to dipping to preclude the development of chunks in the coating. The colloid was poured into a volumetric

cylinder, placed beneath the dipper (a notched arm connected to the gears of a stepper motor). The thickness of each coat was determined by the dipping speed and the viscosity of the colloid. The viscosity was visually inspected to ensure that it was neither too high nor too low. The speed was set to 1 cm/s for each sample.

Before dipping, the u-tubes were dried. One end of the u-tube was plugged with paraffin to prevent the colloid from coating the inside of the u-tube. Wire was placed through holes drilled into the top of the u-tube and hung onto the dipper arm. The stepper motor was energized to move the u-tube vertically into the magnetite, making sure the sides of the graduated cylinder were avoided. The u-tube was drawn out of the magnetite in the same manner.

The coating was inspected to ensure no running of the colloid was visible, and the u-tube was dried in an oven set to 70 °C. Once dry, the u-tube was hung onto stainless steel rods, placed on supports, and inserted into a furnace. The coating was not touched. Air was purged from the furnace with high purity Ar to prevent oxidation of the magnetite at high temperatures. The coatings were sintered at 800 °C for one full hour after the required temperature was reached.

The deposit thickness was increased by repetitively dipping and sintering a u-tube. Once coated, the u-tube was cut into 2 cm sections to be used for heat transfer measurements and characterization.

3.3 OD Deposit Characterization

3.3.1 Composition

Before using any batch of magnetite, X-ray diffraction (XRD) was used to determine the composition of the colloid. All batches were pure magnetite.

3.3.2 Thickness

Circumferential and axial sections were cut from one 2 cm section of the u-tube and mounted in bacolite. SEM micrographs were produced of the sections to determine thickness and deposit uniformity in the axial and circumferential directions. In all cases, uniform deposits were fabricated. As an example, the thickness SEM micrograph of sample B4-3 is given in Figure 3.1. The results of each sample are given in Table 2.1

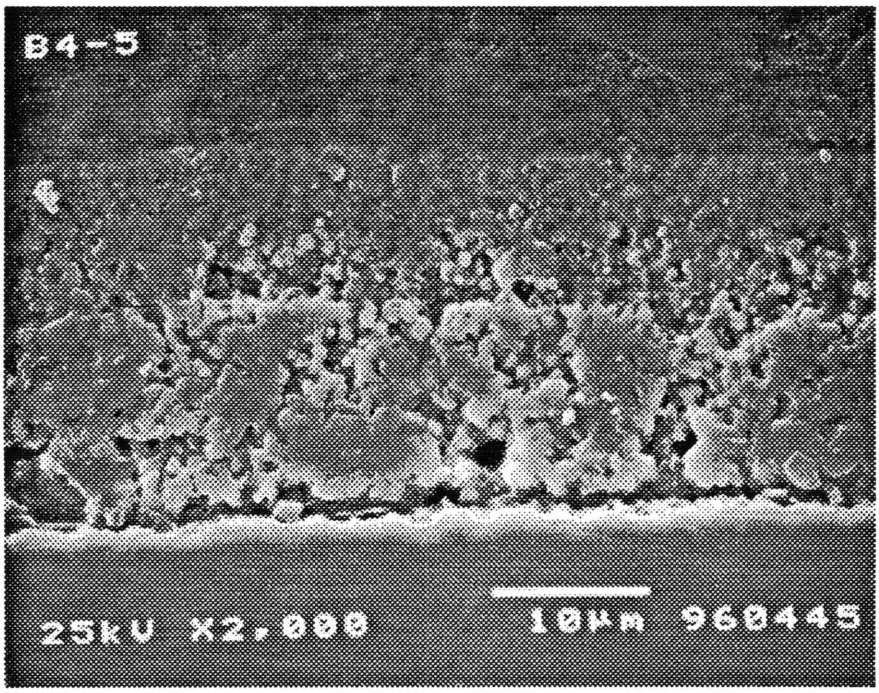

Figure 3.1: Thickness SEM Micrograph of B4-3

3.3.3 Porosity

Porosity is the ratio of the pore volume to that of the sample. To determine the porosity of the coating, some magnetite from each batch was poured into Pyrex boats and given the identical heat treatment as the deposits. This sintered batch sample was analyzed using mercury porosimetry (HgPS) to yield porosity. It was

postulated that each of the three deposits produced per batch of magnetite would have the same porosity.

To verify the results of the HgPS, the loading of each of the coated tubes was determined. The loading (g/m^2) and deposit thickness were used to determine the density of each deposit. The porosity was then determined by dividing the skeletal density of magnetite (5.2 g/cm^3) by the deposit density.

The mass of each deposit was evaluated by subtracting the weight of the u-tube after the deposit was removed from the weight of the coated u-tube. The deposit was removed by soaking the sample in a solution of alkaline permanganate at 70 °C for 15 min followed by modified Clarke's solution for 1 min [C-6]. The deposit was then rubbed with a rubber eraser and completely removed. The procedure did not attack the I-600, as verified by a blank I-600 u-tube section.

The results of both techniques are shown in Table 3.1. The results show relatively good agreement. The porosity of each batch was assumed to be that evaluated by mercury porosimetry [H-1].

3.3.4 Pore Size Distribution

The cumulative pore size distribution represents the percentage of the porous volume comprised of pores with radii less than the given radius. Therefore, the value ranges from 0 to 1 corresponding to the minimum and maximum pore radii in the deposit, respectively. The HgPS run that gave the porosity of the sintered batch sample also yielded the pore size distribution. In an effort to validate the findings, SEM micrographs were taken of the sintered material. Caution should be used when comparing the surface pores visible on SEM micrographs to the HgPS results, which represent a volumetrically averaged distribution [B-5]. However, the SEM micrographs seemed to validate the HgPS data; B3 had the largest pores

on the order of 0.26 μm in radius followed by B4 and B4(7) with radii of approximately 0.23 and 0.20 μm, respectively.

Since the properties measured for the batch samples were applied to the deposits, it was necessary to determine if the magnetite sintered onto the u-tubes reacted similarly to the heat treatment as the batch samples that were sintered in Pyrex boats. This was done by comparing the SEM micrograph of the sintered batch sample to the SEM micrograph of the surface of a representative deposit from each batch. The SEM micrographs were relatively consistent.

The pore size distributions evaluated with HgPS are depicted in Figure 3.2. The SEM micrographs of each sintered batch sample and the surface of a representative deposit from each batch are given in Figures 3.3-3.8. Summary data are listed in Table 3.1.

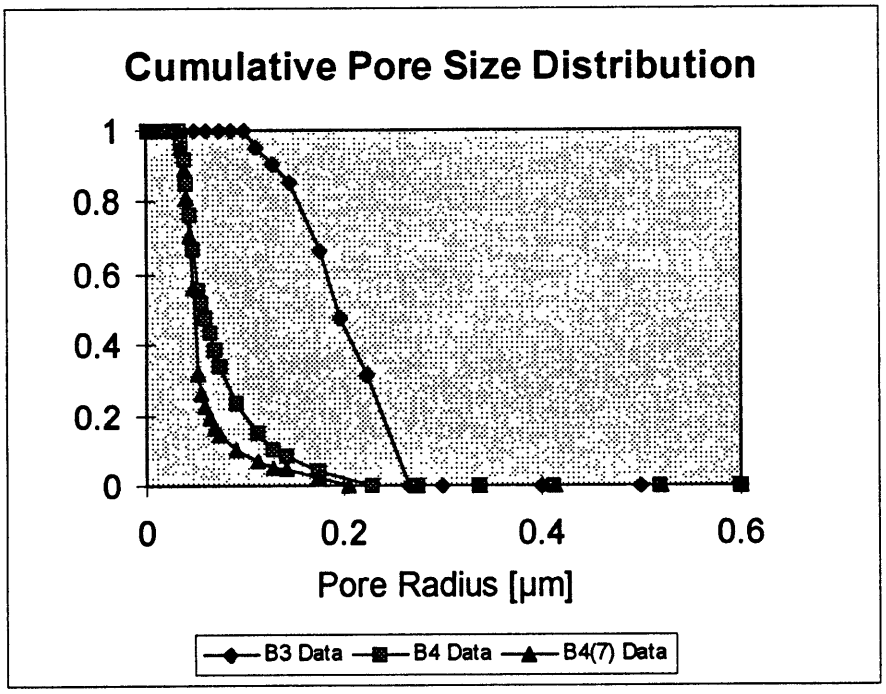

Figure 3.2: Cumulative Pore Size Distribution of Sintered Magnetite Batches

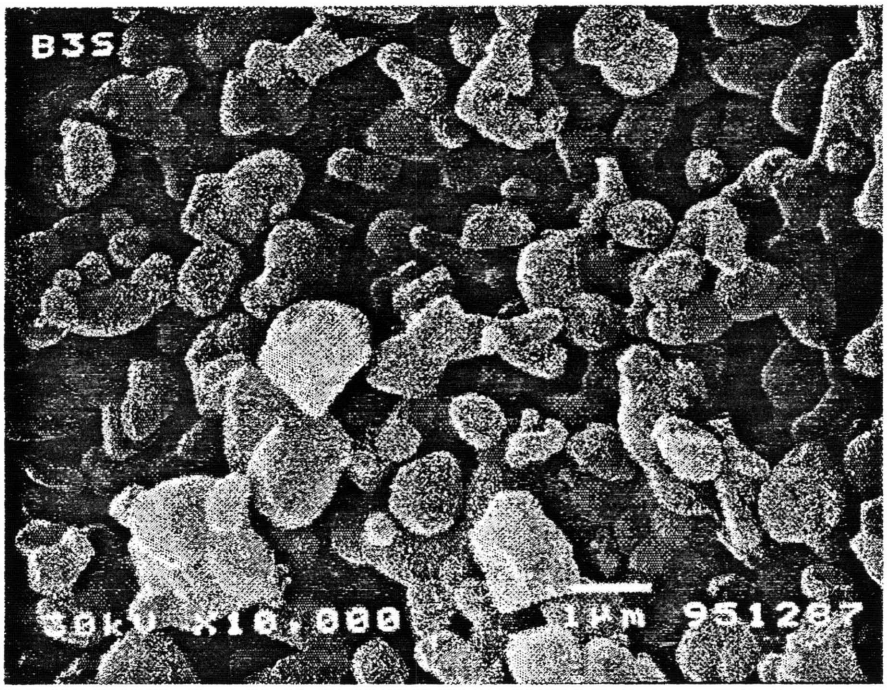

Figure 3.3: SEM Micrograph of Sintered B3

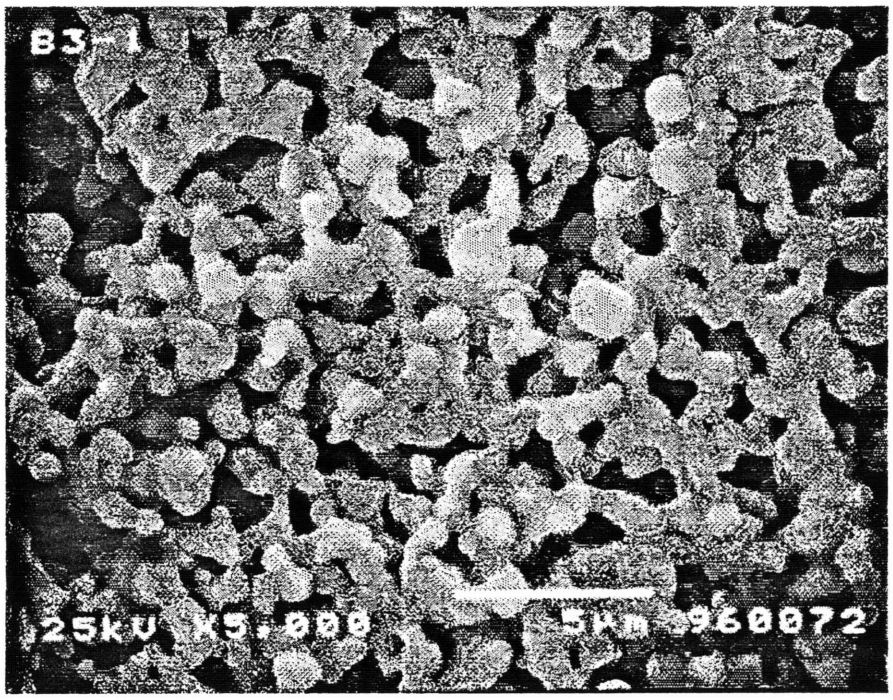

Figure 3.4: SEM Micrograph of B3-1 Surface

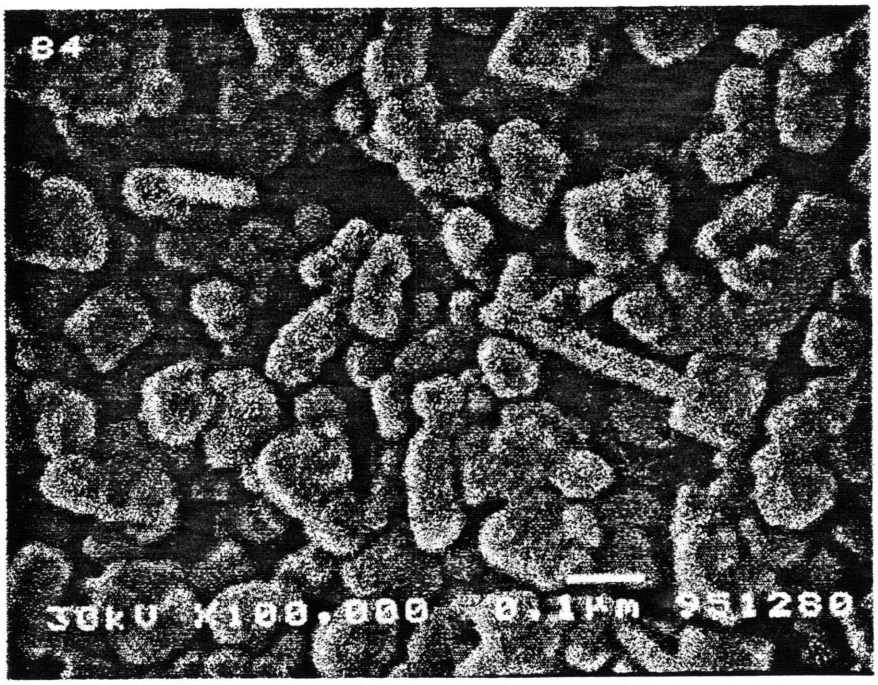

Figure 3.5: SEM Micrograph of Sintered B4

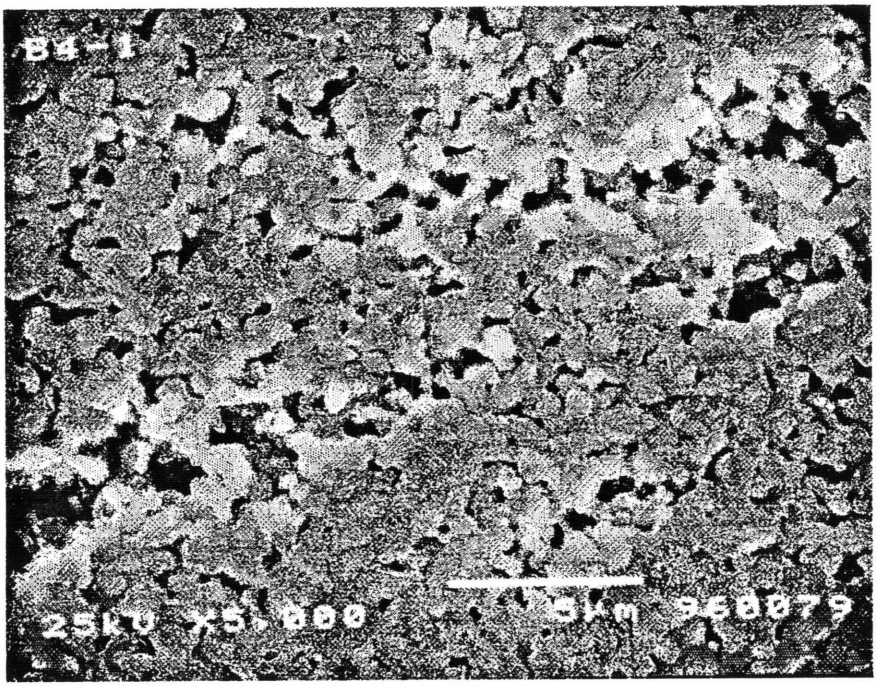

Figure 3.6: SEM Micrograph of B4-1 Surface

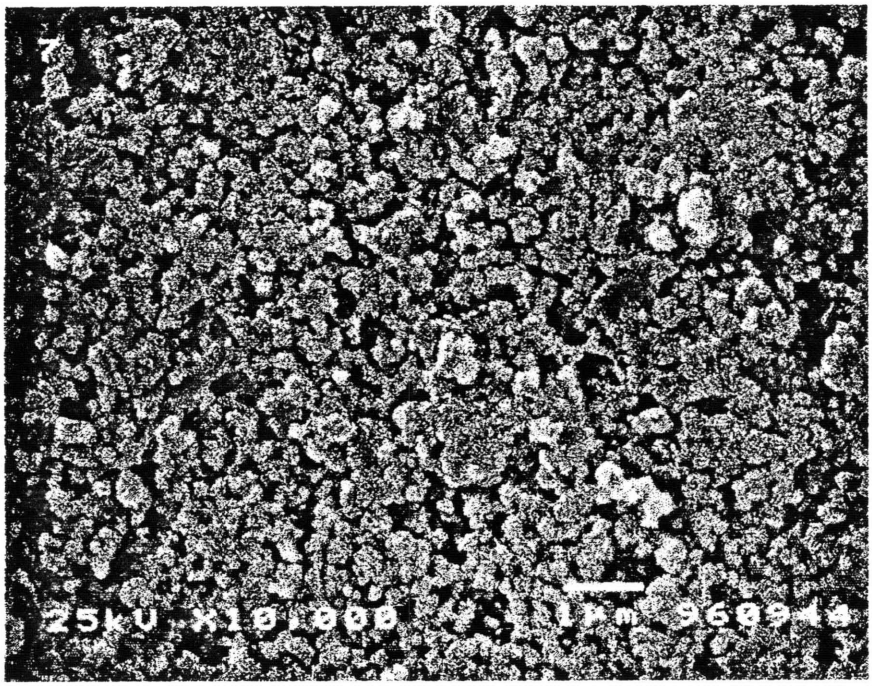

Figure 3.7: SEM Micrograph of Sintered B4(7)

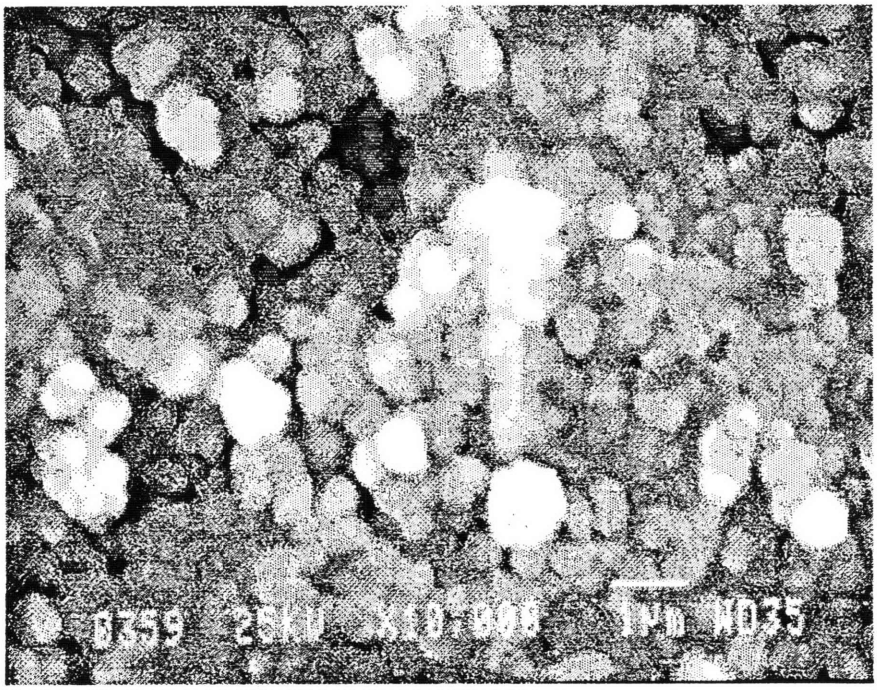

Figure 3.8: SEM Micrograph of B4(7)-3 Surface

3.3.5 Permeability

Permeability, K, is defined by the following equation:

$$Q = \frac{K\Delta PA}{\Delta x \mu}, \tag{3.1}$$

where Q is the volumetric flow rate of an incompressible liquid with viscosity, μ, through a sample with cross-sectional area, A, and length Δx. The pressure drop through the sample is ΔP. K is in units of m^2. Compressibility of the fluid causes Q to depend on pressure. Therefore, when using equation 3.1 with a gas, care must be taken to ensure Q represents the average volumetric flow rate, or the volume flow rate evaluated at the mean pressure. This equation is termed Darcy's Law and only applies to systems where the Reynolds number is less than one [C-7][D-1].

The permeability of the deposits could not be measured directly on the tubes. Therefore, the permeability of each batch was determined by using the respective sintered batch sample. However, the bulk density of the sample was far less than that of the deposit, since the sample was unconsolidated. It was postulated that the permeability of the deposit could be inferred by measuring the permeability of the sample at approximately 10 packing densities and extrapolating the results to the deposit density obtained from HgPS.

To obtain 10 packing densities close to the density of the deposit, the sintered batch sample was finely ground with a mortar and pestal. It was impossible to grind the magnetite to individual particles, so the maximum packing density was approximately 50% of the deposit density.

The setup used to determine the permeability of the sintered batch samples, depicted in Figure 3.9, was comprised of a tank of Ar, a thermocouple, a flow controller and meter, a pressure transducer, a voltmeter and a glass sample

chamber. The chamber included a fitting to connect the pressure transducer upstream of the sample column where the magnetite was packed. The column included both a stationary and a removable glass frit. The removable frit allowed the packing of the magnetite into the column and was held in place by a plastic threaded cap. The cap was open at the top so the gas escaped the chamber to atmosphere. The frits measure 2 mm in thickness, whereas the chamber measured 0.776 cm^3 in volume, 0.95 cm in length and 0.51 cm in radius.

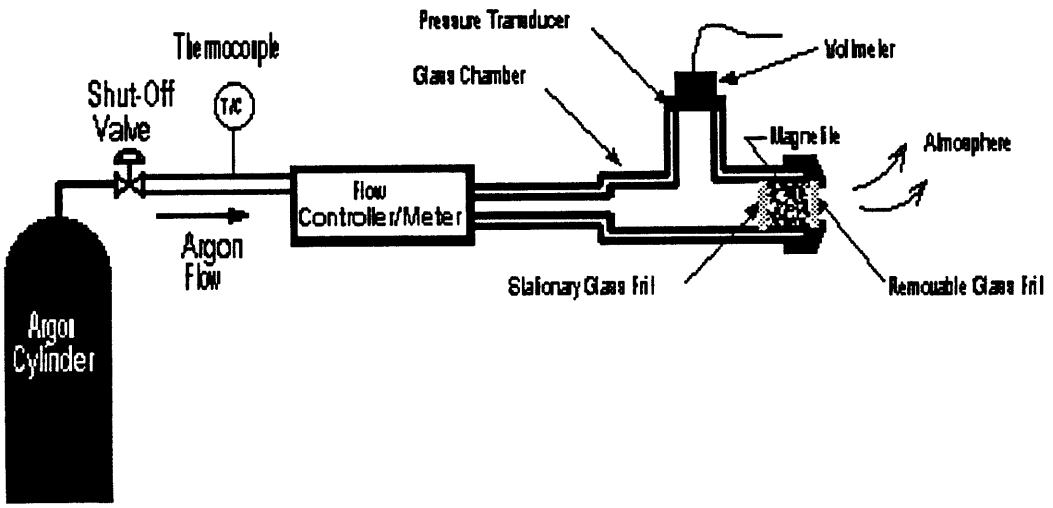

Figure 3.9: Permeability Measurement Setup

In the setup, the Ar flowed through the flow controller to the sample chamber, where the pressure was measured. The gas then flowed through the stationary frit across the magnetite and finally through the removable frit to atmosphere. The temperature of the gas was measured to evaluate the viscosity.

Five flow rates were tested. The flow was controlled, and the pressure was measured upstream of the column. The same flow rates were run again without the sample so that the pressure drop stemming from the glass frits was measured.

The pressure drop across the frits was then subtracted from the sample pressure drop to determine the permeability of the packed magnetite.

The density of the packing was found by weighing the sample and dividing by the chamber volume. The density of the packing was then changed and the procedure repeated. Approximately 10 packing densities were run for each batch of magnetite to determine the dependence of permeability on density. The permeability was then extrapolated to the density of the magnetite deposits found from HgPS.

The results of the permeability measurements are shown in Figures 3.10-3.12. Extrapolation of the B3 data to the deposit density of 3.81 g/cm^3 yielded a value of 6E-16 m^2 for the permeability of the B3 deposits. The value of B4 at a density of 2.81 g/cm^3 and B4(7) at 2.08 g/cm^3 was 4E-16 and 1E-16 m^2, respectively. In each sample, the asymptote was approached at a packing density of approximately 50% of the deposit density. The sample could have been ground finer if the rate of decrease did not diminish appreciably at the maximum packing density achievable.

It was hypothesized that a pellet of magnetite could be formed by sintering the magnetite in a container, extracting the hardened pellet and placing it in a column for measurements. The pellet would have the same density as the deposit formed from the specific batch of magnetite and sintered at the same temperature and the extrapolation technique would not have been necessary. This procedure was not possible because the sintering process only worked for thin layers of magnetite. Thick coats did not sinter as hard as thin coats and were less dense. In addition, if the magnetite was not exposed to the flow of Ar, the water evaporating from the drying colloid would oxidize the magnetite, forming hematite (Fe_2O_3). Therefore, the pellet would differ from the deposit in composition and density.

The results are summarized in Table 3.1.

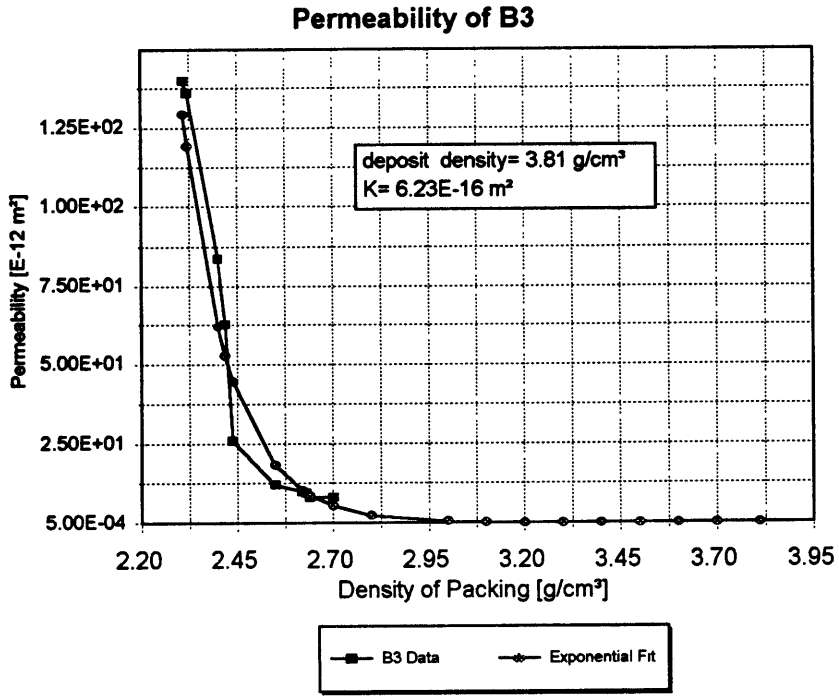

Figure 3.10: The Permeability of B3

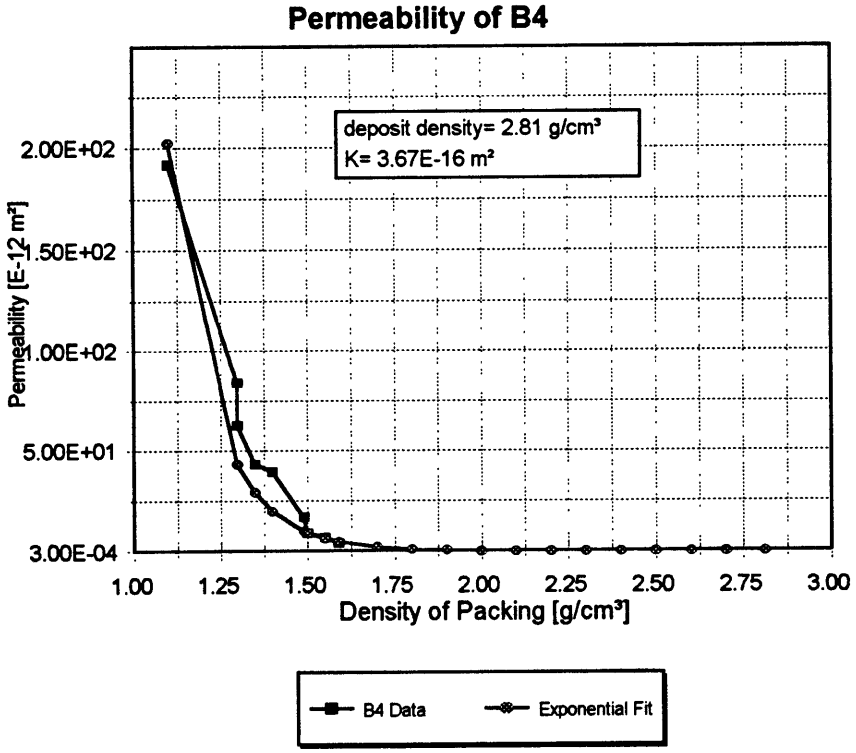

Figure 3.11: The Permeability of B4

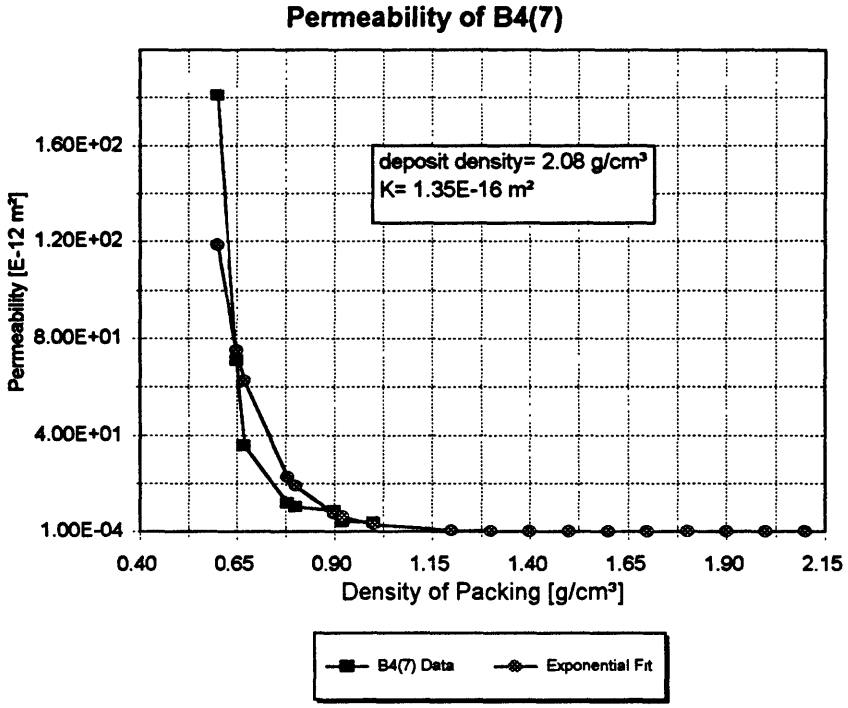

Figure 3.12: The Permeability of B4(7)

3.3.6 Contact Angle

The contact angle of the water/steam/magnetite is a parameter used in the model. The contact angle of water/steam/magnetite is not documented in literature. The heat transfer loop used in the experiments contained distilled water with approximately 0.001 volumetric fraction of morpholine. This solution was used to evaluate the contact angle at room temperature with a simplistic but effective setup [G-2]. Typically, US and Canadian plants use all-volatile secondary side chemistry control. An amine such as morpholine or ammonia is used to control pH and hydrazine is added to scavenge oxygen to establish a reducing rather than oxidizing environment [T-5]. Therefore, since morpholine was added to the fluid when the contact angle was measured, the result most likely applies to steam generator conditions.

Both B3 and B4 were coated onto thin sheets of I-600, measuring approximately 1 cm in length on a side. The sheets were not sintered, since the deposits tend to flake off flat pieces. Therefore, the surface roughness of the coated sheets was not identical to that of the deposits.

The contact angle was measured by placing a drop of the solution onto the coated surface and visually inspecting the angle through a magnifying lens mounted so that the side of the bubble was viewed. The solution was allowed to wet the surface for 1 hour prior to analyzing the angle, so that some solution had absorbed onto the surface. The contact angle was estimated to be 30° for both batches of magnetite.

Roughness tends to decrease the contact angle of a wetting fluid [C-1]. Since the sheets were not sintered, this effect was not measured. However, the accuracy of the measurement was no better than 10°, outweighing the error stemming from not sintering the sheets. The measurements were done at room temperature. Elevated temperatures tend to decrease contact angles of wetting fluids, but the trend and magnitude of the effect for the morpholine solution is unknown [C-1]. Furthermore, it is unknown how the presence of air rather than steam affected the results. Since some solution was absorbed onto the magnetite surfaces, hysteresis did not appreciably affect the measurements. The values obtained in the experiment were used in the model.

3.3.7 Summary of Results

Heat transfer data was only obtained for one B3 sample, since the other samples chipped and therefore only one thickness was represented. The parameters evaluated for a particular batch of magnetite were used for each sample of the batch. For example, the porosity, permeability and pore size distribution were common to all three samples of B4.

parameter	***thickness***	***pore size***	***permeability***	***porosity***	***porosity***
units	μm	μm	m^2		
method	SEM	HgPS	flow study[+]	HgPS	loading
SAMPLE					
B3		**0.1-0.26**	**6E-16**	***0.22**	**0.27**
B3-1	3			0.22	
B4		**0.035-0.23**	**4E-16**	**0.49**	**0.47**
B4-1	10			0.47	
B4-2	38			0.40	
B4-3	24			0.59	
B4(7)		**0.035-0.20**	**1E-16**	**0.61**	**0.60**
B4(7)-1	13			0.53	
B4(7)-2	24			0.67	
B4(7)-3	33			0.64	

* The results of the samples were averaged to obtain the porosity of the batch.
+ See section 3.3.5

Table 3.1: Measured Sample Characteristics

3.4 Characteristics of Steam Generator Deposits and Sludge

Since the boiling heat transfer model was developed for steam generator u-tube fouling deposits and its accuracy evaluated by comparing the calculated results to measurements on simulated deposits, the similarity of the simulated and real deposits should be analyzed. The literature lacks any information on the characterization of real fouling deposits. However, heat transfer measurements have been taken on deposits from CANDU plants at AECL [T-3].

SEM micrographs of the deposits show that the particles are predominantly spherical and range in radius from 0.1 to 2 μm. The composition is mainly magnetite but depends on the secondary side chemistry and materials. For

instance, in the plants with brass condensers, there is an elevated level of copper in the deposits comprising approximately 30% of the deposit by mass. Typically, the content of the deposits is 90% magnetite. The porosity ranges from about 0.3 to 0.6 [T-4].

The permeability has not been measured but the permeability of the sludge pile from a variety of plants was studied. The values ranged from E-12 to E-14 m^2. The fact that the simulated deposits measured two orders of magnitude lower is not surprising, since the pore sizes of the deposits are smaller and the porosity generally lower. Furthermore, the sludge pile is unconsolidated, whereas the deposits are consolidated [B-1][B-3]. This factor alone can account for one order of magnitude difference in permeability [D-1]. Probably the best determination of the similarity is the fact that the simulated deposit heat transfer data were consistent with that of the real deposits. An SEM micrograph of the surface of a deposit on the u-tube of a CANDU steam generator is depicted in Figure 3-13.

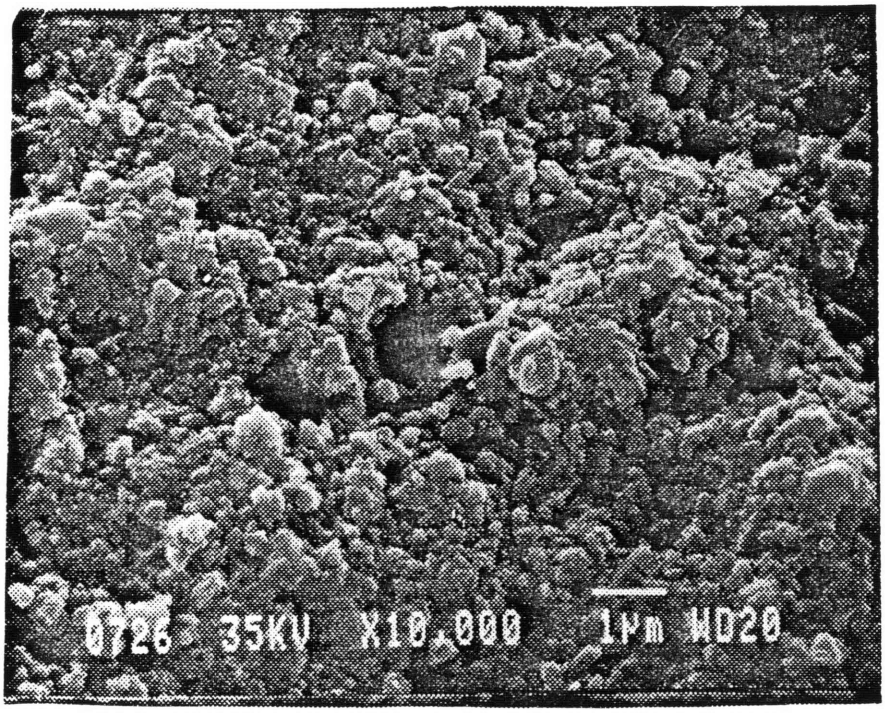

Figure 3-13: Surface SEM Micrograph of CANDU Fouling Deposit

4 HEAT TRANSFER EXPERIMENTS

4.1 Introduction

The experimentation was performed at AECL, Chalk River. The outer diameter (OD) deposits were fabricated at the laboratory and machined to meet the design specifications of the OD heat transfer setup. The inner diameter (ID) deposits did not require any machining. A high temperature/pressure heat transfer loop was used to set the conditions of the experiments. The OD and ID heat transfer measurements are outlined in Section 4.2 and 4.3, respectively. The results of the OD measurements and an error analysis are presented in Chapter 6 to facilitate their comparison to theory. The results of the ID measurements are discussed in Section 4.3.4.

4.2 OD Heat Transfer Measurements

The OD experiments measured the temperature drop across the deposits to a forced convected flow in both saturated boiling and subcooled conditions. The aim of the boiling runs was to determine the effects of deposit characteristics, heat flux and mass flux on the boiling heat transfer of the deposits, whereas the thermal conductivity of each deposit was measured in the subcooled runs.

4.2.1 The ID Test Configuration

The coated tube was cut into 2.0 cm sections. One section was used in the heat transfer measurements. The inside of the tube was machined to remove any deposit or film. Three 21 mil holes were drilled into the center of the tube wall, to a depth of 1.0 cm. Therefore, the thermocouples were located at the midpoint of

the wall in the center of the 2.0 cm test section of the deposit. Type K thermocouples with a diameter of 20 mils were placed into the holes, so that good contact was achieved. Figure 4.1 depicts the location of the thermocouples.

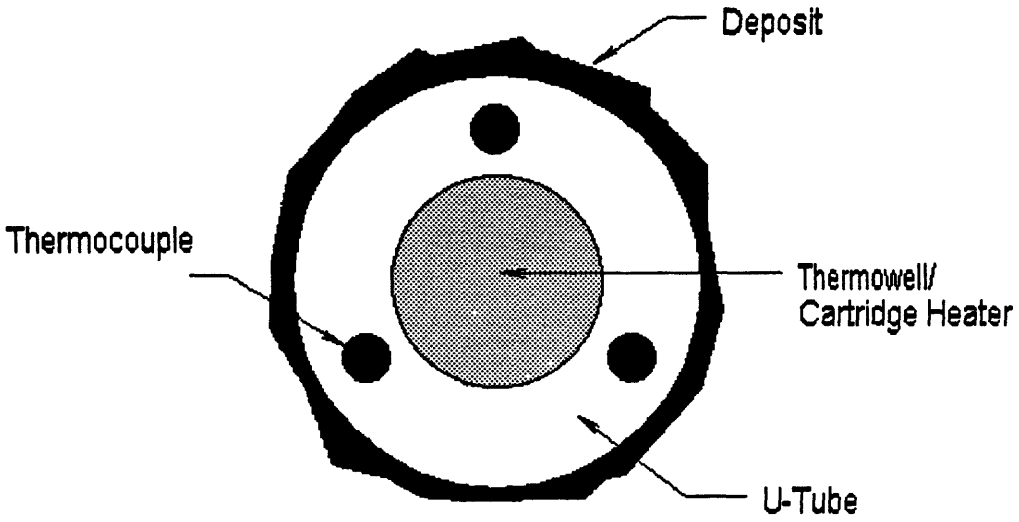

Figure 4.1: The Location of the Thermocouples in the U-Tube for the OD Heat Transfer Setup

A 5.0 cm sheath of stainless steel was press fit onto a thermowell. The test section was then press fit onto the sheath. There was a negligible gap between the test section and the sheath. Two 1.5 cm sections of clean I-600 u-tube were fit onto the sheath on both sides of the test section. This prevented any disturbance in the flow pattern around the test section (the fouled 2.0 cm sample). The combined length of the test section and clean tubes measured 5.0 cm so that the sheath was completely covered. The sheath served only to increase the diameter of the thermowell, since no thermowells with an outer diameter equal to the inner diameter of the I-600 u-tubes could be purchased.

Ceramic was placed on the exposed areas of the thermowell, surrounding the u-tubes, and prevented any heat transfer to the bulk flow from the thermowell. Therefore, the sheath and subsequently the test section and the clean tubes,

received virtually all of the heat flux. Rulon covered the squared end of the thermowell/ceramic edge to prevent flow pattern disruption. A cartridge heater was then inserted into the thermowell. The expanse of its heated zone was on the order of 5.0 cm. The test setup is depicted in Figure 4.2. The units are in cm.

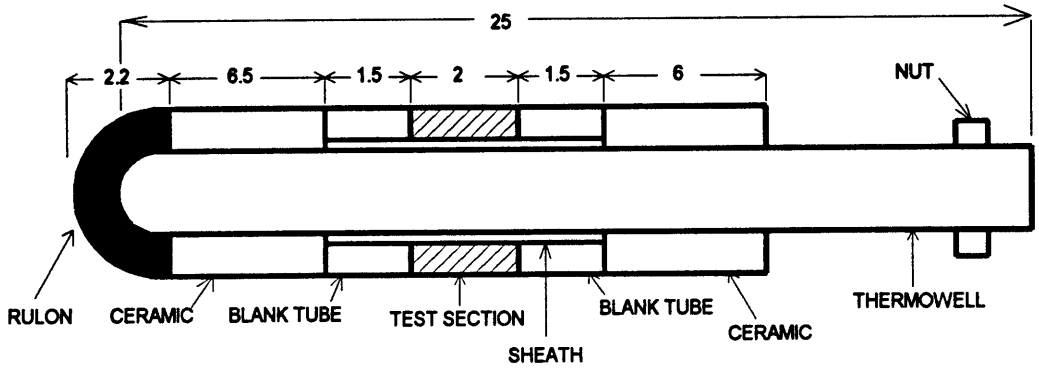

Figure 4.2: Schematic of the OD Heat Transfer Setup

The test setup was placed into the autoclave of the heat transfer loop, so that the flow was vertical and perpendicular to the applied heat flux. Figure 4.3 shows this arrangement. The heat transfer loop is depicted in Figure 4.4. The thermocouples were connected to the recorder through the head of the autoclave by passing them through lava type seals. The conditions of the loop were set by the heated section upstream of the autoclave, the pressure control valve and the pump. Therefore, boiling conditions were achieved when the cartridge heater was not energized. The cartridge heater only served to apply heat flux to the test section, not to set conditions in the loop. The flow rate, pressure and quality were constant upon entering the autoclave.

The flow rate was measured by a calibrated temperature independent flow meter. The pressure of the autoclave was measured by a gauge connected directly to the autoclave. The quality was calculated by knowing the flow rate, the power to the heated section of the loop and the pressure in the autoclave. A measured amount

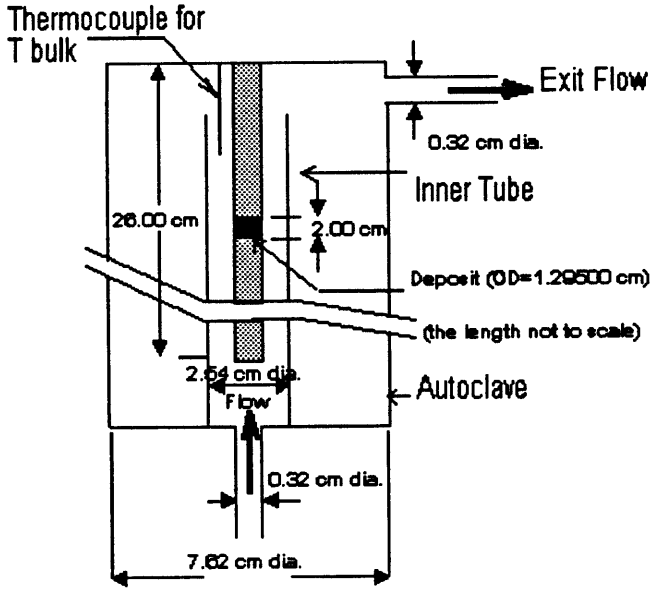

Figure 4.3: The Arrangement of the OD Setup in the Autoclave

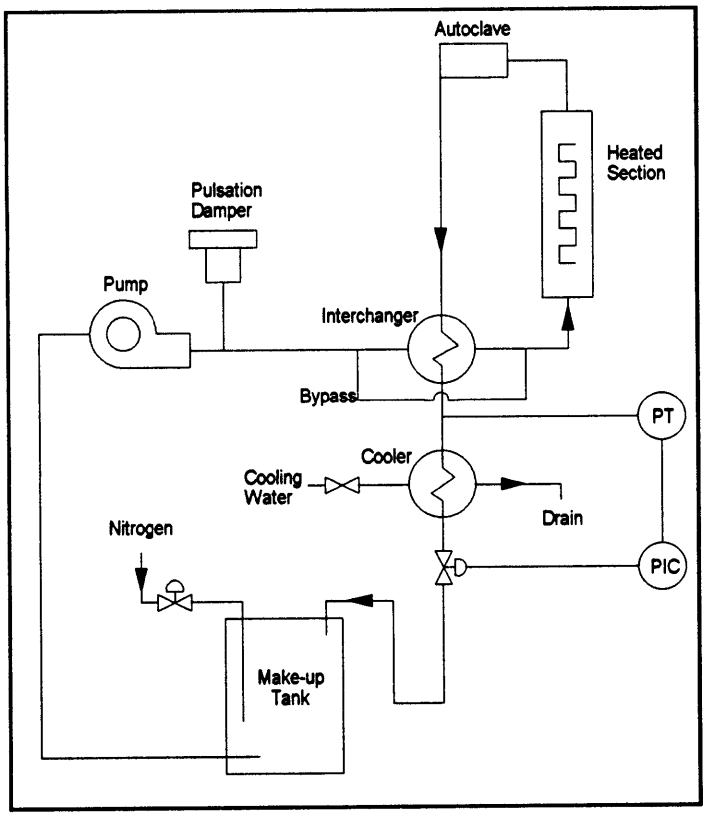

Figure 4.4: Schematic of the Heat Transfer Loop

of alternating electrical current was passed through the boiler tubes of the heated section to heat the flow. The heated section and all loop components up to the interchanger were insulated to prevent heat loss. The thermal efficiency of the heated section was calculated during the one phase studies and was used to obtain the quality of the two phase runs. The efficiency, typically 95%, was calculated by knowing the temperature entering and exiting the heated section and the flow rate.

4.2.2 Procedure

Table 4.1 summarizes the OD heat transfer runs performed in this study. The term run refers to a specific sample, flow rate and quality (boiling or subcooled). Each sample was put into the autoclave and the conditions were set 12 hours before the start of the run to allow the deposit to hydrate. In each run, the wall temperatures and the bulk temperature of the fluid in the autoclave were measured at zero power and three heat fluxes measuring 4.92E4, 6.14E4 and 7.37E4 W/m^2. In some graphs and tables in this text, these values are referred to as q"(1), q"(2) and q"(3), respectively. The use of the zero power measurements is described in Chapter 6. After the heat fluxes were changed, the system was allowed to stabilize before measurements were taken (typically 10 minutes). Anywhere from 6-10 measurements of T_w and T_b were taken at intervals of one minute. This procedure was repeated twice to ensure repeatability of the measurements.

The measurements of each thermocouple were averaged to yield a wall temperature at a given heat flux for the individual thermocouple. The two series of measurements were averaged for each thermocouple. The data of each of the three thermocouples were then averaged to yield T_w, the average wall temperature for the heat flux. For the boiling and subcooled runs, the standard deviation of the 6-10 measurements taken by one thermocouple at each flux was typically 0.1 and 0.9 °C, respectively. The standard deviation in the thermocouple average wall temperature for the two series of measurements was never greater than 0.5 and 2.0

°C for the boiling and subcooled runs, respectively. The 6 to 10 measurements of T_b were averaged for each heat flux. This value was then averaged for both series of measurements. T_b displayed the same standard deviation as the wall thermocouples. The value of T_w - T_b was obtained for each heat flux by subtracting the average value of T_b from that of T_w..

Once the measurements were completed for the fouled sample, the setup was removed from the autoclave and the deposit was stripped from the test section. The removal of the deposit was done by sanding with 320 grit emery paper until no deposit was visible. The tube was then sanded with 3 μm diamond paste. This practice was used to yield a reproducible surface finish. Measurements were repeated with the clean tube under identical conditions. The clean tube was allowed to oxidize in the loop under the run conditions for 12 hours prior to the start of the measurements.

Sample	Subcooled	*G(1)=5	G(2)=125	G(3)=250
Batch 3				
B3-1	-	X	-	-
Batch 4				
B4-1	-	X	-	-
B4-2	X	X	X	X
B4-3	X	-	-	X
Batch 4(7)				
B4(7)-1	X	X	X	X
B4(7)-2	X	-	X	X
B4(7)-3	X	X	X	X

*G is in kg/m^2-s

#The subcooled and boiling runs were done at a pressure of 4.2 and 4.4 MPa, respectively. The quality of the boiling runs was 5%. In each run, measurements were taken at three heat fluxes, 4.92E4, 6.14E4 and 7.37E4 W/m^2. The terms G(1), G(2) and G(3) are used to refer to the corresponding mass flux levels throughout the text.

Table 4.1: #Test Matrix of the OD Heat Transfer Study

4.2.3 Boiling Conditions

All the boiling studies were performed at a pressure of 4.4 MPa and a quality of 5%. The flow rates were varied to determine the effect of this parameter on the heat transfer in saturated boiling conditions. The mass fluxes used were 5, 125 and 250 kg/m^2-s. As shown in Table 4.1, in some graphs and tables in this text, these values are referred to as G(1), G(2) and G(3), respectively. The 2.54 cm tube was removed from the autoclave to obtain G(1). For some samples, only one mass flux was used, since the availability of the loop limited the size of the test matrix. The flow rates were not only restricted by the loop but also by the durability of the deposits. The shear on the deposits was elevated by the quality in boiling conditions, and therefore the mass fluxes used were lowered from that of the subcooled studies to ensure the adhesion of the deposits during the runs.

4.2.4 Subcooled Conditions

The subcooled studies were performed at a pressure of 4.2 MPa and at a mass flow rate of 300 kg/m^2-s. The original flow rate used for B3-1 and B4-1 was G(1). This value did not yield good data, as the temperature drop across the thermal boundary layer was too large in comparison to the temperature drop across the deposit to evaluate a difference between the fouled and clean tube. Therefore, in Table 4.1, these runs are not listed. In all other runs, the results were used to obtain the thermal conductivity of the deposit, a property used in the model.

From each subcooled run, the efficiency of the heated section was calculated and used to determine the quality in the boiling runs of the given sample.

4.3 ID Heat Transfer Measurements

The purpose of the ID heat transfer measurements was to determine the effect of steam quality and mass flux on the heat transfer of a clean I-600 u-tube and one internally coated with magnetite. The OD setup prohibited the use of elevated qualities because of the cost and time invested in the fabrication and characterization of the deposits. It was feared that the deposits would chip in the presence of elevated flows and qualities, and the runs would be lost. The ID setup required a fraction of the cost and time in fabrication, and therefore, the mass flux and the quality were elevated in these tests.

The ID coating process does not produce uniform deposits, so the deposit was not characterized and the thickness was only estimated. In addition, the adherence of the deposit was uncertain so that more thermocouples were used to measure the temperature of the fouled tube than the clean tube. Several batches of magnetite have been produced using the same procedure as the batch used in this test and have particle sizes on the order of 0.25 μm in radius and porosities of approximately 30-40% [L-1].

4.3.1 The ID Test Configuration

The heat transfer loop heated section (see Figure 4.5) was replaced with three sections of I-600 tubing with an ID of 1.0715 cm. The first and last sections were clean tubing and measured 1.00 and 0.20 m in length, respectively. The middle section, 0.90 m in length, was coated with a layer of uncharacterized magnetite, measuring approximately 10 μm in thickness. The total length of the setup measured 2.10 m. The sections were connected to each other and fitted into the loop with Swagelok fittings. Eleven thermocouples were spot welded to the outside of the fouled tube and one to each of the clean tubes. No thermocouples were placed on the 10 cm sections upstream and downstream of the Swagelok

fittings so that temperatures were measured only in regions of relatively fully developed flow. The heat flux was applied through direct alternating electrical current heating. The section was insulated to minimize heat loss. The setup is depicted in Figure 4.5.

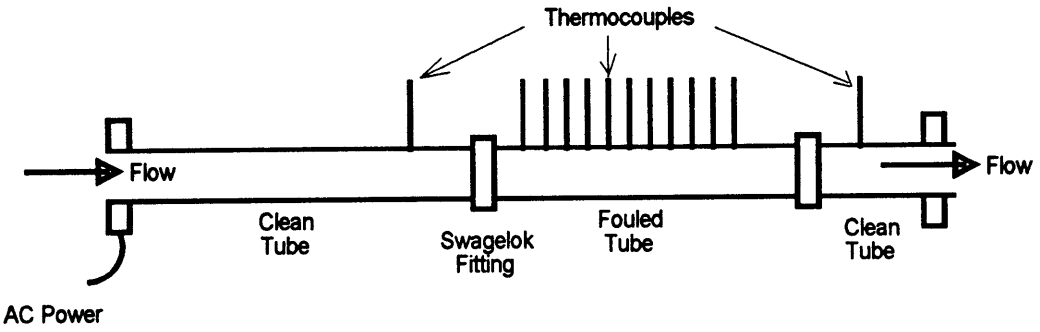

Figure 4.5: Schematic of the ID Heat Transfer Setup

4.3.2 Procedure

To determine the effect of quality, the qualities of the runs were changed, and the heat transfer coefficients evaluated at a single thermocouple during one run was compared to the value measured in another run (the conditions at the thermocouple changed between runs). To perform the sensitivity study, it was necessary to hold the heat flux and flow rate constant while changing quality. Since the heat flux was constant along the length of the setup, the quality increased in the direction of flow. This was done by changing the inlet enthalpy to the test section through the use of the interchanger. To drop the temperature, the bypass to the interchanger was opened, reducing the flow through the interchanger. To determine the effect of flow rate, the heat flux and qualities were held constant, and the flow rates were changed. This was done by changing the inlet enthalpy. Once conditions were set, temperatures were sampled for 15 minutes at one minute intervals.

The runs are outlined in Table 4.2. The pressure was set at 4.9 MPa. The electrical power applied to the heated sections was 16.0 kW. The thermal efficiency of the setup was calculated to be 93%, by measuring the test section inlet and exit temperatures, mass flux and heat flux under single phase conditions. Therefore, 16.0 kW corresponded to a heat flux of 2.1E5 W/m^2 on the inner diameter of the u-tube and a volumetric heat rate of 1.8E5 kW/m^3. Two mass fluxes were studied, 273 and 185 kg/m^2-s. The inlet temperatures were adjusted so that each mass flux was run with three different ranges of qualities. Therefore, the effect of mass flux, G, at three ranges of qualities, $x_v(1)$- $x_v(3)$, as well as the effect of quality at two mass fluxes, were analyzed with this test. Table 4.2 shows the run conditions and qualities produced at each thermocouple location.

4.3.3 Data Analysis

The goal of the study was achieved by comparing the heat transfer coefficients between runs to determine the effects of the parameters. When performing the comparisons, the data for a given thermocouple were compared only to the data of the same thermocouple collected in the different runs. This procedure was independent of the effects of thermocouple offset and deposit thickness inhomogeneity. The only error stemmed from the calculation of the heat transfer coefficient, and the determination of quality and mass flux at each location. These points are further discussed later in the text.

The determination of the heat transfer coefficient involved some calculations. The fluid enthalpy at each location was evaluated to determine the quality and temperature. Since the inlet temperature, pressure and hence, enthalpy were known, the fluid enthalpy at each thermocouple was calculated by knowing the heat flux [G-1]. The quality at each thermocouple was then determined. Once a homogeneous quality greater than zero was reached, the temperature of the bulk flow, T_b, was assumed to be the saturation temperature of the system pressure

found in the steam tables [G-1]. If subcooled, the temperature was evaluated through knowledge of the enthalpy and the use of subcooled steam tables.

To calculate the heat transfer coefficient of the tube, the inner wall temperature, T_{wi}, was required. Therefore, the measurements taken on the outside of the tube, T_{wo}, were used to evaluate the inner wall temperature by knowing the volumetric heat rate applied, q''', the thermal conductivity of the I-600 tube, k_{I600}, and the tube inner and outer radii, r_i, r_o:

$$T_{wi} = T_{wo} - \frac{q'''}{4\,k_{I600}}\left(2\,r_o^2 \ln\left(\frac{r_o}{r_i}\right) - r_o^2 + r_i^2\right). \tag{4.1}$$

The value of k_{I600} was based on T_{wo} [P-3]. The evaluation of the heat transfer coefficient, h, was completed with the following relation:

$$h = q''/(T_{wi} - T_b). \tag{4.2}$$

The effect of the parameters on the heat transfer coefficient was determined by calculating the difference between the h values measured under different conditions. Since the thickness and the adhesion of the deposit were uncertain, the differences in h (Δh) at every thermocouple on the fouled tube were averaged, whereas the average of only two thermocouples was used to determine the effects on the clean tube. The averages were done only on locations where the homogeneous quality was greater than zero.

Therefore, to determine the effect of quality, the h values of run 1 were subtracted from those of both run 2 and run 3. The results were averaged with the difference between run 2 and run 3. This was also done for the runs with G=185 kg/m^2-s. To ascertain the effect of flow, the h values of G=185 kg/m^2-s were subtracted from those of G=273 kg/m^2-s at each quality. Therefore, run 4 was subtracted from run 1, run 5 from run 2 and run 6 from run 3. The results are given in section 4.3.4.

Thermocouple #		1	2	3	4	5	6	7	8	9	10	11	12	13
Thermocouple location (m)		0.85 (clean)	1.06	1.13	1.20	1.27	1.34	1.42	1.49	1.56	1.62	1.69	1.76	1.96 (clean)
G=273 kg/m^2-s														
x_v T_{in} (∘ C)	Run #													
1 225	1	0.05	0.09	0.10	0.12	0.13	0.14	0.16	0.17	0.18	0.20	0.21	0.22	0.26
2 205	2	-0.00	0.04	0.05	0.06	0.08	0.09	0.10	0.12	0.13	0.14	0.16	0.17	0.21
3 185	3	-0.06	-0.02	-0.00	0.01	0.02	0.03	0.05	0.06	0.08	0.09	0.10	0.11	0.15
G=185 kg/m^2-s														
x_v T_{in} (∘ C)	Run #													
4 185	1	0.00	0.05	0.07	0.09	0.11	0.13	0.15	0.16	0.18	0.20	0.22	0.23	0.28
5 165	2	-0.05	0.00	0.02	0.04	0.06	0.07	0.10	0.11	0.13	0.15	0.17	0.18	0.23
6 145	3	-0.09	-0.04	-0.02	-0.00	0.02	0.04	0.06	0.08	0.09	0.11	0.13	0.15	0.20

4.2: ID Experiment Runs and Conditions

The evaluation of the heat transfer coefficient involved a variety of assumptions. T_{wi} was calculated from T_{wo} using equations 4.1. The value of k_{I600} was based on T_{wo}, rather than the radially averaged temperature. Since T_{wo} and T_{wi} differed by no more than 4 °C, corresponding to an 0.06 W/m-K change in k_{I600} [P-3], virtually no error can be attributed to this assumption. The heat flux was known since the efficiency of the heated section was calculated, as previously described. Pressure, measured at the outlet of the test section, was assumed to be constant along the length of the test section. Therefore, once the enthalpy of the fluid reached that of saturated liquid, T_b was assumed to be the saturation temperature at the test section pressure. A conservative estimate of the pressure drop at the highest mass flux and exit quality was evaluated using the Thom correlation [T-1] (Appendix B) and yielded a value of 6.9 kPa. Since this pressure drop corresponds to 0.09 °C change in saturation temperature, the assumption that T_b was constant induced negligible error.

When calculating the liquid enthalpy, it was assumed that the heat flux raised the liquid temperature to saturation and then initiated nucleation. Therefore, the condition of superheated vapor coexisting with subcooled liquid was not postulated. Vertical churn and annular flow in the test section precluded the development of thermally inhomogeneous phases, so that the use of homogenous quality was generally valid [H-1]. The error in the determination of the heat transfer coefficient at each thermocouple location was limited to the accuracy of the steam tables.

Once the heat transfer coefficients were evaluated for one run, determining the change in value between runs was independent of the effects of thermocouple offset and deposit thickness inhomogeneity (since the data of one run were compared only the data of another run for a given thermocouple).

The difference in mass flux between runs was known, since the flow meter was calibrated. The change in quality was calculated by subtracting the quality at each thermocouple between runs. The quality was calculated by assuming that test section pressure remained constant (the method was previously described) and that no thermal inhomogeneity developed between the phases. The error associated with this assumption was limited to the accuracy of the steam tables.

Overall, the error of the ID experiments stemmed from the accuracy of the steam tables and the assumption that pressure was constant along the 2.1 m test section and was presumed negligible.

4.3.4 Results

Table 4.3 displays the results of the runs. Δh_F and Δh_C denote the difference in the heat transfer coefficient for the fouled and clean tubes as respectively, whereas h_F and h_C are the heat transfer coefficients of the fouled and clean tubes. The values of Δh (for both the fouled and clean tube) were obtained by subtracting h of one run from h of another. A Δh value of zero implies that no change in the heat transfer coefficient, h, was noted for the change in conditions (either quality of mass flux) between the runs.

In the experiment, the effect of quality was analyzed by holding mass flux and heat flux constant while increasing quality (see Table 4.2). The percent change in quality between runs was not the same at each thermocouple. For the fouled thermocouples, #2-#12, the change in quality between $x_v(1)$ and $x_v(3)$ was approximately 150% for the two mass fluxes. For example, the qualities at #12 at G=273 kg/m^2-s measured 0.11, 0.17, 0.22, respectively, whereas the values at #2 measured 0.0, 0.05 and 0.10. The percent change in quality between runs was obtained by averaging the change at each fouled thermocouple location. This method facilitated the summarization of the data. The values of quality are given

in Table 4.2 if more detail is required. At thermocouple #13 on the clean tube, the average change was about 50%.

The effect of quality on the fouled tube heat transfer coefficient was not constant. This conclusion was drawn by considering the average Δh_F (runs 1-3) and (runs 4-6). The latter was negative, implying an increase in quality reduced h_F, while the former was positive. The magnitude of the changes was determined by comparing the Δh_F values to the h_F values, also shown in the Table 4.3. The h_F values were on the order of 18 kW/m^2-K compared to the values of -0.06 and +0.15, corresponding to -0.3% and +0.8% change in h_F, respectively and an average of +0.2%. Due to the lack of a constant trend and the low values calculated (-0.06 and +0.15), it is postulated that quality did not affect the heat transfer coefficient of the fouled tube for the changes in quality achieved in the experiment (see Table 4.2).

In contrast to Δh_F, Δh_C was always positive, implying that h_C increased with quality. For both mass fluxes, the average Δh_C (runs 1 through 3) and (runs 4 through 6) was approximately +0.38. Therefore, in comparison to the h_C values, which were on the order of 13 kW/m^2-K, the Δh_C values corresponded to a 3% change in h_C. Certainly a small effect was recorded, but since the trend was constant, and the error associated with the comparison was negligible, it was postulated that an effect of quality, rather than just random fluctuations in data, was measured.

Due to the limitations of the experiment, the mass flux was not changed dramatically but only increased by 50%. The effect of mass flux on h_C was constant. In all cases, h_C increased with mass flux. The magnitude of the Δh_C values were small in comparison to the values of h_C. The comparison of run 1 to run 4, or the effect of mass flux at $x_v(1)$ yielded Δh_C of +0.76. The comparison at the other quality ranges gave similar results, +0.77 and +0.73 at $x_v(2)$ and $x_v(3)$,

respectively. Therefore, mass flux did not affect the clean tube dramatically, since the average effect was +0.75 compared to h_C values on the order of 13 kW/m^2-K, corresponding to a +6% change in h_C for a 50% increase in mass

Effect of Quality	**range in Δh_F** (kW/m^2-K)	**average Δh_F** (kW/m^2-K)	**average Δh_C** (kW/m^2-K)
G=273 kg/m^2-s			
run 1-run 2	-0.08 - -0.09	-0.02	+0.20
run 1-run 3	-0.16 - +0.02	-0.09	+0.58
run 2-run 3	-0.11 - +0.02	-0.08	+0.37
average Δh (runs 1 through 3)		-0.06	+0.39
G=185 kg/m^2-s			
run 4-run 5	-0.47 - -0.06	-0.21	+0.21
run 4-run 6	-0.04 - +0.38	+0.22	+0.55
run 5-run 6	+0.35 - +0.50	+0.43	+0.33
average Δh (runs 4 through 6)		+0.15	+0.36
average Δh (all runs)		+0.04	+0.38
Effect of Mass Flux			
$x_v(1)$ run 1-run 4	-0.09 - +0.17	+0.12	+0.76
$x_v(2)$ run 2-run 5	-0.19 - +0.09	-0.06	+0.77
$x_v(3)$ run 3-run 6	+0.33 - +0.57	+0.43	+0.73
average Δh (all runs)		+0.16	+0.75
Run #	**average h_F** (kW/m^2-K)	**average h_C** (kW/m^2-K)	
1	18.10	13.34	
2	18.12	13.13	
3	18.31	12.76	
4	17.98	12.58	
5	18.18	12.37	
6	17.77	12.03	

Table 4.3: Results of the ID Heat Transfer Measurements

flux. Since the trend was constant, and the error associated with the comparison was negligible, the experiment recorded the effect of mass flux and not scatter in the data.

The values of h_F did not exhibit a constant trend with mass flux, with Δh_F ranging from -0.06 to +0.43 in the runs with $x_v(2)$ and $x_v(3)$, respectively. The average Δh_F was +0.16 corresponding to a +0.9% change in h_F. Therefore, no effect of mass flux on the fouled tube heat transfer coefficient was measured in the experiment.

Although comparing h_C to h_F involves error associated with the offset of the thermocouples, the fact that the fouled sections exhibited a larger average heat transfer coefficient than the clean section, warrants consideration. The same conclusion was drawn in the analysis of some OD runs, as discussed in Chapter 6.

4.3.5 Discussion of Results

The effect of quality was not measured in the OD boiling runs. It was concluded in this study that an approximately 50% increase in quality increased the boiling heat transfer coefficient of the clean tube by +3%. This is consistent with the work done by Chen [C-2], who concluded that under approximately the same conditions, increasing the quality by 50% (from 10% to 15% and from 15% to 20%) changes the heat transfer coefficient by an average of 6%. The effect of quality on the fouled tube was not consistent. Its average effect was +0.3% for a 150% change in quality. Therefore, it is hypothesized that at mass fluxes of 185 and 273 kg/m^2-s, the heat transfer coefficient of the clean tube increased slightly with quality, whereas that of the fouled tube was insensitive to quality, over the range of qualities achieved in the study (Tables 4.1 and 4.2).

The effect of mass flux on the heat transfer coefficient of the fouled tube was not constant, averaging +0.9% for a 50% change in mass flux. Consistent with work done by Macbeth [M-1], it was concluded that mass fluxes of the study did not affect h_F. In contrast, the effect on the clean tube was both constant and more

dramatic, averaging +6% for a 50% change in mass flux. The results of the clean tube are somewhat consistent with the Chen correlation which calculates a +15% change for a 50% change in mass flux under approximately the same conditions. Therefore, the ID studies have shown that increasing mass flux does not affect h_F and only slightly increases h_C. The same conclusion was drawn in the OD boiling measurements and is discussed Chapter 6.

5 THE THEORETICAL MODEL

5.1 Introduction

The goal of this research effort was to identify the heat transfer characteristics of steam generator u-tube fouling deposits. One aspect of the research involved the development of a heat transfer model. The approach used was to take advantage of previously proven models of heat transfer, and link the models through boundary conditions. Therefore, models involving boiling in porous media and two phase forced convection were utilized [C-2][K-1]K-2][K-3][S-4].

Since mass fluxes on the order of 10^2 kg/m^2-s, and vapor qualities of approximately 25% exist on the secondary side of steam generators, the effects of these parameters on heat transfer were considered. A correlation for the boiling heat transfer to saturated fluids in convective flow was developed by Chen [C-2] and applies to the conditions typical of steam generators.

If the u-tubes are fouled, the situation is further complicated, since the deposits change the surface characteristics of the u-tubes. Heat transfer in pool boiling has been well studied. Surface conditions have been strongly linked to the heat transfer coefficient in pool boiling, as the required superheat for nucleation is governed by geometry of the nucleation sites, mainly radius and cone angle [L-3][S-3]. However, these studies only consider isolated surface pits and not the morphology of the deposits, comprised of interconnecting channels of pores.

Heat transfer in porous media has been well studied [B-2][C-4][J-1][K-1][K-2][K-3][M-1][M-2][S-2][S-5][U-1]. These models do not account for the forced convective aspect of the heat transfer and assume 100% of the applied heat flux is evaporated in the deposit. Furthermore, most do not utilize what has been learned

from pool boiling investigations, that pit geometry strongly influences surface boiling [C-1][C-5][H-3][L-3][S-3]. This knowledge warrants the consideration that pore size distribution also affects heat transfer in porous media.

Due to its consideration of pore size, the Kovalev model was used as the basis for the model in the porous deposit. The Chen model was used as the forced convective component of the model, and boundary conditions were developed. Each separate model is outlined and the boundary conditions that link the models are presented [C-2][K-1][K-2][K-3][S-5]. A brief discussion on the method of solution of the combined model is made in section 5.5.

5.2 Chen Correlation for Boiling Heat Transfer to Saturated Fluids in Convective Flow

Chen's model was developed for two phase flow conditions. The model does not apply to post critical heat flux or liquid deficient cases. The heat transfer is assumed to occur by two different modalities, an ordinary macroconvective and a microconvective mechanism. The latter heat transfer mechanism is associated with bubble nucleation and growth, and the former is attributed to forced convection. The Chen correlation assumes that the micro and macro components are additive. Each mechanism is discussed below.

5.2.1 The Microconvective Component

The analysis of Forster and Zuber was used as the basis for the microconvective mechanism of heat transfer [F-1]. The Forster and Zuber correlation was developed for pool boiling on the premise that the Reynolds number for microconvection is governed by the bubble growth rate. In essence, the detaching

bubbles agitate the liquid adjacent to the wall and increase the effective Reynolds number of the system.

$$h_{mic} = 0.00122 \frac{k_l^{0.79} c_{pl}^{0.45} \rho_l^{0.49} g_c^{0.25}}{\sigma^{0.5} \mu_l^{0.29} h_{fg}^{0.24} \rho_v^{0.24}} (T_{wall} - T_b)^{0.24} (P_s(T_{wall}) - P_b)^{0.75} S \qquad (5.1)$$

where the subscripts l and v refer to liquid and vapor phase, respectively, and k, c_p, g_c, h_{fg}, ρ, σ and μ are the thermal conductivity (kW/m-K), specific heat (kJ/kg-K), gravitational constant (m^2/s), latent heat of vaporization (kJ/kg), density (kg/m^3), surface tension (N/m) and viscosity (Pa-s). T_{wall} is the temperature of the wall , and T_b is the saturation temperature corresponding to P_b, the pressure of the bulk flow. $P_s(T_{wall})$ is the saturation pressure corresponding to T_{wall}. Since only temperature differences are used, the units may be in Kelvin or Celsius. Pressure is in Pascals. The equation yields h_{mic} in kW/m^2-K.

The term, *S*, is the suppression factor, defined as the ratio of the effective superheat to the total superheat of the wall. In both pool boiling and convective boiling, the degree of superheat is not constant across the thermal boundary layer. The effective superheat is based on some average temperature of the thermal boundary layer, slightly lower than the wall temperature. This effect stems from the fact that as bubbles grow, they extend from the hot wall into the thermal boundary layer towards the cooler bulk fluid. If the boundary layer profile is steep, the bubbles reach cool fluid during growth and condense before they detach from the wall. Hsu developed this principle into his criteria for bubble nucleation [H-3]. In pool boiling, the temperature profile across the thermal boundary layer is not steep, so that Forster and Zuber assumed the effective superheat was equal to the wall superheat. However, this effect cannot be neglected with the steep profiles of high flows. Chen postulated that in all ranges of flow, the suppression factor is a function of the local two-phase Reynolds number, Re_{tp},

$$Re_{tp} = Re_l \left(F(X_{tt})\right)^{1.25}, \qquad (5.2)$$

where X_{tt} is the Martinelli parameter [M-3],

$$X_{tt} = \left(\frac{x_v}{1-x_v}\right)^{0.9}\left(\frac{\rho_v}{\rho_l}\right)^{0.5}\left(\frac{\mu_v}{\mu_l}\right)^{0.1}, \tag{5.3}$$

and x_v is the weight fraction of the vapor phase. For fluids other than liquid metals, the two phase Reynolds number is simply the liquid Reynolds number modified by a term, F, which is based on the liquid fraction of flow. Since the ratio depends on flow only, it is a function of momentum transfer and therefore, of the Martinelli parameter, X_{tt}. Chen used data to fit the function $F(X_{tt})$ and $S(\mathrm{Re}_{tp})$. Later, Collier developed the following empirical relations to fit Chen's curves [C-5]:

$$F(X_{tt}) = 1 \text{ for } X_{tt}^{-1} \le 0.1 \tag{5.4}$$

$$F(X_{tt}) = 2.35\left(0.213+\frac{1}{X_{tt}}\right)^{0.736} \quad \text{for } X_{tt}^{-1} > 0.1 \tag{5.5}$$

$$S(\mathrm{Re}_{tp}) = \left(1+2.56E-6\mathrm{Re}_{tp}^{1.17}\right)^{-1} \tag{5.6}$$

Therefore, $S(\mathrm{Re}_{tp})$ drops as Re_{tp} increases; high flow rates and qualities suppress surface nucleation.

5.2.2 The Macroconvective Component

Macroconvection normally occurs with flowing fluids but is complicated, due to the influence of vapor quality. Chen used a modified form of the Dittus-Boelter equation to quantify the effect of a two phase forced convected fluid. The form of the Chen macroconvective heat transfer coefficient, h_{mac}, is then:

$$h_{mac} = 0.023\left(\frac{k_l}{D}\right)\mathrm{Re}_l^{0.8}\,\mathrm{Pr}_l^{0.4}F(X_{tt}), \tag{5.7}$$

where $\mathrm{Re}_l, \mathrm{Pr}_l$ and D are the Reynolds, Prandtl numbers and diameter of the tube respectively. In the analysis for the steam generator, an equivalent hydraulic diameter is used for D .

5.2.3 The Chen Heat Transfer Coefficient

The Chen heat transfer coefficient, h_c, is simply the sum of the micro and macro components:

$$h_c = h_{mac} + h_{mic}. \tag{5.8}$$

5.3 Kovalev Model for Boiling Heat Transfer on a Capillary-Porous Surface

5.3.1 General Description

The Kovalev model assumes that inside the capillary-porous matrix, stable conditions of evaporation exist. Therefore, the liquid/vapor interfaces are constant, and the mass flux of liquid into the deposit is equal to the mass flux of vapor exiting. Capillary forces drive the fluid flow. The pores act as heat pipes-- liquid is supplied to the deposit through the action of capillary forces. The pores are modeled as right circular cylinders. Liquid flows into the deposit through channels of small pores and evaporates at the menisci formed with the larger pores. The vapor exits through channels of large pores. Therefore, liquid and vapor flow countercurrently in separate channels. The deposit is comprised of a connected porous matrix, its voids filled with a dispersed medium. In steam generator fouling deposits, water or steam is the dispersed medium, and magnetite is the matrix.

Dullien [D-1] found that if the capillary number of a system, $C_a = \mu_l v_l / \sigma$, the ratio of viscous to capillary forces, is less than 1E-3, vapor and liquid will flow in separate systems of pores (μ_l, v_l and σrepresent the liquid viscosity, velocity and surface tension respectively). In typical steam generator deposits, C_a is on the order of 1E-6, and thus this assumption applies.

Surface tension forces maintain dynamic equilibrium between the phases. The fluid is assumed perfectly wetting. Heat is conducted through the connected matrix of the deposit, since the conductivity of the matrix is greater than that of the liquid. The model is one-dimensional; the temperature of the matrix only varies in the direction of the heat flux, perpendicular to the u-tube. The heat capacity of the liquid is neglected as in phase change, latent heat outweighs the contribution of sensible heat. Liquid properties are assumed to remain constant in the matrix. All heat supplied to the deposit at its base is assumed to evaporate liquid, and no heat is conducted at the boundary of the deposit and the bulk flow.

5.3.2 Changes to the Kovalev Model

The Kovalev model was the basis for the model, but some changes were made. It was not assumed that the liquid completely wets the surface, so the model requires the value of the contact angle of the liquid. The thermal conductivity of the deposit is modeled to be one-half the value of the parallel arrangement of the magnetite matrix and the two phase fluid filling the pores. This approach was based on subcooled forced convection studies of the deposits and is further developed in section 5.3.3.2. The fluid properties are evaluated at each x location (see Figure 5.1). However, the deposit thicknesses used in this study (no larger than 38 μm) precluded appreciable changes in fluid properties. The deposit parameters and the heat flux applied at the base of the deposit determine the fraction of the heat flux transferred by phase change in the deposit. The remainder is transferred to the bulk flow at the deposit/bulk flow boundary. Therefore, the model incorporates a heat transfer coefficient at the deposit boundary to complete the solution procedure. This concept is further developed in section 5.5.

The model is not time-dependent and therefore, the saturation temperature of the liquid does not change with time. In reality, non-volatile species concentrate in the

deposit as liquid is vaporized. This effect could be easily incorporated, since the mass flux of vapor is calculated at each x position. Therefore, the concentration rate could be obtained. The saturation temperature could then be calculated as a function of the concentration based on the length of time the heat flux is applied.

Presently, the equations are solved for a constant heat flux case to facilitate the comparison of the model results to those obtained experimentally. Of course, the model boundary conditions can be readily reformulated to solve for the case of constant wall temperature if applied to the conditions of a steam generator.

5.3.3 Mathematical Description

The convention that the boundary of the deposit and the steam generator secondary side bulk flow is located at $x = 0$, and the boundary of the deposit and the u-tube is located at $x = t_d$, is used throughout the text to facilitate the description of the model. The term, t_d, represents the thickness of the deposit. The heat flux is applied at $x = t_d$. Figure 5.1 depicts the arrangement.

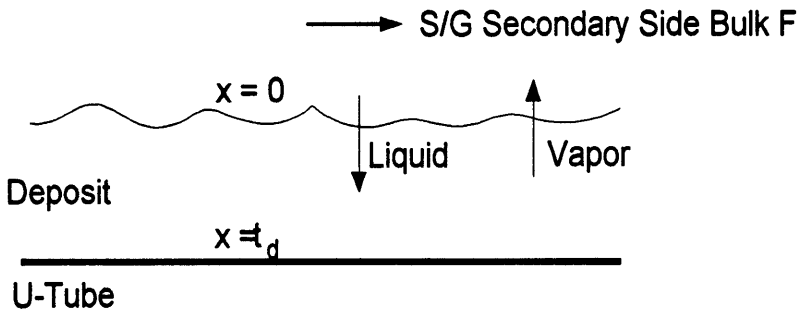

Figure 5.1: Coordinate System of the Deposit

5.3.3.1 Fluid Flow

At each cross section, x , the menisci have a radius, $R^*(x)$, governed by the relation:

$$P_c(x)=P_v(x)-P_l(x)=\frac{2\sigma\cos\theta}{R^*(x)}, \tag{5.9}$$

where P,σ,θ, v, l are the pressure, liquid surface tension and contact angle, the subscripts denoting vapor and liquid phases respectively. P_c represents the capillary pressure. The equation relates the vapor pressure to that of the liquid and defines the boundary between the liquid and vapor phases in the porous deposit. At a cross section, x , all pores with radii $r \geq R^*$, are filled with vapor, and those with $r < R^*$, are filled with liquid. In a pore with $r \geq R^*$, the difference in the vapor and liquid pressure (the capillary pressure) at the x location is larger than the interfacial pressure difference that develops across an interface with a radius of r. Therefore, the vapor flows through the pore and a meniscus does not exist.

Figure 5.2 depicts this situation. Pore 1 and 2 are filled with liquid and vapor respectively, because for the capillary pressure existing at the x location, the corresponding R^* is larger than r_1 but smaller than r_2. The capillary pressure is constant at an x location and is set by fluid flow equations, outlined below. Therefore, at an x position, the pressure of the liquid, P_l and that of the vapor, P_v, are constant. The existence of vapor in the pores stems from a mechanical force balance and implies that phase change occurred either at this x position or at larger values of x, closer to the heat flux where the temperatures are hotter. If phase change occurred at this x position, then according to Figure 5.2, $q''(0) < q''(x)$. In Figure 5.2, a section of the deposit is depicted, and x does not represent the u-tube/deposit boundary. The coupling of heat transfer and fluid flow is further described in section 5.3.2.2.

Due to the variation in R^* with x, zones for flow vary with the cross section. Therefore, the flow equations must include terms of acceleration, and the relative permeability terms must be a function of cross section. The equation of motion for the liquid and vapor phases respectively are:

$$\frac{\rho_l}{\Pi^2} v_l \frac{dv_l}{dx} = -\frac{dP_l}{dx} - \frac{\mu_l}{K_l} v_l, \tag{5.10}$$

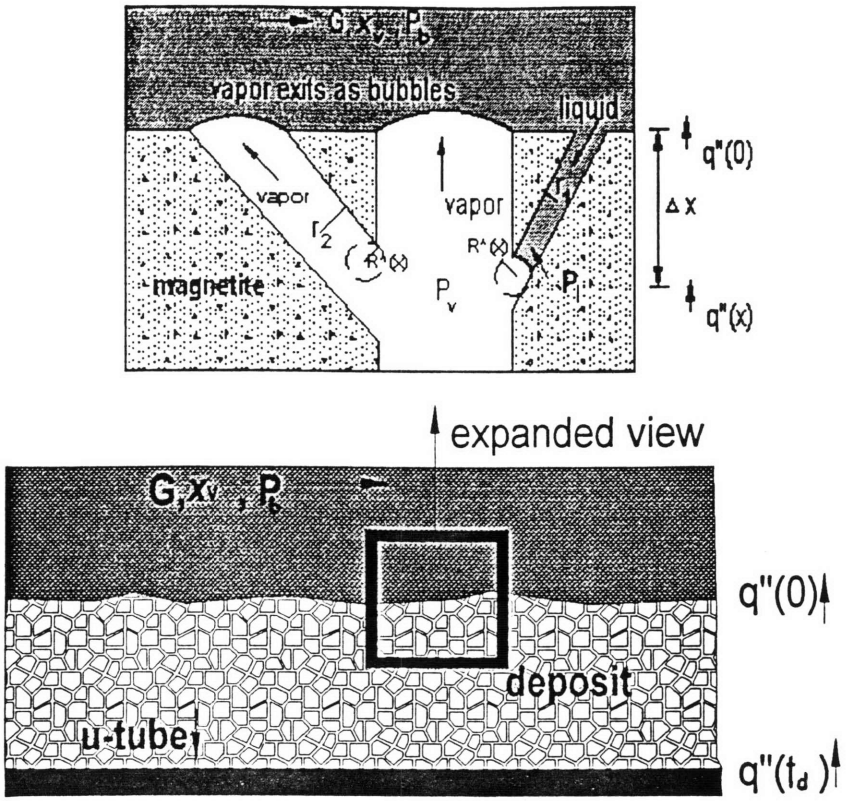

Figure 5.2: Schematic of R* in the Deposit

$$\frac{\rho_v}{\Pi^2} v_v \frac{dv_v}{dx} = -\frac{dP_v}{dx} - \frac{\mu_v}{K_v} v_v, \tag{5.11}$$

where v, ρ, K, μ, and Π are velocity, density, permeability and viscosity of the phase and porosity of the deposit respectively. Equations 5.10 and 5.11 are modified forms of Darcy's Law for the flow of fluid in a porous deposit, accounting for fluid acceleration. Darcy's Law only applies to flows with Re<1 [C-7][D-1][S-1]. To conservatively estimate the Reynolds number, assume the pore diameter is on the order of 1 μm and 100% of the applied heat flux (7.37E4 W/m^2) is vaporized. Unlike the calculation of the Reynolds number for conditions in a tube or channel, the mass flux in porous media must be scaled by the fractional surface area that the system of pores represent. An estimate of this is the porosity. Conservatively say the porosity is 10% and therefore the mass flux through the

pores is increased by an order of magnitude (since the mass flux must be divided by the porosity):

$$\mathrm{Re_d} = \frac{q'' \mathrm{D}}{\mathrm{h_{fg}}\,\mu_v\,\Pi} \tag{5.11 b}$$

The result is that the Reynolds number in the deposit, $\mathrm{Re_d}$, is approximately 2E-3 when $\mathrm{h_{fg}}$ and μ_v are 1.7E5 J/kg and 1.8E-5 Pa-s, respectively. Therefore, the use of Darcy's law is valid for much higher heat fluxes than used in the study.

Subtracting equation 5.11 from 5.10, differentiating equation 5.9 and substituting the result, the following is obtained (see Appendix C):

$$\frac{\rho_l}{\Pi^2} v_l \frac{dv_l}{dx} - \frac{\rho_v}{\Pi^2} v_v \frac{dv_v}{dx} = -\frac{2\sigma\cos\theta}{(R^*)^2}\frac{dR^*}{dx} - \frac{\mu_l}{K_l} v_l + \frac{\mu_v}{K_v} v_v. \tag{5.12}$$

Mass conservation yields the values for liquid and vapor velocity at a given cross section, x, in terms of the mass flux of vapor, $G(x) > 0$,

$$v_l(x) = -\frac{G(x)}{\rho_l \varphi(R^*)}, \tag{5.13}$$

$$v_v(x) = \frac{G(x)}{\rho_v (1-\varphi(R^*))}, \tag{5.14}$$

where $\varphi(r)$ is the cumulative pore size distribution, representing the fraction of the porous volume with values of radius less than r. Since the liquid flows countercurrently to the vapor, the velocities have opposite signs. Steady state forces the values of mass flux to be equal.

Substituting equations 5.13 and 5.14 into 5.12, and defining $f(r) = \frac{d\varphi}{dr}$ as the incremental pore size distribution, the first order hydrodynamic equation of countercurrent liquid and vapor flow in porous media is obtained:

$$\frac{dR^*}{dx}\left\{\frac{2\sigma\cos\theta}{R^*(x)^2}-\frac{G^2(x)f(R^*)}{\Pi^2}\left(\frac{1}{\rho_l\varphi^3(R^*)}+\frac{1}{\rho_v(1-\varphi(R^*))^3}\right)\right\}=\frac{G(x)}{\Pi^2}\frac{dG}{dx}*$$

$$\left[\frac{1}{\rho_v(1-\varphi(R^*))^2}-\frac{1}{\rho_l\varphi^2(R^*)}\right]+\frac{\nu_l G(x)}{CF(R^*)}+\frac{\nu_v G(x)}{K-CF(R^*)}, \qquad (5.15)$$

where

$$F(R^*)=\int_{r_{min}}^{R^*} r^2 f(r)dr\ , \qquad (5.16)$$

and r_{min} and r_{max} are the smallest and largest pore sizes in the deposit. A detailed derivation of equation 5.15 is given in Appendix C.

In equation 5.15, the liquid and vapor permeability is expressed in terms of the pore size distribution according to filtration theory,

$$K= C\int_{r_{min}}^{r_{max}} r^2 f(r)dr\ , \qquad (5.17)$$

$$K_l\varphi(R^*) = C\int_{r_{min}}^{R^*} r^2 f(r)dr\ , \qquad (5.18)$$

$$K_v(1-\varphi(R^*))= C\int_{R^*}^{r_{max}} r^2 f(r)dr\ , \qquad (5.19)$$

The constant, C, in equation 5.17 can be obtained by comparing the integral of the pore size distribution obtained through mercury porosimetry to the permeability measured experimentally. The experimental value of permeability was obtained in single phase flow conditions. Evidence has shown that the value measured in two-phase conditions is an order of magnitude lower than that in single phase [D-1][K-2]. Therefore, the measured value of K was reduced by an order of magnitude. It is apparent that K_l, K_v are functions of x through the dependence of $\varphi(R^*)$ on x.

5.3.3.2 Heat Transfer

Heat is transferred through the deposit, increasing the temperature of the deposit, T_d:

$$q''(x) = -k_d \frac{dT_d}{dx}, \tag{5.20}$$

where $q''$is the heat flux, and k_d is the thermal conductivity of the deposit. The connected magnetite matrix and the dispersed two phase fluid are modeled as acting in parallel to conduct heat. Based on subcooled forced convective studies, one-half the parallel arrangement was used (Chapter 6):

$$k_d = \left(\left[(1-\varphi)k_v + \varphi k_l\right]\Pi + \left[1-\Pi\right]k_m\right)/2, \tag{5.21}$$

where k_l, $k_v$and k_m are the conductivities of the liquid and vapor phase and magnetite, respectively.

Concurrent with conduction through the deposit, liquid evaporates at the menisci. Therefore, the gradient of heat flux is proportional to the incremental production of vapor. The following equation mathematically represents the situation:

$$\frac{dq''}{dx} = -k_d \frac{d^2T_d}{dx^2} = \alpha^v_{vol}\left(T_d - T_s(P_v)\right) = \frac{dG}{dx}h_{fg}, \tag{5.22}$$

where $T_s(P_v)$ represents the saturation temperature corresponding to the vapor pressure at the cross section, x. The term, α^v_{vol}, represents the volumetric heat transfer coefficient of phase change in the matrix [S-5]. The coefficient accounts for the thermal resistances of the liquid layer, phase interface and disjoining pressure, which raises saturation temperature. Disjoining pressure is the interface pressure drop at the boundary of a thin film and is analogous to the Laplace pressure drop on a curved surface [C-1]. The term, α^v_{vol}, is expressed as:

$$\alpha^v_{vol}(x) = 5.6\Pi^2\sqrt{\alpha_{ph}k_l}\left(\frac{\pi}{2} - \arctan\sqrt{\frac{\alpha_{ph}\delta}{k_l}}\right)\frac{\varphi(R^*)}{\sqrt{R^*}}\int_{R^*}^{r_{max}}\frac{f(r)dr}{r}, \tag{5.23}$$

where the term, α_{ph}, represents the heat transfer coefficient at phase change, defined as [S-7]:

$$\alpha_{ph} = \sqrt{\frac{2}{\pi}} \sqrt[3/2]{\frac{1}{\Re}} \frac{P_v h_{fg}^2}{T_v^{5/2}}, \tag{5.24}$$

where $\Re$ is the gas constant for the fluid.

From equation 5.22, evaporation at the menisci of an x position can occur only if the deposit temperature is greater than the saturation temperature corresponding to the vapor pressure at the x position [S-2]. The capillary pressure increases with x, since the liquid pressure decreases with x, while the vapor pressure increases with x (the vapor exits the deposit and the liquid flows into the deposit). As a result, the saturation temperature increases with x. The trends in the model calculations are presented in Chapter 6.

The increase in capillary pressure occurs even if no vaporization occurs in the distance increment (if the deposit temperature is less than saturation temperature at the x position). This result stems from equation 5.15, since a finite change in $R^*(x)$ occurs even if the gradient of the mass flux is zero, provided the mass flux at the location is greater than zero. Alternatively stated, $\frac{dR^*}{dx}$ is not forced to zero when $\frac{dG}{dx} = 0$ as long as $G(x) > 0$. The mass flux is greater than zero if some vaporization occurs at the x position or at larger values of x, where the deposit temperatures are hotter.

The mass flux is then the integral of the incremental production of vapor, expressed by:

$$G(x) = \int_0^x \frac{dG}{dx} dx = \frac{1}{h_{fg}} \int_0^x \alpha_{vol}^v \left[T_d - T_s(P_v) \right] dx \ . \tag{5.25}$$

Equations 5.15, 5.20, 5.22 and 5.25 can be solved once the boundary conditions are defined.

5.4 Boundary Conditions

At x=0, the liquid pressure is equal to that of the bulk fluid or

$$P_l(0) = P_b \tag{5.26}$$

The heat flux is applied at $x = t_d$. Since phase change in the deposit serves as a heat sink, at every cross section, the sum of the heat flux and the product of mass flux and the latent heat term must equal the applied heat flux, q''_o. Therefore, the boundary conditions for heat flux are:

$$q''(t_d) = q''_o,\ G(t_d) = 0 \tag{5.27}$$

$$q''(0) = q''(t_d) - G(0)\, h_{fg}. \tag{5.28}$$

However, $q''(0)$must also satisfy the condition:

$$T_d(0) - T_b = q''(0) / h_c, \tag{5.29}$$

where T_b is the saturation temperature of the bulk flow on the secondary side of the steam generator. h_c represents the Chen heat transfer coefficient. Equation 5.29 demonstrates the coupling between the Chen and Kovalev models.

The determination of $R^*(0)$ warrants explanation. Concurrent with the heat transfer, the hydrodynamics must also be satisfied. The term multiplying $\frac{dR^*}{dx}$ on the left hand side of the equation 5.15 must not be negative. A negative result implies the acceleration loss of the flow is larger than the moving pressure boundary, which induces flow. Therefore, the largest possible value of $R^*(0)$ is set by this condition and the pore size distribution of the matrix. Obviously, the values of $R^*(x)$ are bounded by the maximum and minimum values of the deposit radii. $R^*(x)$ cannot be greater than r_{max} or less than r_{min}. As the position $x = t_d$ is

approached, $R^*(x)$ decreases. Therefore, the minimum radius of the deposit, and the condition that the acceleration loss must not exceed the moving pressure boundary in equation 5.15, limits the lowest value of $R^*(x)$.

No phase change can occur when $R^*(x)$ is equal to the minimum value of the radii, since no liquid can be pulled in through capillary forces without a change in $R^*(x)$. This condition is expressed by:

$$R^*(x) = r_{min} \text{ and } G(x)=0, \tag{5.30}$$

The implication of equation 5.30 is that if G(x)>0 and $R^*(x) = r_{min}$, a larger difference between the maximum and minimum values of radii in the deposit is required to provide enough capillary force to pull in adequate water to sustain evaporation. Therefore, a larger portion of the heat transfer should be attributed to the Chen component to solve the system of equations. Therefore, $T_d(0)$ must increase.

In the cases that

$$G(x)=0 \text{ for } x<t_d \text{ and } R^*=r_{min}, \tag{5.31}$$

the deposit is vapor filled below this x position, and conduction through the matrix alone transfers heat. Since no vaporization occurs, the temperature increases more dramatically than when vaporization aids heat transfer. However, if $R^* > r_{min}$, then more water can be pulled in and evaporated. In this case, a smaller fraction of the heat transfer must be attributed to the Chen component, and $T_d(0)$ must decrease. Therefore, the following condition is invalid:

$$G(x)=0 \text{ for } x<t_d \text{ and } R^*>r_{min}. \tag{5.32}$$

Finally, the condition that the amount of heat transferred in the deposit by phase change must not force the solution that:

$$G(x)>0 \text{ for } x = t_d. \tag{5.33}$$

This condition implies that all of the heat must be transferred by either the Chen or by phase change in the porous media and is implied by equation 5.27. If equation 5.33 is met, then the choice of $T_d(0)$ must increase. A brief description of the solution technique is section 5.5 clarifies this condition.

5.5 Solution Technique

The first step in the solution of the system of equations is the choice of $T_d(0)$ and the calculation of the Chen heat transfer coefficient. In the calculation, T_{wall} is replaced by $T_d(0)$ (see section 5.2). The heat flux, $q^{\cdot}(0)$, and the mass flux, G(0)are then calculated. Using an iterative procedure, $\frac{dR^*(x)}{dx}$ and $\frac{dG(x)}{dx}$ are calculated so that equations 5.15, 5.20, 5.22 and 5.25 are solved subject to the boundary conditions.

A choice of $\frac{dG(0)}{dx}$ is made, and $\frac{dq''(0)}{dx}$ and $\frac{d^2T_d(0)}{dx^2}$ are then evaluated by equation 5.21. Using $q^{\cdot}(0)$, $\frac{d^2T_d(0)}{dx^2}$ and $k_d(0)$, $\frac{dT_d(0_m)}{dx}$ is calculated at the midpoint of the distance step. $k_d(0)$ is evaluated by using the value of $\varphi(0)$ from the choice of $R^*(0)$. The subscript, m, implies that the value is evaluated at the midpoint of the distance step.

Using $\frac{dT_d(0_m)}{dx}$ and $T_d(0)$, $T_d(0_m)$ is evaluated at the midpoint. $\frac{dR^*(0)}{dx}$ is then chosen, and $R^*(0_m)$ is found. The parameters in equation 5.15 are evaluated using $R^*(0_m)$. These parameters include $\varphi(R^*)$, $f(R^*)$, $F(R^*)$. Using the chosen

value of $\frac{dG(0)}{dx}$, $G(0_m)$ is evaluated, and equation 5.15 is solved for $\frac{dR^*(0)}{dx}$. An iterative process continues until the values of $\frac{dR^*(0)}{dx}$ converge.

Using $G(0_m)$, $\frac{dP_l(0)}{dx}$ is evaluated from equation 5.10 and is used to find $P_l(0_m)$. Equation 5.9 yields $P_v(0_m)$, which is used to evaluate $T_s(P_v(0_m))$. The value of $R^*(0_m)$ is used to find $\alpha^v_{vol}(0_m)$, so that $\frac{dG(0)}{dx}$ can be found from equation 5.22. This calculated value is then compared to the chosen value, and the entire process is repeated until the values converge.

The original choice of $R^*(0)$ is set as large as possible to allow for the largest change in $R^*(x)$ before the minimum value is reached, and subsequent conduction across a vapor filled deposit occurs. This choice is restricted by equation 5.15. If the condition described by equation 5.30 is violated or if 5.33 is met, then the original choice of $T_d(0)$ is increased, and the procedure starts from the beginning. If equation 5.32 is met, then $T_d(0)$ is lowered.

The maximum value of $T_d(0)$ is limited to the value that corresponds to 100% of the heat flux being transferred by the Chen component. In this case, the nucleation occurs on the surface of the deposit at the deposit/steam generator secondary side flow boundary. No nucleation occurs in the deposit and the pores are saturated with liquid. The value of $T_d(t_d)$ is equal to the value at $x = 0$ plus the temperature drop across the liquid filled deposit.

The procedure described above is continued, subject to the boundary conditions. The liquid properties, and the conductivity of the magnetite is evaluated at each distance step. The model yields values for all the properties mentioned at each

distance step. Therefore, given heat flux, deposit parameters and flow conditions, the model yields the temperature at the deposit/u-tube boundary and subsequently the drop in temperature from the deposit/u-tube boundary to the bulk flow of the steam generator secondary side.

5.6 Using the Model

A listing of the FORTRAN code that solves the model system of equations is given in Appendix A. Inputs to the code include: bulk flow pressure, mass flux, quality, deposit thickness, permeability, cumulative pore size distribution, porosity and applied heat flux. The code requires a number for each parameter except for the cumulative pore size distribution. The cumulative pore size distribution, $\varphi(r)$, is an algebraic expression that depends on the pore radius, r. The results from mercury porosimetry were curve fit to obtain the expression. The code also requires the minimum and maximum values of radius in the deposit. Furthermore, the derivative of the cumulative pore size distribution, $f(r)$, must also be evaluated as well as the expressions of $\int r^2 f(r)dr$ and $\int \frac{f(r)}{r}dr$. Once the expressions involving the pore size distribution are evaluated, and the values of the other parameters are known, the code will yield the temperature drop across the deposit to the bulk flow.

6 EXPERIMENTAL AND THEORETICAL RESULTS

6.1 Introduction

The deposits were characterized according to thickness, porosity, pore size distribution, composition and permeability. The model incorporating these characteristics was developed and is described in Chapter 5. The calculated results were compared to the experimental data in an effort to determine the accuracy of the model. The experimental and theoretical results of the OD boiling heat transfer runs are compared in Figures 6.1-6.14. The figures are discussed in section 6.2. Section 6.3 contains an error analysis of the OD experimental setup, used in the comparison of section 6.2. The results of the subcooled OD measurements are presented in section 6.4. A parametric comparison of the theoretical and experimental OD and ID boiling results is given in section 6.5.

6.2 Graphical Comparison of OD Experimental Results to Theoretical Model

In Figures 6.1-6.14, the superheat of the wall is plotted versus the applied heat flux for each of the OD boiling heat transfer runs. Wall superheat is defined as T_w-T_b, where T_b is the temperature of the bulk flow in the autoclave, and T_w is the average wall temperature at the applied heat flux.

In Figures 6.1-6.14, the data of the clean and fouled tube are shown to validate the deposit resistance values also depicted on the figures. The concept of deposit resistance is outlined in section 6.5.1. The results of the calculations are also plotted to facilitate the comparison of the experimental data to the predictions of the model. The model calculates the temperature drop across the deposit to the bulk fluid. Therefore, the temperature drop from the centerline of the u-tube (the

assumed location of the thermocouples) to the base of the deposit, calculated in section 6.3, was added to the model results. This value was then compared to the measured results.

Since the thermocouples were imbedded in the walls of the coated u-tubes, and the location of the thermocouples were not known, the comparison of the model results to the data involves error. An error analysis was performed to identify the experimental error associated with the location of the thermocouples and is discussed in section 6.3. The results are plotted as error bars, which bound the fouled tube data. The same error is associated with the clean tubes but is not shown, since the clean tube data were not compared to theoretical values.

The per cent error in the theoretical results compared to the experimental values averaged to be ±17.5 %. The maximum and minimum errors were ±34% and ±2%, respectively.

A summary of the OD heat transfer runs is given in Table 4.1. A summary of the sample characteristics is given in Table 3.1.

6.3 Error Analysis of the OD Setup

An error analysis was performed to identify the experimental error associated with the location of the thermocouples. The thickness of the u-tubes was 1.1176 mm, the outer, r_o, and inner, r_i, radii measured 6.4750 mm and 5.3574 mm, respectively. The thermocouples measured 20 mils in diameter and were placed in holes measuring 21 mils. Since 1 mil is equivalent to 0.0254 mm, the holes measured 0.2667 mm in radius. Machining procedures placed the thermocouples in the middle of the u-tube wall, or on the circumference of a circle with a radius, r_m, of 5.9162 mm. If the thermocouples were misplaced adjacent to the outer wall,

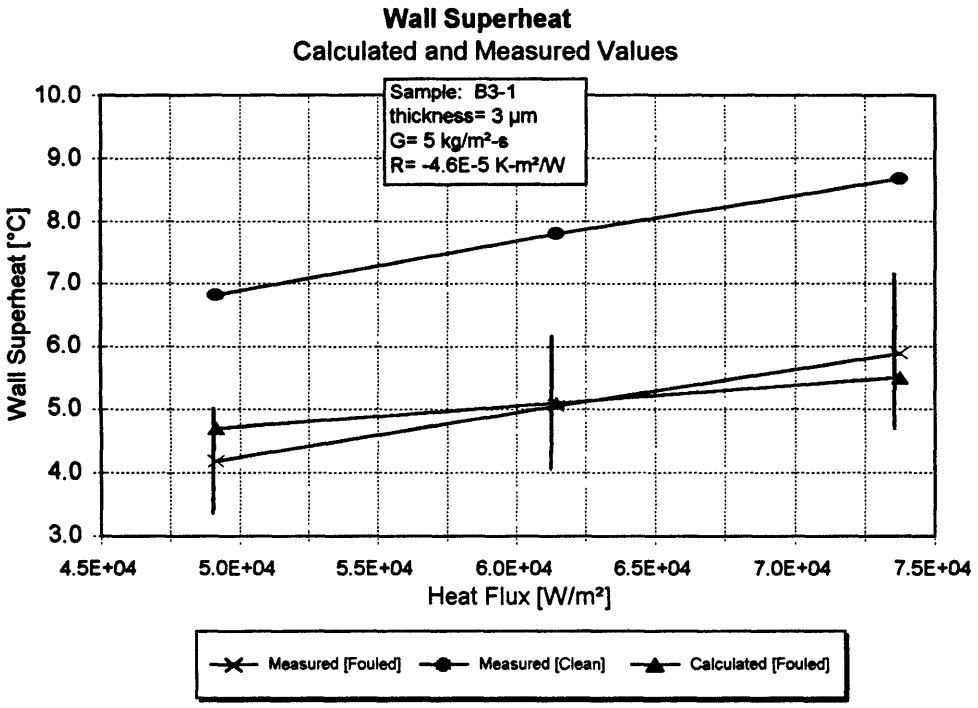

Figure 6.1: Results of B3-1

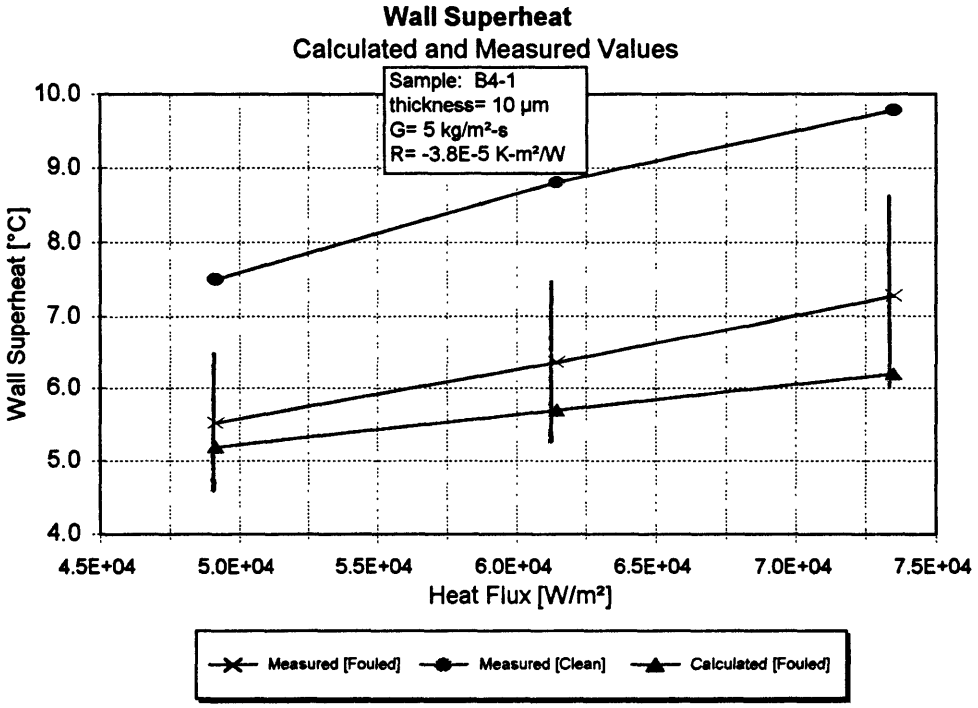

Figure 6.2: Results of B4-1

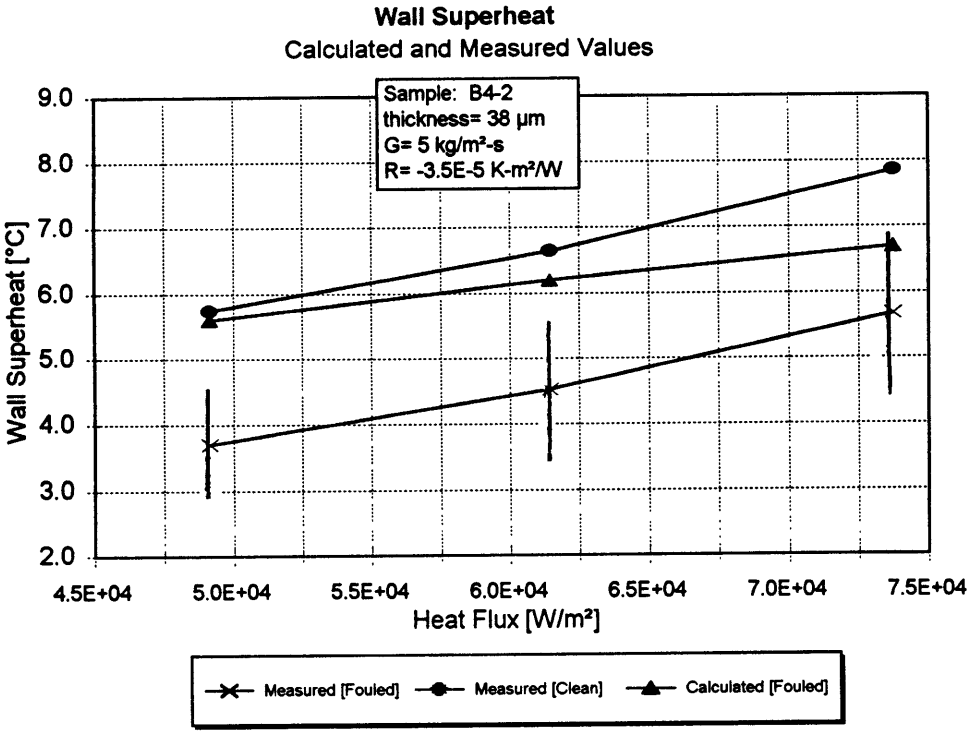

Figure 6.3: Results of B4-2, G(1)

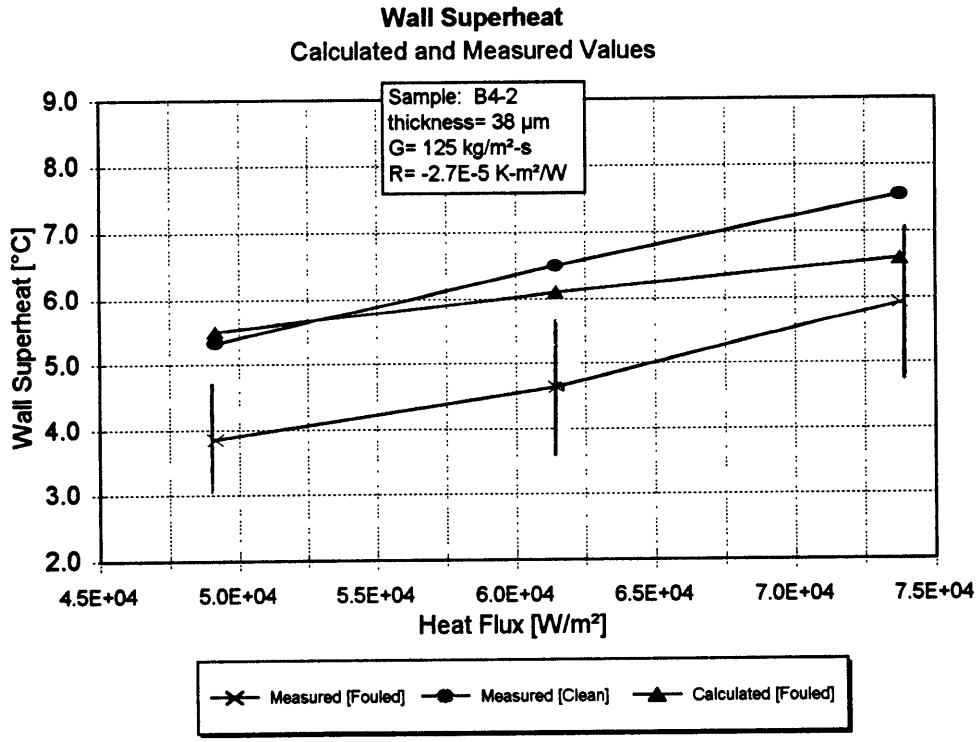

Figure 6.4: Results of B4-2, G(2)

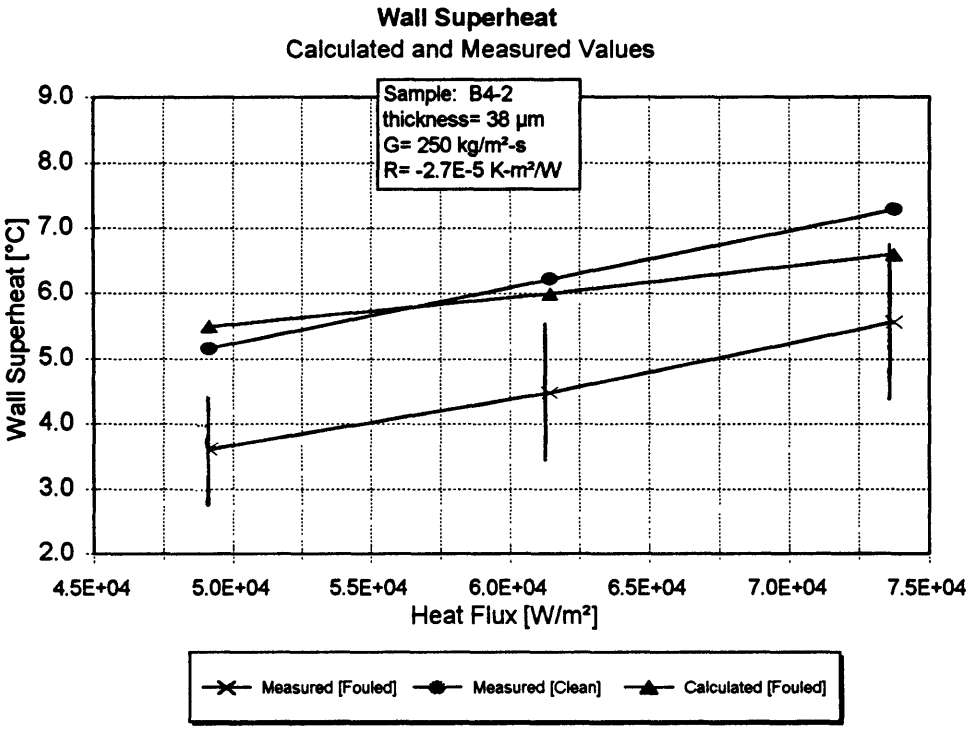

Figure 6.5: Results of B4-2, G(3)

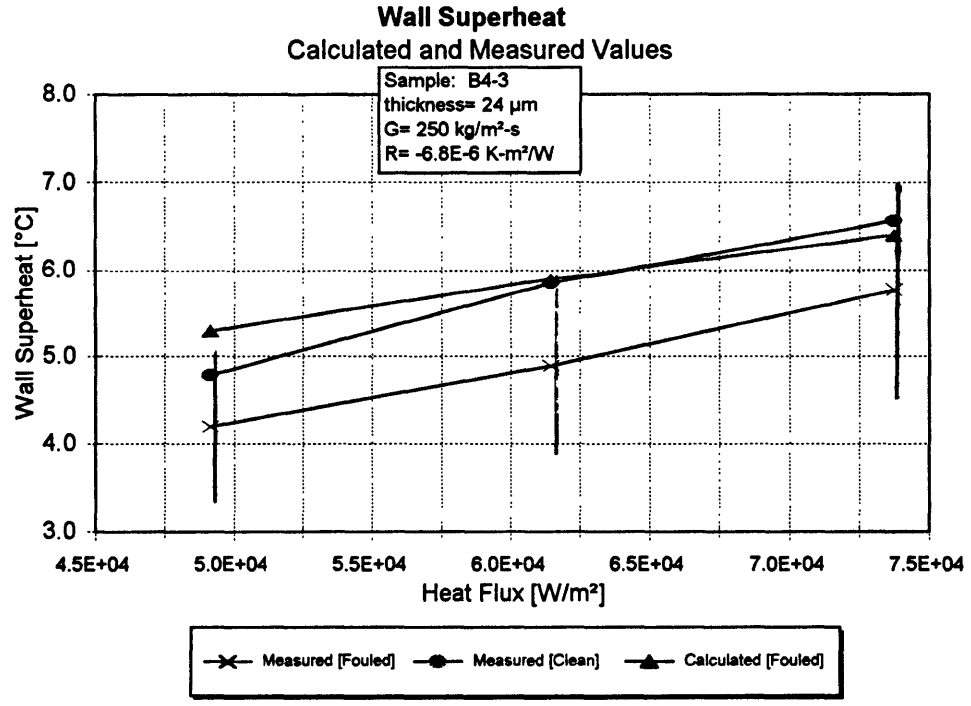

Figure 6.6: Results of B4-3, G(3)

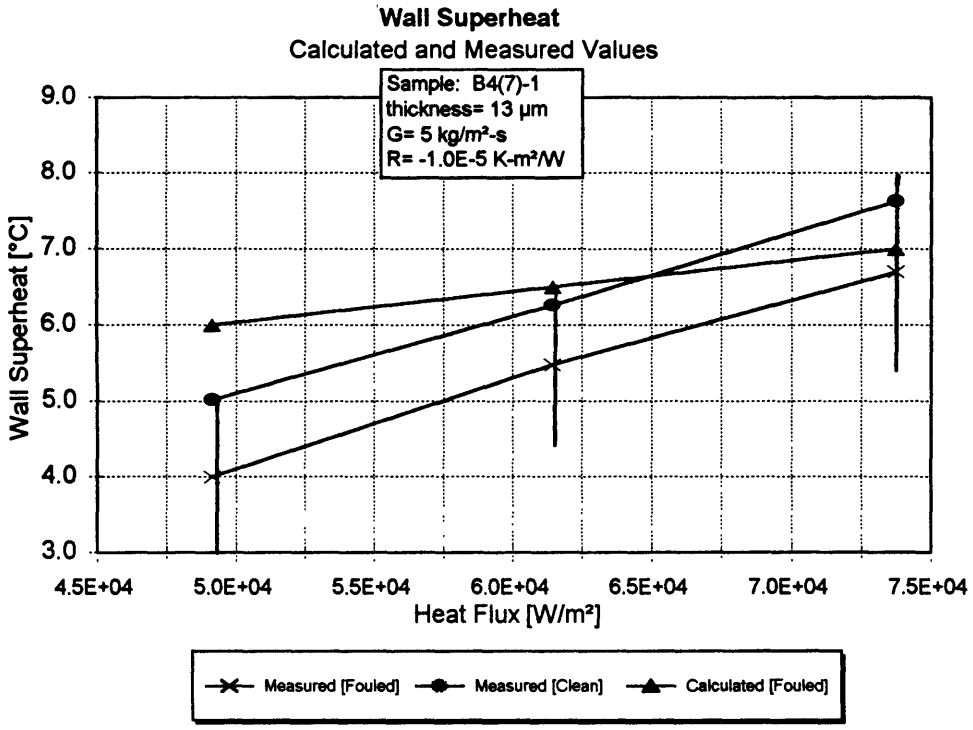

Figure 6.7: Results of B4(7)-1, G(1)

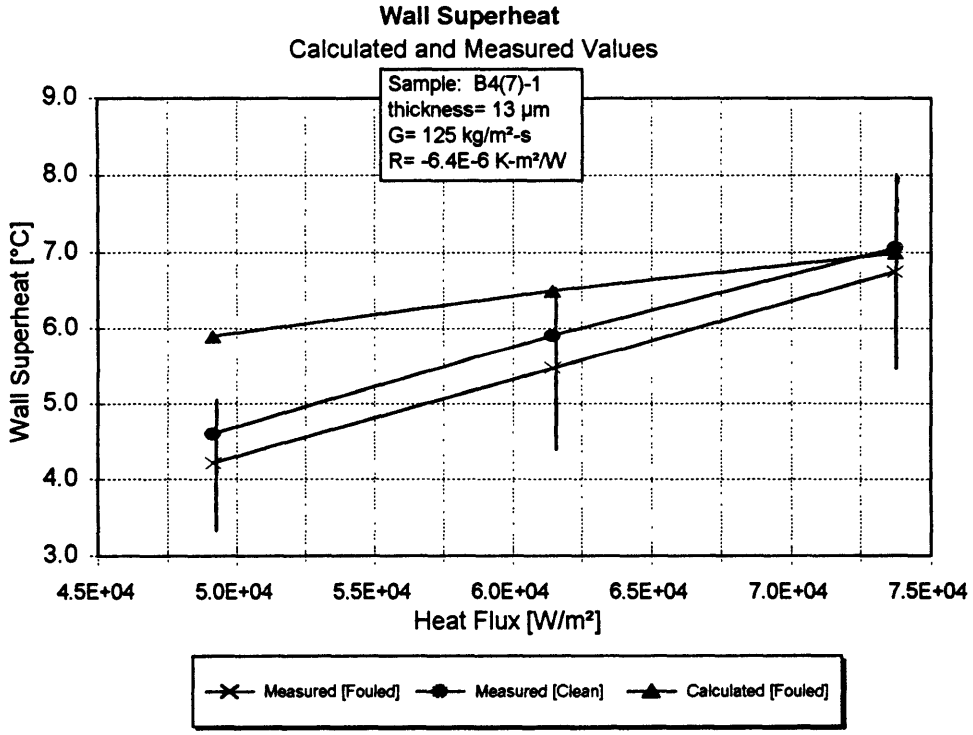

Figure 6.8: Results of B4(7)-1, G(2)

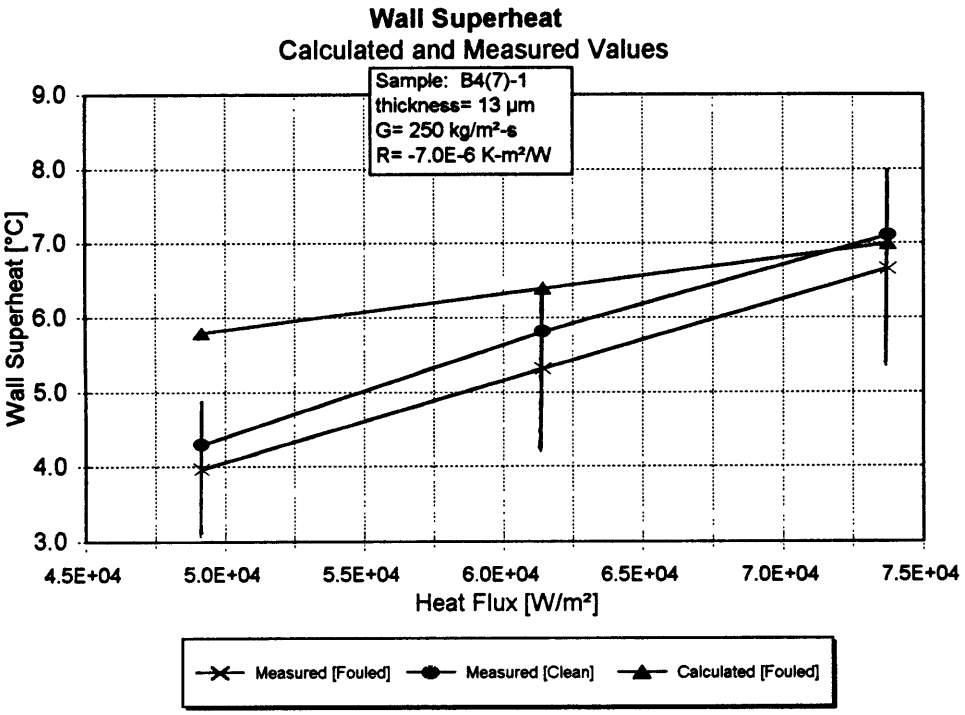

Figure 6.9: Results of B4(7)-1, G(3)

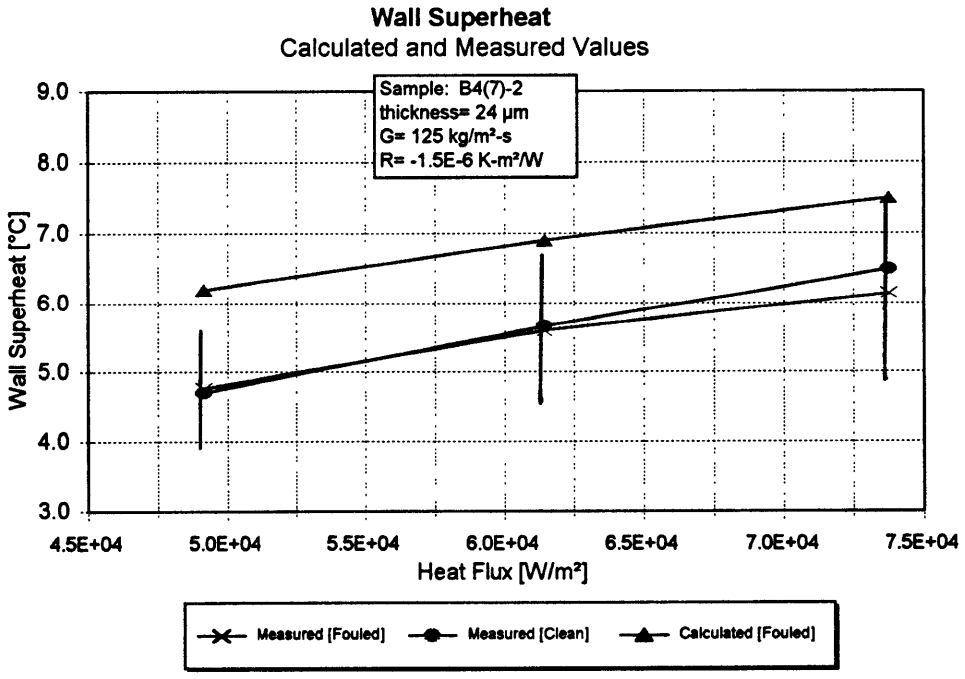

Figure 6.10: Results of B4(7)-2, G(2)

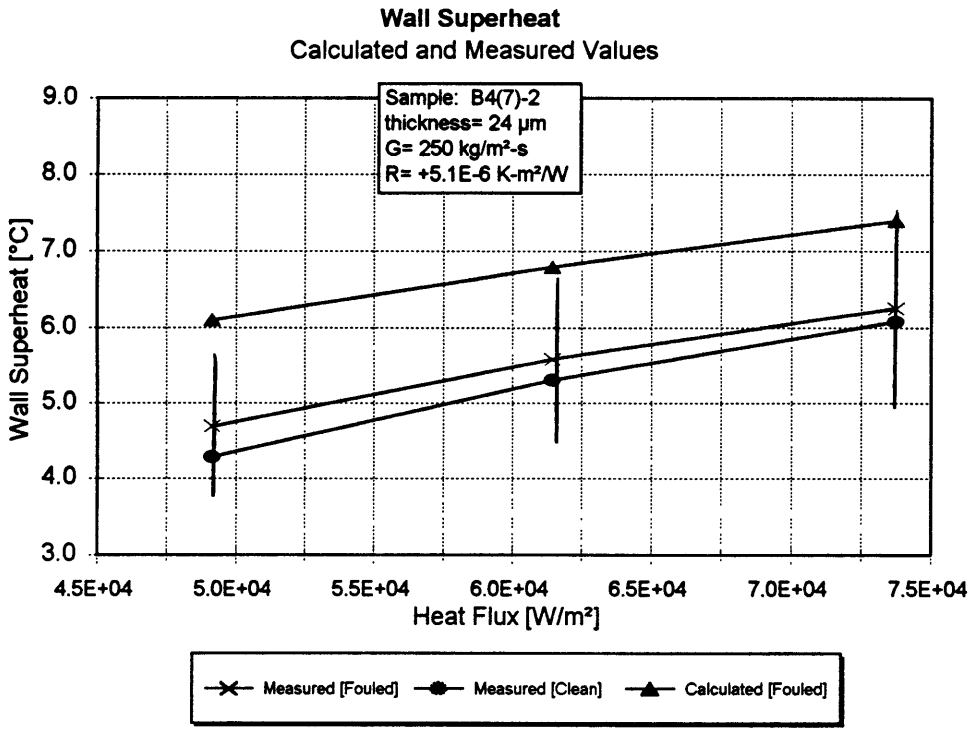

Figure 6.11: Results of B4(7)-2, G(3)

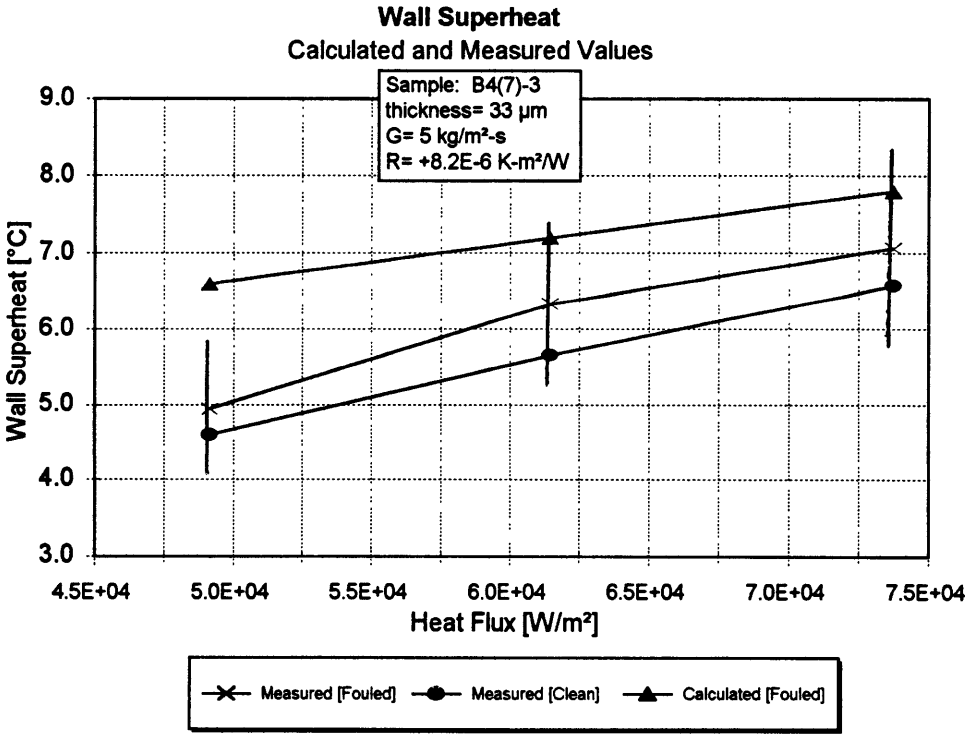

Figure 6.12: Results of B4(7)-3, G(1)

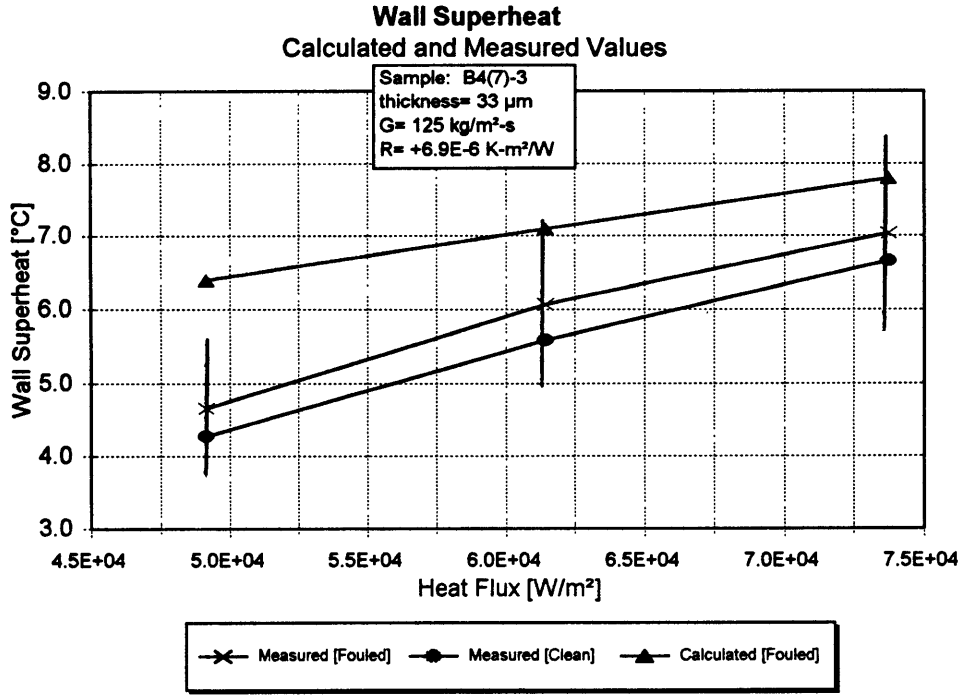

Figure 6.13: Results of B4(7)-3, G(2)

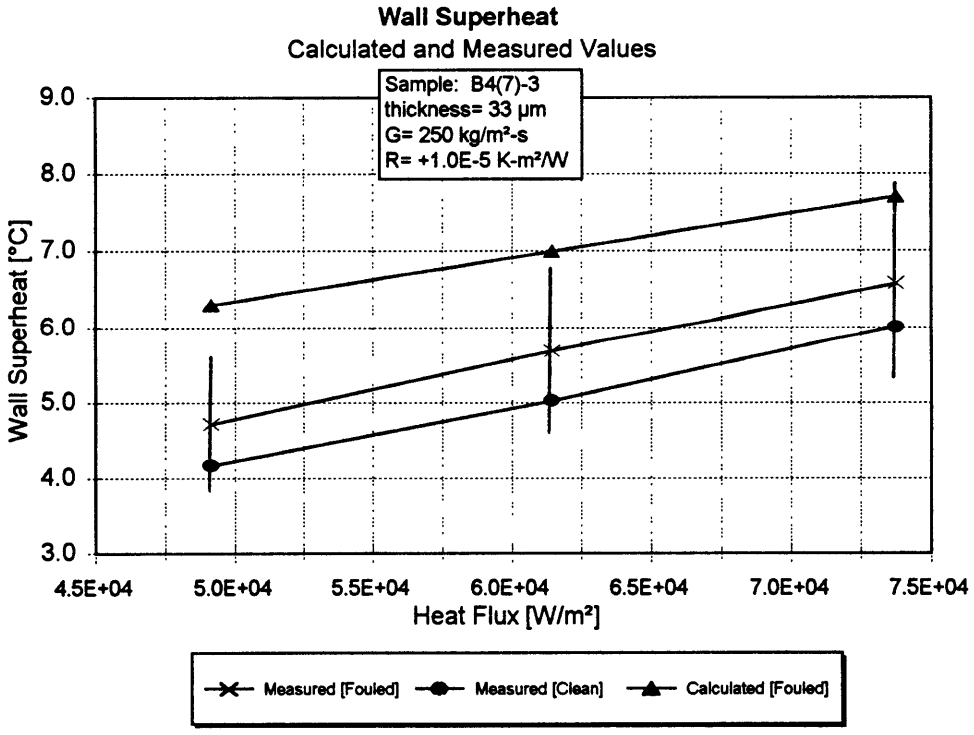

Figure 6.14: Results of B4(7)-3, G(3)

their midpoints would be located at a radius, r_{to}, of 6.2083 mm, or 6.4750 mm minus the radius of the thermocouple hole. If misplaced adjacent to the inner wall, the location, r_{ti}, would be 5.6241 mm. The thermocouple locations at the midpoint and adjacent to the inner and outer walls of the u-tube are shown in Figure 6.15.

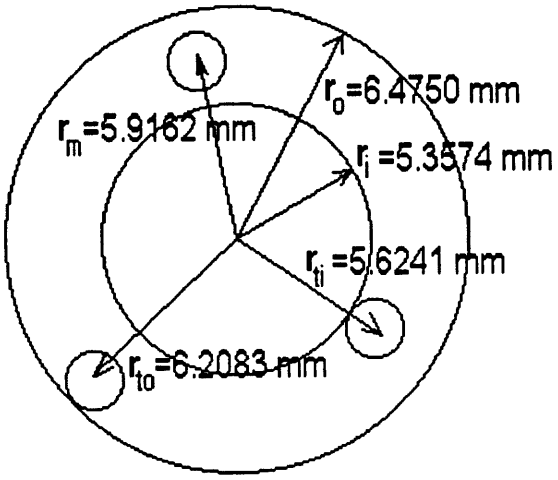

Figure 6.15: The Possible Location of the Thermocouples in the OD Heat Transfer Setup

The temperatures which would have been measured if the thermocouples were located at the inner and outer walls were compared to the temperatures which would have been measured if located at the center line, for the three heat fluxes used in the study. The difference between the assumed center line location and the outer and inner wall locations represents the maximum error in the heat transfer studies. The temperature drop at the center line location (representing one-half of the temperature drop across the u-tube) and the error associated with the location of the thermocouples are listed for the heat fluxes in Table 6.1. The value the I-600 conductivity used in the analysis was 18.21 W/m-K and was evaluated at a wall temperature of 255 °C, a typical value for the measurements performed in the study.

Heat Flux (W/m^2)	Temperature Drop at Center	Error
4.92E4	1.58	+/- 0.86
6.14E4	1.97	+/- 1.08
7.37E4	2.37	+/- 1.30

Table 6.1: Temperature Drop across the U-Tube and Error

Since the difference in temperature between the wall thermocouples and the bulk fluid was measured, it was imperative to determine the offset between the thermocouples of the wall and the bulk fluid. This was done by recording the temperature difference between the wall and the bulk fluid at zero power, when the thermocouples should have read the same temperature. If this difference was not zero, then the difference was then subtracted from the temperature difference when the heat flux was applied. Since even at the highest heat flux the wall thermocouples were elevated no more than 10 °C, it was assumed that this offset did not change. Therefore, virtually no error was associated with thermocouple offset (typically less than 1.0 °C).

6.4 Subcooled OD Measurements

All subcooled measurements on the OD samples were taken at a mass flux of 300 kg/m^2-s. The data were evaluated to determine the thermal conductivity of the deposits, a parameter used in the heat transfer model. The wall temperature elevation, $T_w - T_b$, of the clean tube was subtracted from that of the fouled tube. This value, which represents the temperature drop through the deposit (the temperature drop through the wall cancels out), was then used to evaluate the thermal conductivity of the deposit with use of the following expression:

$$q'' t_d \Big/ \left((T_w - T_b)_F - (T_w - T_b)_C \right) = k_d, \qquad (6.1)$$

where t_d, q'' and k_d are the thickness of the deposit, heat flux and thermal conductivity of the deposit respectively.

It was assumed that the deposits were fully saturated with water during the measurements, so that k_d was the conductivity of the magnetite matrix filled with water [P-2]. Since during the boiling measurements both water and steam filled the matrix, the k_d evaluated in the forced convection studies would overestimate the actual conductivity of the deposit in boiling conditions. Therefore, it was necessary to determine how the conductivities of the magnetite and the water combined to make up k_d, so that the conductivity of the matrix filled with both steam and water could be modeled.

Several models have been suggested to evaluate the conductivity of a porous matrix filled with another medium. Subcooled forced convection studies done by Turner at AECL have shown that the data of k_d for a variety of magnetite deposits were best fit with the following expression [T-4]:

$$k_d = (k_l \Pi + [1 - \Pi] k_m)/2, \qquad (6.2)$$

where k_m, k_l and Π are the conductivities of the magnetite [R-1] and liquid and the porosity respectively. This expression represents half the value of the liquid and matrix conductivities in parallel. This approach was adopted, as the data from this study and that taken by Turner agree reasonably well with the theoretical predictions. The results are shown in Table 6.2. The theoretical and experimental values of k_d are plotted versus porosity in Appendix D.

Sample	Porosity	Measured k_d	Theoretical k_d
B4-2	.46	1.10	1.15
B4-3	.46	1.57	1.16
B4(7)-1	.60	1.02	.95
B4(7)-2	.60	1.40	.95
B4(7)-3	.60	.80	.94

Table 6.2: Experimental and Theoretical Thermal Conductivity of the Deposit Saturated with Subcooled Liquid

In the boiling experiments, the matrix was filled with both liquid and vapor. Therefore, the equation for the conductivity of the matrix becomes:

$$k_d = \left(\left[(1-\varphi)\,k_v + \varphi\,k_l\right]\Pi + [1-\Pi]\,k_m\right)/2, \tag{6.3}$$

where φ and k_v are the fraction of the porosity filled with liquid and the conductivity of vapor, respectively.

6.5 Parametric Trends

The study aimed to identify the effect of deposit characteristics on boiling heat transfer. To determine the effect of deposit thickness, for each batch of magnetite, three OD samples varying in thickness were fabricated. The batches differed in pore size distribution, permeability and porosity. These parameters could not be controlled independently, and their combination is referred to as deposit morphology throughout this text. Three batches were produced, so that three morphologies were represented. In addition, OD measurements were taken at three heat fluxes and three mass fluxes, so the effect of these parameters could be determined. ID measurements were done to determine the effects of mass flux and quality. Therefore, the effect of thickness, morphology, heat flux, mass flux and quality were determined.

This section discusses the effects of all parameters on the boiling heat transfer of magnetite deposits. In addition, it compares the model predictions to the experimental results. Theoretical explanations based on the model are given for each trend.

6.5.1 Data Analysis Techniques

The effects of the parameters measured in the OD boiling experiments were determined using three techniques. If the parameter was studied by comparing different samples, so that the thermocouple locations were not constant (the location of the thermocouples was not known in this study), then the resistance technique was used. The effects of thickness and deposit morphology were evaluated in this manner so that the location of the thermocouples did not impair the comparison. If the parameter was studied by comparing results from the same sample, the thermocouple location did not change and the T_w - T_b values were compared at a particular heat flux. This technique was used to evaluate the effect of mass flux variation. The same principle was used to evaluate mass flux and quality with the ID data. Neither technique was used for heat flux, as described in section 6.5.5.

The following equation was used to calculate the deposit resistance, R_d:

$$R_d = \left((T_w - T_b)_F - (T_w - T_b)_C\right) / q'', \tag{6.4}$$

where the subscripts F and C denote fouled and clean u-tubes (temperature measurements were first done for the fouled sample and then repeated with the same conditions after the deposit was removed).

This resistance technique effectively subtracts out the temperature increase from conduction across the u-tube. Therefore, the locations of the thermocouples did not affect the analysis. The resistances were evaluated at each heat flux and then averaged. The effects of thickness and morphology were deduced by comparing the resistances of the samples at a given mass flux (quality was 5% in each run).

It was straightforward to determine if the experimental mass flux and quality trends matched those of the model, since $T_w - T_b$ values were used. If an increase in mass flux reduced the experimental value, than the same must occur in the calculation. To compare the experimental morphology and thickness trends to those of the model, the deposit resistance was calculated. The $T_w - T_b$ value of the clean u-tube was calculated using the Chen correlation. The model was used to calculate $T_w - T_b$ for the fouled u-tube. The deposit resistance was then calculated with equation 6.4 using these values. Discussion of the heat flux effect is given in section 6.5.5.

6.5.2 Mass Flux

6.5.2.1 Trend

Generally, the mass flux did not seem to affect the heat transfer of the deposits. Figure 6.16 shows the results of sample B4(7)-1 at three mass fluxes and 5% quality. Therefore, the effect of mass flux was evaluated at constant thickness, morphology and quality at three values of heat flux. The $T_w - T_b$ values dropped negligibly as the mass flux was increased from 5 to 250 kg/m^2-s. It is interesting to note that the $T_w - T_b$ values of the clean tube showed more dependence on mass flux than the fouled tube. This same result was found in the ID measurements (Chapter 4). The model also predicts that over the range of mass fluxes studied, the heat transfer of the fouled tube was insensitive to mass flux. The results of the B4(7)-1 calculations are shown on Figure 6.17 for the three mass fluxes. The model only applies to the fouled tube.

6.5.2.2 Theoretical Explanation

It is well documented that mass flux does not increase the boiling heat transfer coefficient of clean tubes dramatically [C-2][C-3]. In fully developed boiling, the

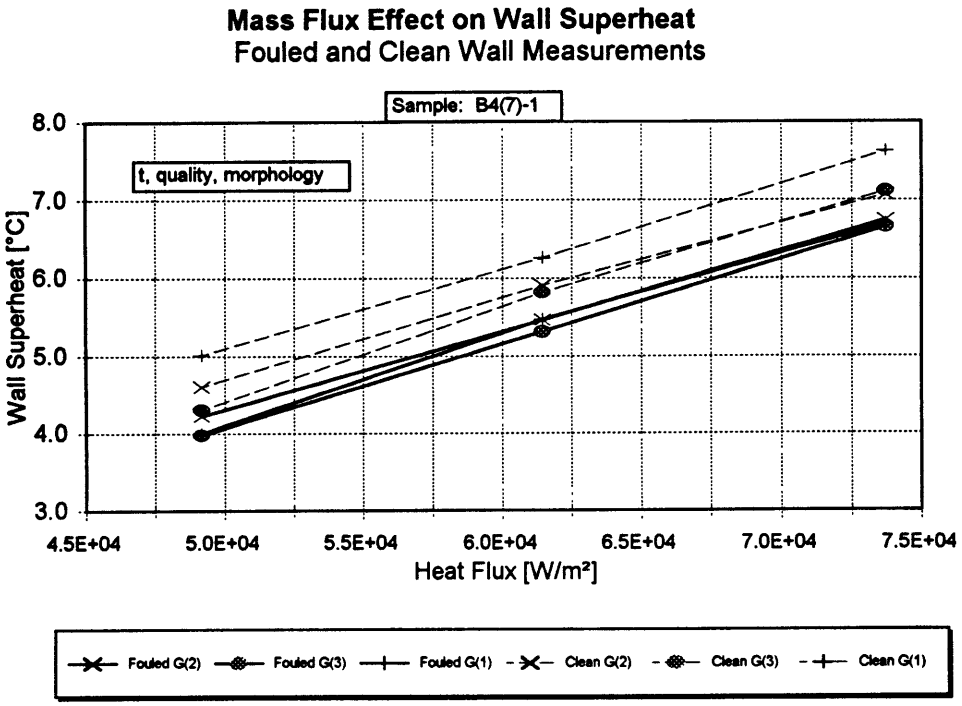

Figure 6.16: The Measured Effect of Mass Flux

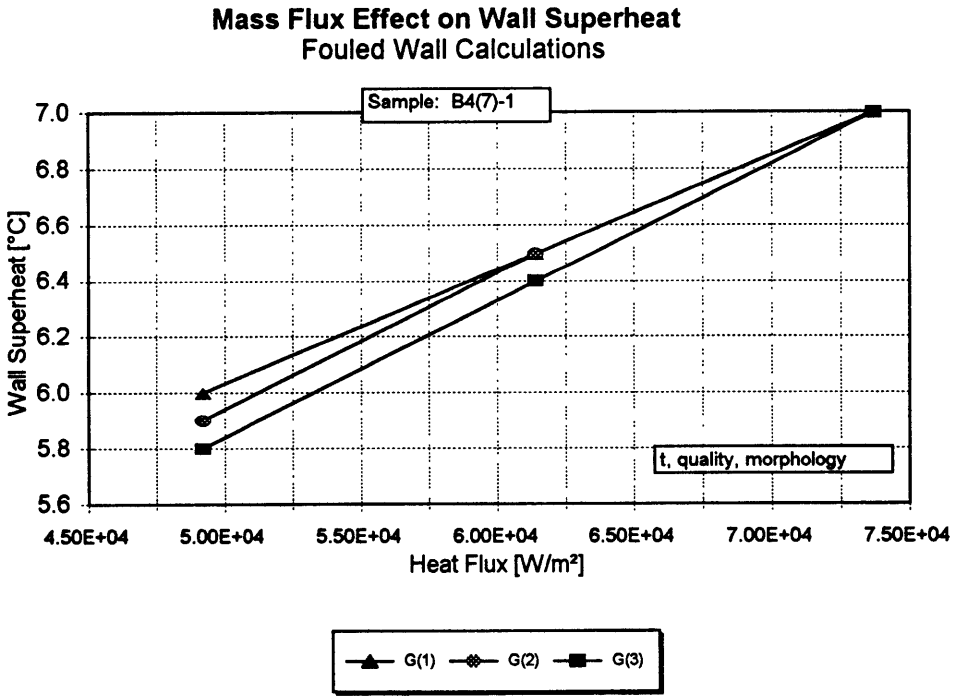

Figure 6.17: The Calculated Effect of Mass Flux

agitation stemming from bubble nucleation at the heated surface increases the Reynolds number in regions close to the wall, disrupting the thermal boundary layer. Since even in turbulent flow, the layer adjacent to the wall is laminar, high flow rates do not agitate the regions near the wall as efficiently as nucleation. Clark and Rohsenow found that at pressures and mass fluxes comparable to those used in this study, the curves of heat flux versus T_w-T_b at different mass fluxes merged at superheats on the order of 10^2. In this study, the superheats were on the order of 10^1, so that according the Clark and Rohsenow data, mass flux slightly affected the heat transfer coefficient of the clean tube. A slight dependence was measured.

From the OD and ID experimental data, the heat transfer coefficient of the fouled tube was insensitive to mass flux over the range of mass fluxes studied. This conclusion is consistent with work done by Macbeth [M-1]. The same argument that applies to the clean tube can be used to explain the lack of dependence on mass flux for the fouled tube. However, the fact that the clean tube was more sensitive to mass flux than the fouled tube warrants consideration.

The model uses the Chen correlation to yield the heat transfer coefficient at the boundary between the deposit and the steam generator secondary side bulk flow. The remainder of the heat flux that did not evaporate in the deposit is then transferred by the Chen coefficient at the boundary. Therefore, the portion of heat that is evaporated in the deposit does not reach this boundary. The increase in mass flux does not affect the evaporation of liquid in the deposit but only reduces the temperature drop due to the remainder that must be transferred at the boundary. Since the heat flux at the boundary is larger for the clean tube, the clean tube is more dependent of mass flux.

6.5.3 Quality

6.5.3.1 Trend

The effect of quality was measured in the ID experiments. It was concluded in this study that an approximately 50% increase in quality (from 20% to 30%) increased the boiling heat transfer coefficient of the clean tube by +3%. This is consistent with the work done by Chen [C-2], where under approximately the same conditions, the same increase in quality increased the heat transfer coefficient by 6%. It was found that over the range of quality achieved in the study, quality had virtually no effect on the fouled tube measurements. Therefore, it is hypothesized that the heat transfer coefficient of the clean tube is more sensitive to an increase in quality than that of the fouled tube. The calculated effect of quality was evaluated for sample B4(7)-1 at a mass flux of G(3) and 5% quality, as shown in Figure 6.18. Therefore, the effect of quality was calculated at constant thickness, morphology and mass flux at three values of heat flux. Only a 0.4 °C decrease in wall superheat was calculated for qualities ranging from 0.01 to 0.20. The model is consistent with the experimental data in predicting virtually no effect of quality on the heat transfer coefficient of the fouled tube.

6.5.3.2 Theoretical Explanation

According to the theory of Chen, an increase in quality affects the heat transfer of a system in the same way as an increase in mass flux, since the Chen correlation is based on the two phase Reynolds number. For this reason, the theoretical explanation of the quality trend is identical to that of mass flux.

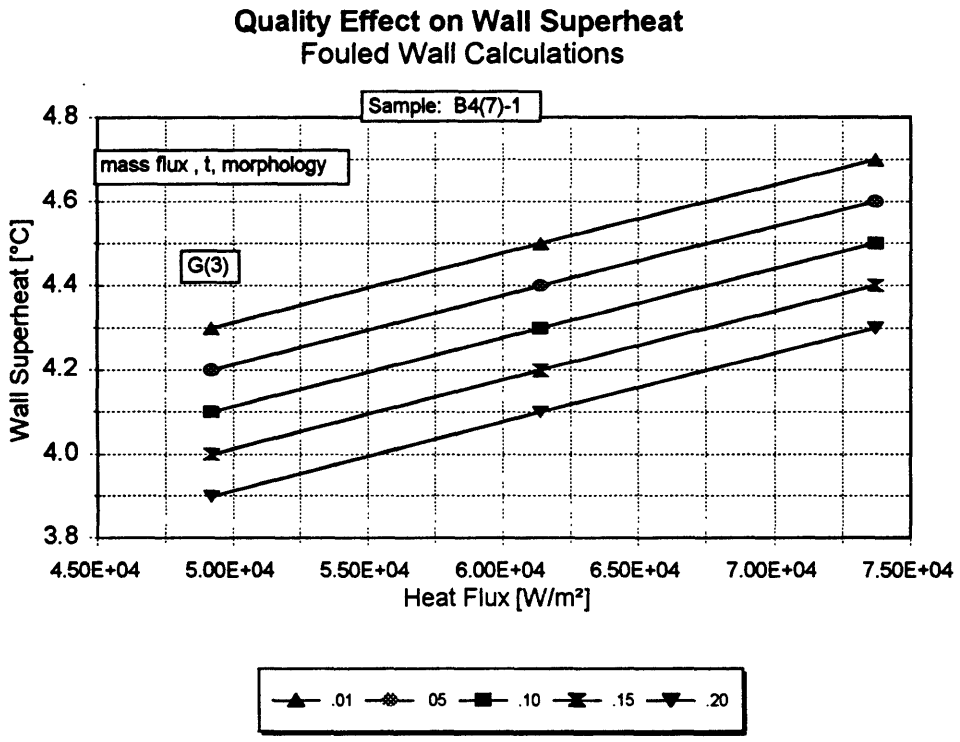

Figure 18: The Calculated Effect of Quality

6.5.4 Thickness

6.5.4.1 Trend

It was found both experimentally and theoretically that an increase in thickness increased the resistance of the deposit. Figures 6.19-6.20 depict the calculated and measured values of resistance averaged over the three values of heat flux for both

B4 and B4(7) at a quality of 5% and three mass fluxes. In the figures, the arrows along the y-axis imply that increasing negative and positive values of deposit resistance respectively correspond to an improvement and hindrance in heat transfer by the deposit as compared to the clean tube. One exception in the

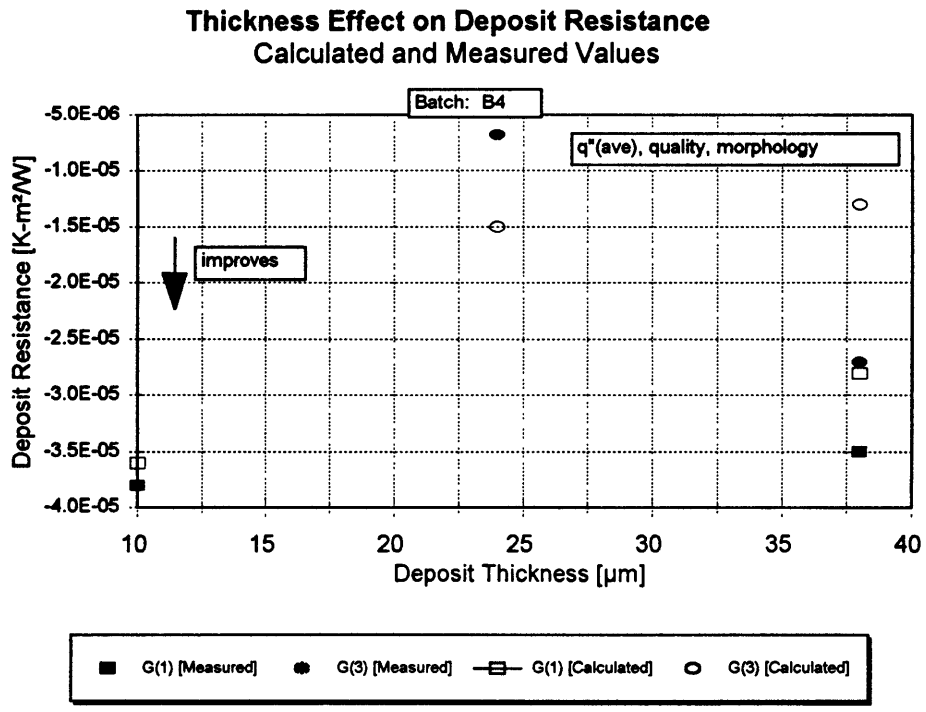

Figure 6.19: The Calculated and Measured Effect of Thickness for B4

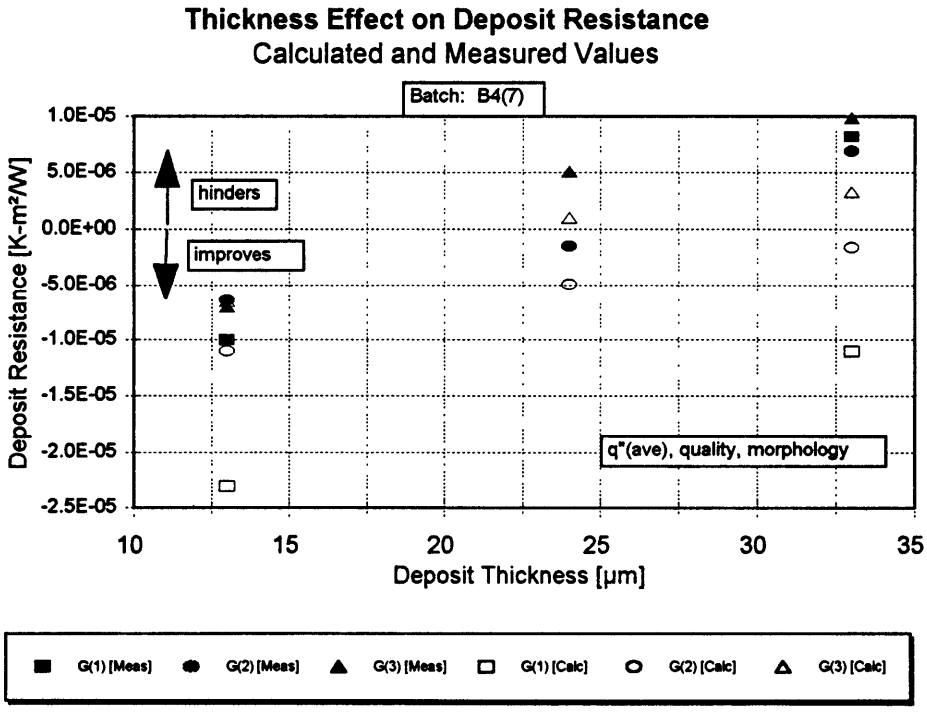

Figure 6.20: The Calculated and Measured Effect of Thickness for B4(7)

thickness trend was noted for the measurements of sample B4-2 (the B4-2 data are plotted at a thickness of 38 μm on Figure 6.19).

6.5.4.2 Theoretical Explanation

In the model calculations, by increasing the thickness of the deposit, the mass flux of vapor exiting and liquid entering the deposit is forced to travel across a larger distance, thereby increasing the liquid and vapor pressure drops. As a result, the capillary pressure in the deposit is larger and nucleation occurs at a higher temperature. Therefore, the temperature drop across the deposit increases, thereby increasing the deposit resistance.

6.5.5 Morphology

6.5.5.1 Trend

Table 3.1 summarizes the sample characteristics. For a given thickness, the B4(7) samples with the smallest pores, lowest permeability and largest porosity yielded a larger resistance than the B4 samples with similar thicknesses. B4 had larger pores, higher permeability and lower porosity. Sample B3-1 yielded the lowest resistance and was consistent with the trend. However, since it was thinner than the other samples, the reduction in resistance stemmed from both the effects of morphology and thickness. However, since B3-1 was only 7 and 10 μm thinner than B4-1 and B4(7)-1, respectively, the effect of morphology presumably outweighed that of thickness, and the resistance of B3-1 is compared to B4-1 and B4(7)-1. Figure 6.21 plots the calculated and measured resistances of B3, B4 and B4(7) as a function of thickness for three levels of mass flux at a quality of 5%. Therefore, the effect of morphology was evaluated at constant average heat flux and quality at three levels of thickness and mass flux. The model calculations showed the same dependence as the measured values.

Since the parameters comprising deposit morphology could not be controlled independently, the exclusive effects of porosity, pore size and permeability were not measured. Calculations were run to determine the theoretical effect of porosity, permeability and pore size. The results are depicted in Figures 6.22-6.24.

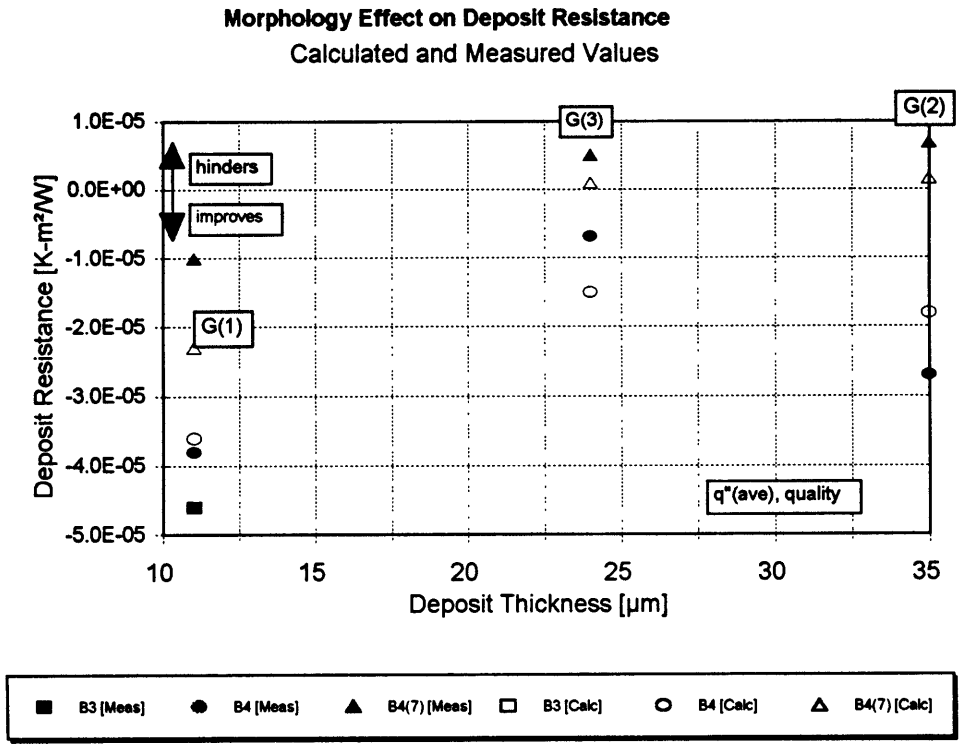

Figure 6.21: The Calculated and Measured Effect of Morphology

6.5.5.2 Theoretical Explanation

This section contains the calculated effects of porosity, pore size and permeability. The base case was run with a permeability of 1.0E-15, a uniform pore size distribution with r_{max} of 0.5 and r_{min} of 0.1 m, a thickness of 10 m, G(3) level of mass flux, 5% quality and a heat flux 7.37E4 W/m^2.

As the porosity increases, the thermal conductivity of the deposit decreases and the conduction of heat that occurs concurrently with evaporation requires a larger

temperature drop. Of course the effect of porosity is more complicated, since a deposit with zero porosity could not transfer heat through evaporation in the deposit. Therefore, there is an optimum value of porosity for a given sample and conditions. Figure 6.22 depicts the deposit temperature drop as a function of porosity.

As the pore size decreases, the capillary pressure increases which elevates saturation temperature. Therefore, the temperature of the deposit increases. Figure 6.23 shows the effect of pore size. The base value of r_{max} was changed from 0.7 to 0.3.

As permeability decreases, the pressure drop through the deposit increases, and the capillary pressure increases, elevating saturation temperature. However, if the permeability is not large enough, then the pores will be saturated and the deposit will have less volume for vaporization. Less heat will be transferred through vaporization in the deposit, and the component transferred by the Chen coefficient at the deposit/bulk flow boundary will increase, thereby elevating wall superheat. Therefore, for the same reason as porosity, there exists an optimum value of permeability for a sample and conditions. Figure 6.24 depicts the effect of permeability.

The model predicts that over the range of parameters studied (see Table 3.1), pore size dominated the heat transfer in a deposit. No other parameter affected heat transfer dramatically.

6.5.6 Heat Flux

6.5.6.1 Trend

The ability of the model to predict the effect of heat flux cannot be evaluated, since the location of the thermocouples is not known, and the increase in T_w - T_b is

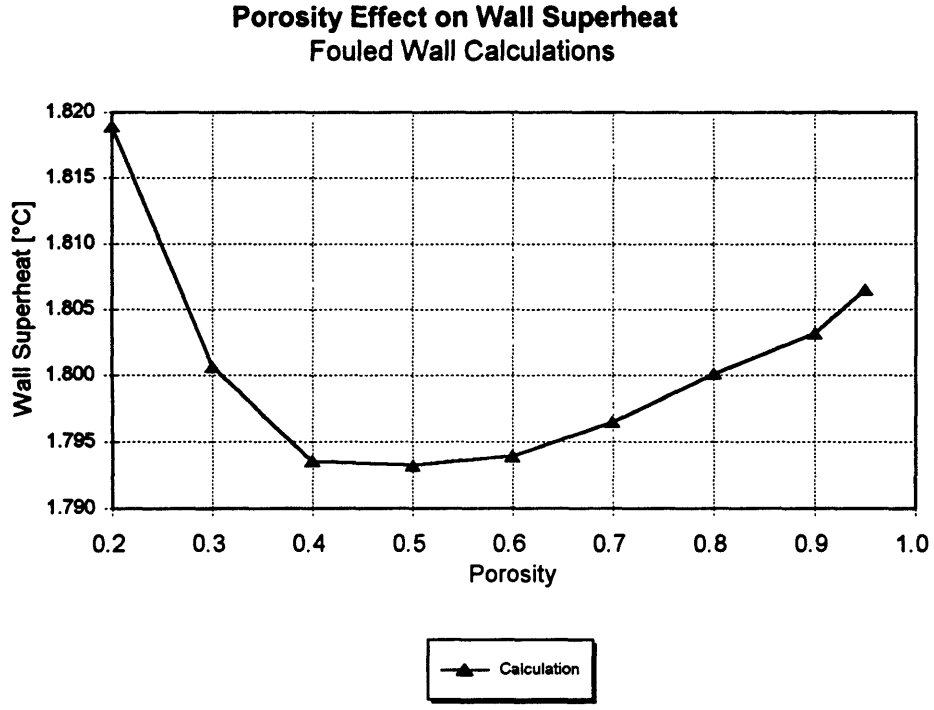

Figure 6.22: The Calculated Effect of Porosity

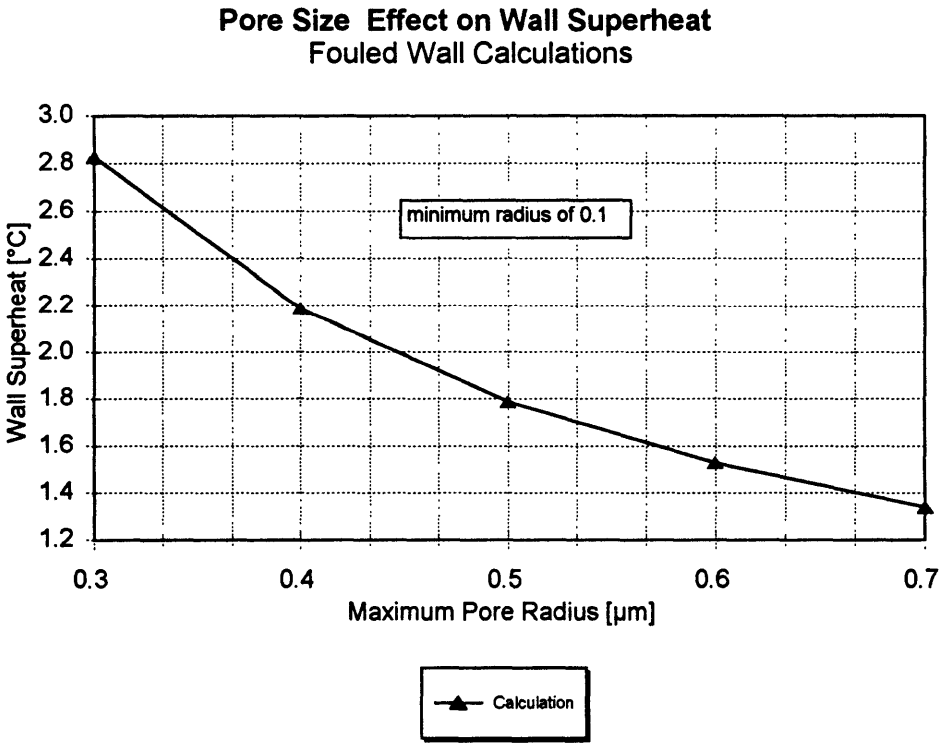

Figure 6.23: The Calculated Effect of Pore Size

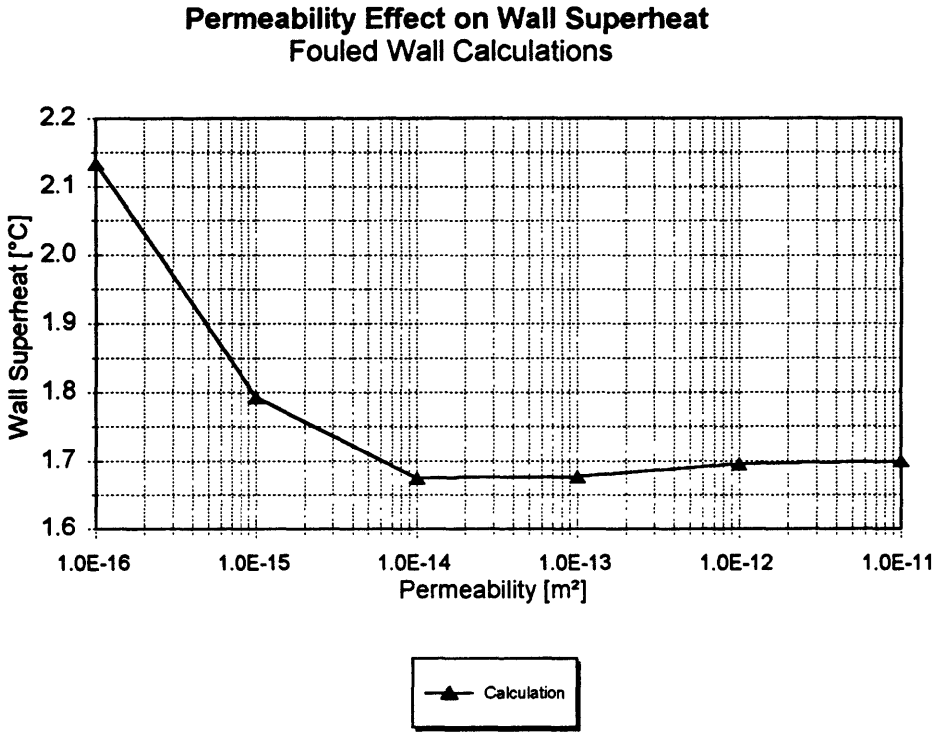

Figure 6.24: The Calculated Effect of Permeability

dependent on their location. The use of the resistance technique cannot be used in determining the effect of heat flux, because the heat transfer coefficient of the bare tube is most likely dependent on heat flux but is not known.

The general agreement between the slopes of the calculated and measured curves in the Figures 6.1-6.14 suggest that the model predictions match the measurements reasonably well. The model predicts that for the given deposit morphologies, the deposit temperature increases with heat flux. This was also the case in the experiments. However, it was not known how much of the temperature increase stemmed from conduction across the u-tube. If the slope of the data were greater than the maximum slope due to conduction across the u-tube, then an increase in deposit temperature with heat flux would have occurred in the measurements. The

maximum slope, m_{max}, with the heat fluxes based on the u-tube outer radius is given by:

$$m_{max} = r_o \ln\left(\frac{r_o}{r_{ti}}\right) \Big/ k_{I600}, \tag{6.5}$$

The value of this slope is 5.0E-5 K-m^2/W. The smallest slope on Figures 6.1-6.14 was measured for sample B3-1 at a value of 5.5E-5. The slopes are depicted in Figure 6.25.

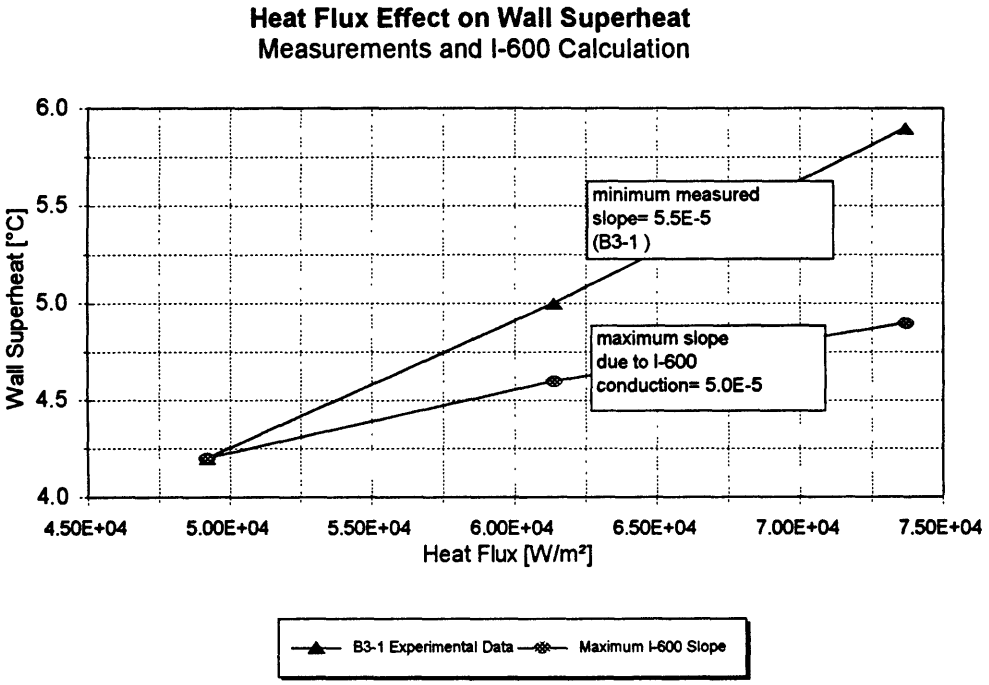

Figure 6.25: The Measured Effect of Heat Flux

Therefore, in all the experiments, the temperature of the deposit increased with heat flux, and the measured increase in T_w - T_b stemmed from the increase in both the deposit temperature and the temperature drop across the u-tube wall. The increase in deposit temperature drop as a function of heat flux at constant mass flux, quality, morphology and thickness is depicted in Figure 6.26. The case was run for B4(7)-3 at G(3) and a quality of 5%. The figure proves that the model

predicted the same effect of heat flux that was measured experimentally. Thinner u-tubes with higher thermal conductivity coated with thicker deposits would more accurately measure the effect of heat flux.

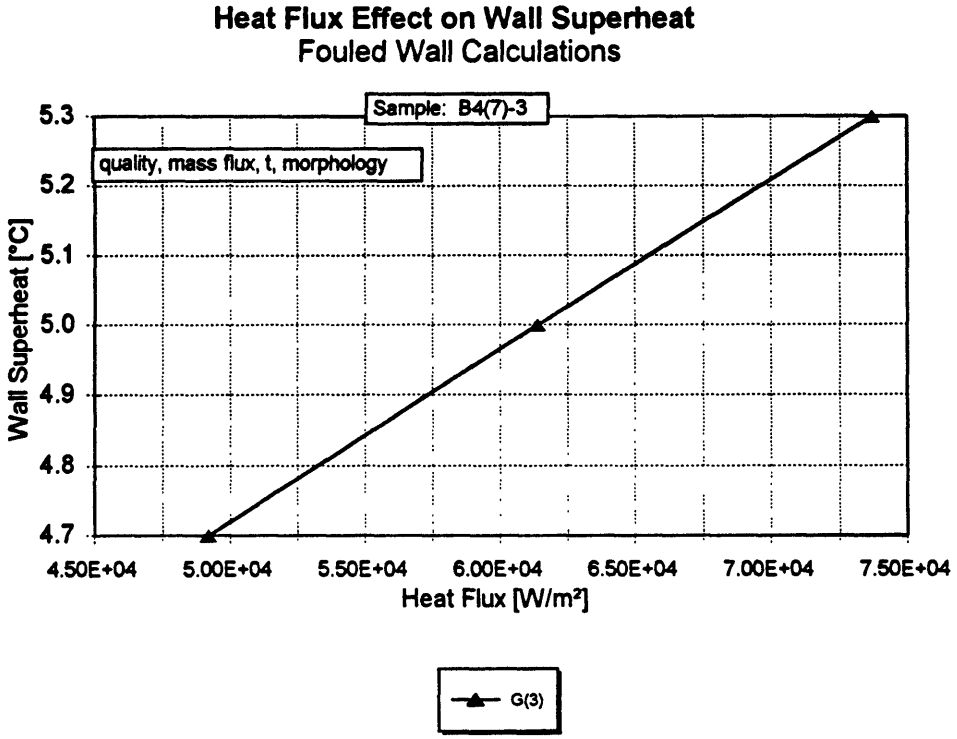

Figure 6.26: The Calculated Effect of Heat Flux

6.5.6.2 Theoretical Explanation

As the heat flux increases, the mass flux of the vapor and liquid increase in the deposit. Therefore, the pressure drop and the capillary pressure increase. As a result, the saturation temperature is elevated and the deposit temperature must increase to initiate phase change.

These effects can be seen in Figures 6.27-6.29, depicting the deposit and saturation temperature, the capillary pressure, and the liquid and vapor pressures, respectively

for the lowest ($q''(1)$) and highest ($q''(3)$) heat fluxes. The calculations were run for sample B4-2 at a mass flux of 250 kg/m^2-s (G(3)) and quality of 5%.

The difference in the y-intercepts of the data plotted in Figure 6.27 represents the difference in the temperature drops for the two heat fluxes due to the transfer of the remainder of the applied heat flux that did not vaporize in the deposit, $q''(0)$, by the Chen component. The slightly larger slope of the $q''(3)$ plot stems from the larger value of heat flux and the smaller value of k_m. For $q''(3)$, since the capillary pressure is higher, the fraction of pores that are filled with vapor is larger than at the lower heat flux, resulting in a lower k_m value. These factors combine to elevate the deposit temperature as heat flux increases. It is interesting to note that the phase change occurs in a region that is adjacent to the u-tube, where the deposit temperature exceeds saturation temperature, provided that dry-out does not occur.

6.6 Summary

The theoretical and experimental results were consistent. Therefore, the model predicted the values of T_w-T_b as well as the dependence of the temperature drop on the studied parameters. Based on the calculated and measured values of deposit resistance, deposits fabricated from B3 and B4 tended to improve the heat transfer of the u-tube, as the resistances were negative for all thicknesses. B4(7)-1 improved the heat transfer but positive resistances were measured for the thicker samples. Thickness did not dramatically affect the heat transfer over the range studied. Since the heat transfer of the bare tube tended to improve more dramatically than that of the fouled tube with mass flux, deposit resistance increased slightly with mass flux. Based on a theoretical sensitivity study, the parameter that dominated the heat transfer of the deposits was the pore size distribution.

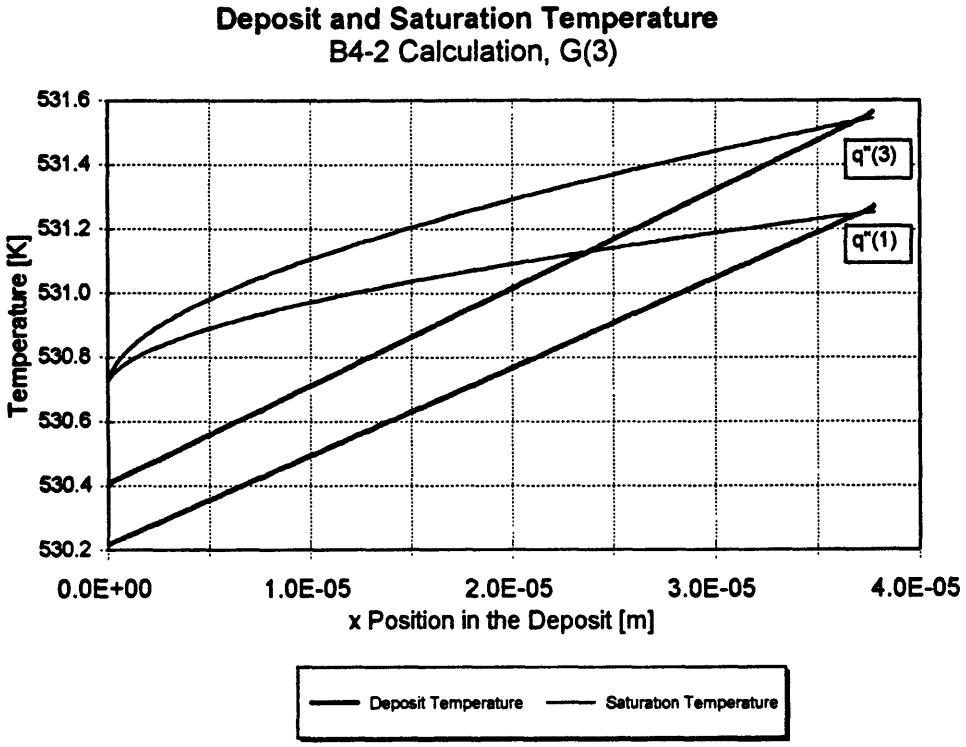

Figure 6.27: Deposit and Saturation Temperature at Two Levels of Heat Flux

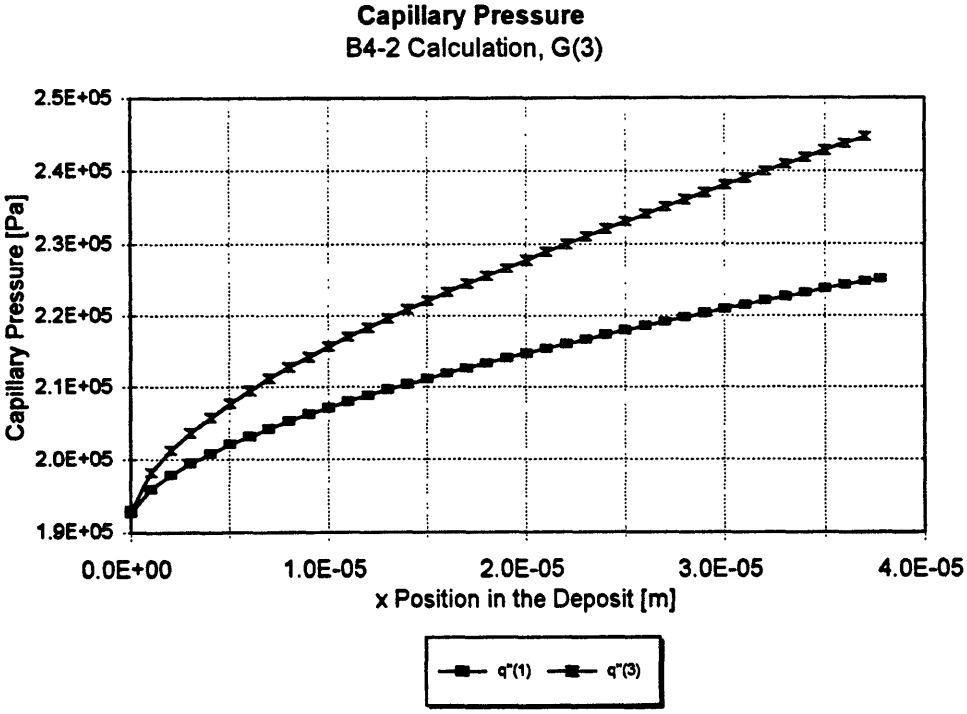

Figure 6.28: Capillary Pressure at Two Levels of Heat Flux

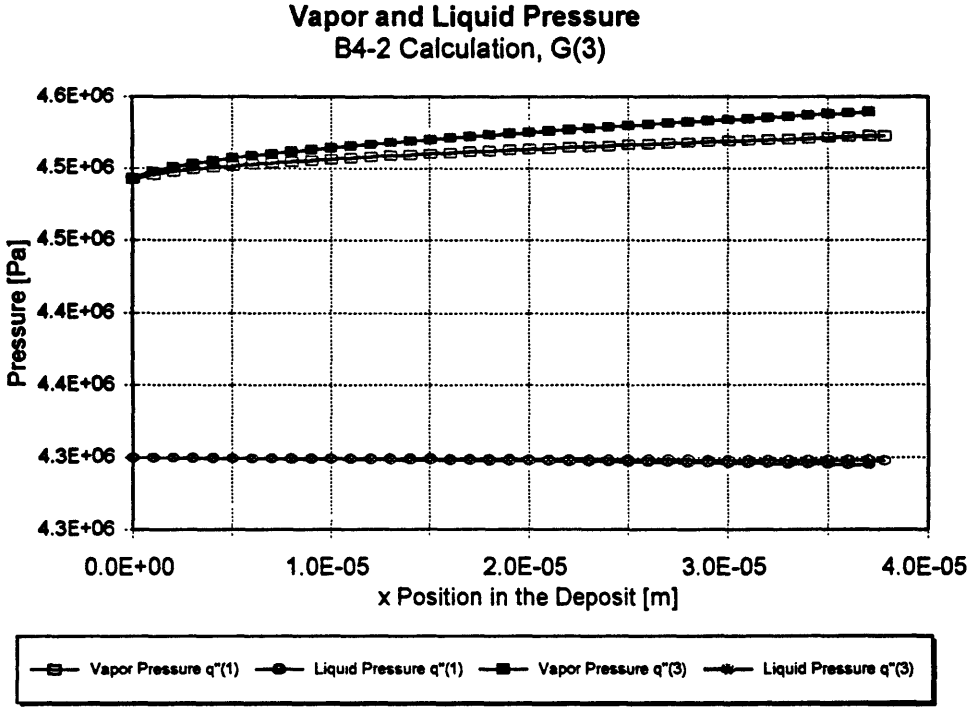

Figure 6.29: Vapor and Liquid Pressure at Two Levels of Heat Flux

Therefore, to use the model to determine the temperature drop across a fouled tube, the pore size distribution must be measured by mercury porosimetry or at least by analysis of a surface SEM micrograph. However, since the other deposit characteristics did not affect the heat transfer dramatically, the characterization process can be minimized by assuming the following values: porosity of 50%, permeability of 5E-15 m^2, a composition comprised of 100% magnetite (30% copper content is found in deposits of systems with brass condensers), thickness measuring 25 μm and a contact angle of 30°. The average steam generator conditions can then be assumed.

7 SUMMARY

7.1 Model Results and Recommendations for Use

The goal of this study was to identify the boiling heat transfer characteristics of steam generator u-tube fouling deposits by developing a boiling heat transfer model and determining its accuracy by comparing the calculated results to experimental values. The effects of the deposit characteristics, heat flux, mass flux and quality on the boiling heat transfer found by both the ID and OD experiments were compared to those determined by the model. The trends in the data were consistent with those predicted by the model. The model results were ±17.5% of the experimental values.

The model system of equations are:

$$\frac{dR^*}{dx}\left\{\frac{2\sigma\cos\theta}{R^*(x)^2}-\frac{G^2(x)f(R^*)}{\Pi^2}\left(\frac{1}{\rho_l\varphi^3(R^*)}+\frac{1}{\rho_v\left(1-\varphi(R^*)\right)^3}\right)\right\}=\frac{G(x)}{\Pi^2}\frac{dG}{dx}*$$

$$\frac{1}{\rho_v\left(1-\varphi(R^*)\right)^2}-\frac{1}{\rho_l\varphi^2(R^*)}\Bigg]+\frac{\nu_l G(x)}{CF(R^*)}+\frac{\nu_v G(x)}{K-CF(R^*)} \qquad (5.15)$$

$$q''(x) = -k_d\frac{dT_d}{dx} \qquad (5.20)$$

$$\frac{dq''}{dx} = -k_d\frac{d^2T_d}{dx^2} = \alpha_{vol}^{v}\left(T_d - T_s(P_v)\right) = \frac{dG}{dx}h_{fg} \qquad (5.22)$$

$$G(x) = \int_0^x \frac{dG}{dx}dx = \frac{1}{h_{fg}}\int_0^x \alpha_{vol}^{v}\left[T_d - T_s(P_v)\right]dx \qquad (5.25)$$

The boundary conditions are numerically expressed by the following:

$$P_l(0) = P_b \qquad (5.26)$$

$$q''(t_d) = q''_o,\ G(t_d) = 0 \qquad (5.27)$$

$$q''(0) = q''(t_d) - G(0)h_{fg} \qquad (5.28)$$

$$T_d(0) - T_b = q''(0) / h_c . \quad (5.29)$$

The terms used in the system of equations and the solution procedure and subsequent numerical restrictions are further described in Chapter 5.

A FORTRAN code was created to solve the model equations, yielding the temperature drop across the deposit to the steam generator secondary side bulk flow. Inputs to the code include: bulk flow mass flux, hydraulic diameter, quality, pressure, liquid contact angle, deposit thickness, composition, permeability, porosity, pore size distribution and applied heat flux. The model is presently solved for the case of constant heat flux. A listing of the code is given in Appendix A.

The deposit pore size distribution was found to dominate the heat transfer of the deposit over the range of parameters studied. Therefore, when using the model, the pore size distribution must be measured. A surface SEM micrograph can be used to quickly estimate the pore size distribution, although mercury porosimetry is strongly recommended. Without further deposit characterization, the model can be used to predict the deposit temperature drop by assuming average values of steam generator conditions, estimating the deposit composition (the deposit composition affects the heat transfer by determining the thermal conductivity of the deposit skeleton), thickness, porosity and permeability and liquid contact angle. It is suggested that the following deposit characteristics be assumed: porosity of 50%, permeability of 5E-15 m^2, a composition comprised of 100% magnetite (30% copper content is found in deposits of systems with brass condensers), thickness measuring 25 μm and a contact angle of 30°.

It was found both theoretically and experimentally that some fabricated deposits improved the heat transfer of the u-tubes, whereas others hindered it. The data were consistent with that of fouled u-tubes pulled from CANDU steam generators.

The Chen correlation and the model were used to calculated the heat transfer coefficient of the clean tube and fouled tube, respectively.

7.2 Applicability of Results to US and Canadian Steam Generators

The accuracy of the model was determined by simulating fouling deposits and flow conditions. The similarity of the conditions and deposits to those of real steam generators warrants consideration. The fabricated deposits were similar to those pulled from CANDU steam generators, and the heat transfer data obtained in this study were consistent with that of fouled CANDU u-tubes. Furthermore, the heat flux, mass flux, quality and water chemistry used in the experiments were generally representative of steam generator conditions. It is therefore postulated that the conclusions drawn in this study apply to the Canadian and US industries.

7.3 Future Work

The model results should be compared to data taken on a larger number of deposits with varying characteristics and over a wider range of conditions. This study has proved that deposits differing in morphology can be fabricated in the laboratory. However, porosity, permeability and pore size distribution could not be varied independently. It would be useful to develop a method of independently controlling these parameters to determine their individual effects in an aim to validate the conclusion that pore size distribution determines the heat transfer of the deposits. This study also identified and successfully implemented methods of characterization, facilitating future work in this area.

The model assumes that the dependence of liquid saturation temperature on pressure is constant and independent of the concentration of non-volatile species in the deposit. It is known that over time, non-volatile species in the liquid will

concentrate as liquid is vaporized in the deposit, thereby elevating saturation temperature. If pressure is reduced, the liquid temperature (near saturation temperature) will drop. Since solubility of a species is strongly dependent on temperature, as the liquid temperature drops, the concentration of the species will decrease. At lower concentration levels, the saturation temperature will decrease as well and according to the model, the heat transfer rate in the deposit will improve. This hysteresis effect has not been validated by this study but the model yields the vaporization rate at each position in the deposit and can be readily coupled with a mass transfer model to determine the concentration rate of non-volatile species in the deposit. Future work should study this hypothesis. Perhaps cycling the steam generator pressure can optimize the heat transfer of fouled tubes.

References

[B-1] Baum, A. J. and Greaney, P. K., "Steam Generator Sludge Pile Model Boiler Testing," EPRI NP1941, July, 1981.

[B-2] Baum, A. J. and Greaney, P. K., "An Experimental and Analytical Investigation of Boiling Heat Transfer in Porous Bodies," *Proceedings of ASME/AIChE National Heat Transfer Conference*, Milwaukee, WI., Aug.,1981.

[B-3] Baum, A. J. and Greaney, P. K., "Steam Generator Sludge Pile Model Boiler Testing Characterization," EPRI NP2041, Sept., 1981.

[B-4] Baum, A. J., "Restricted Geometries and Deposits," The ASME Handbook on Water Technology for Thermal Power Systems, P. Cohen, ed., ASME, 1989.

[B-5] Bushby, S., Personal Communication, June, 1996.

[C-1] Carey, V. P., Liquid -Vapor Phase Change Phenomena, Hemisphere Publishing Corporation, Washington, 1992.

[C-2] Chen, J. C., "A Correlation for Boiling Heat Transfer to Saturated Fluids in Convective Flow," *Ind. Eng. Chem. Proc. Design and Dev.*, Vol. 5, No. 3, 322-339, 1966.

[C-3] Clark, J. A. and W. M. Rohsenow, "Local Boiling Heat Transfer at Low Reynolds' Numbers and High Pressures," MIT Division of Industrial Cooperation, DIC Project No. 6627, NR 035-267, July, 1952.

[C-4] Cohen, P., "Heat and Mass Transfer for Boiling in Porous Deposits with Chimneys," *AIChE Symposium Series 20*, No. 138, 71-80.

[C-5] Collier, J. G., Forced Convective Boiling, in *Two-Phase Flow and Heat Transfer in the Power and Process Industries*, A. E. Bergles, J. G. Collier, J. M. Delhaye, G. F. Hewitt, and F. Mayinger, Eds., Hemisphere, New York, 1981.

[C-6] Cooks, F. H., "Manual of Industrial Corrosion Standards and Control," ASTM Special Technical Publication 534, p. 263, 1973.

[C-7] Corey, A. T., Mechanics of Heterogeneous Fluids in Porous Media, Water Resources Publications, Ft. Collins, Co., 1977.

[D-1] Dullien, F. A. L., Porous Media: Fluid Transport and Pore Structure, Academic Press, New York, 1979.

[F-1] Forster, H. K. and Zuber, N., "Dynamics of Vapor Bubbles and Boiling Heat Transfer," *AIChE Journal*, Vol. 1, No. 4, 531-535, 1955.

[G-1] Groenveld, D. C. and Mancini, F., "Tables of Thermodynamic Properties and Heat Transfe Properties for Steam and Water," CRNL-1533, 1976.

[G-2] Guzonas, D., Personal Communication, Aug., 1996.

[H-1] Hamilton, H., Personal Communication, Sept., 1995.

[H-2] Hewitt, G. F. and Roberts, D. N., "Studies of Two-phase Flow Patterns by Simultaneous X-ray and Flash Photography," AERE-M 2159, Her Majesty's Stationary Office, London, 1969.

[H-3] Hsu, Y. Y., "On the Size Range of Active Nucleation Cavities on a Heating Surface," *J. Heat Transfer*, Vol. 84, 1962.

[J-1] Jennings, J. D. and Udell, K. S., "The Heat Pipe Effect in Heterogeneous Porous Media," *Journal of Heat and Mass Transfer*," Vol. 105, 485-492, Aug., 1983.

[K-1] Kovalev, S. A. and Solovev, S. I., "Model of Heat Transfer in the Boiling of Liquid at a Porous Surface," *Teplofizika Vysokikh Temperatur*, Vol. 22, No. 6, 1166-1171, Nov./Dec., 1984.

[K-2] Kovalev, S. A., Solovev, S. I., Ovodkov, O. A., "Liquid Boiling on Porous Surfaces," *Heat Transfer-Soviet Research*, Vol. 19, No. 3, May/June, 1987.

[K-3] Krokhin, Y. I. and Kulikov, A. S., "Approximate Hydrodynamic Theory of the Evaporative Process in Capillary-Porous Structures," *Teplofizika Vysokikh Temperatur*, Vol. 21, No. 5, 952-958, Sept./Oct., 1983.

[L-1] Lavoie, P., Personal Communication, March 1995.

[L-2] Lavoie, P., Personal Communication, May 1995.

[L-3] Lorenz, J. J., "The Effect of Surface Conditions on Boiling Characteristics," Ph.D. Thesis, Dept. of Mech. Eng., M.I.T., 1971.

[L-4] Luikov, A. V., "Systems of Differential Equations of Heat and Mass Transfer in Capillary-Porous Bodies," *International Journal of Heat and Mass Transfer*, Vol. 18, 1-14, 1975.

[M-1] Macbeth, R. V. et al., "An Investigation Into the Effect of Crud Deposits on Surface Temperature, Dry-out and Pressure Drop With Forced Convection Boiling of Water at 69 Bar in an Annular Test Section," AEEW-R-705-Winfrith, May, 1971.

[M-2] Macbeth, R. V., "Boiling on Surface Overlaid with a Porous Deposit: Heat Transfer Rates by Capillary Action," AAEW-R711, June, 1971.

[M-3] Martinelli, R. C. and Nelson, D. B., Prediction of Pressure Drop During Forced-Circulation Boiling of Water, *Trans. ASME*, Vol. 70, 695-702, 1948.

[M-4] Millett, P. J. and Fenton, J. M., "A Review of PWR Steam Generator Crevice Impurity Concentration Mechansims," *Proc. Steam Generators and Heat Exchanger Conf.*, Canadian Nuclear Society, Toronto, ON., April 30-May 2, 1990.

[M-5] Millett, P. J. and Fenton, J. M., "A Modeling Study of Parameters Controlling Local Concentration Processes in Pressurized Water Reactor Steam Generators," *Nuclear Technology*, Vol. 108, 256-265, Nov., 1994.

[P-1] Pietralik, J., Personal Communication, Dec., 1996.

[P-2] Powell, R. W. et al., "Thermal Conductivity of Certain Liquids," Chemical Rubber Company Handbook of Chemistry and Physics, 61st Edition, 1980.

[P-3] Pratt, A. W., "Heat Transfer in Low Conductivity Materials," Thermal Conductivity, Vol. 1, ed. R. P. Tye, Academic Press, New York, 1969.

[R-1] Rassokhin, N. G. et al., "Thermal Conduction of Deposits of Iron Oxides," *Teploenergetika*, Vol. 20, No. 9, 12-15, 1973,

[S-1] Scheidegger, A. E., The Physics of Flow through Porous Media, University of Toronto Press, Toronto, 1974.

[S-2] Schuh, M. J. and Udell, K. S., "A Study of the Thermodynamics of Evaporation and Condensation in a Porous Medium," Transactions of the ASME/AIChE National Heat Transfer Conference, 1985.
[S-3] Singh, A., "Effects of Surface Conditions on Nucleation and Boiling Characteristics," Sc.D. Thesis, Dept. of Mech. Eng., M.I.T., 1974.
[S-4] Smith, D., Personal Communication, April, 1996.
[S-5] Solovev, S. I. and Kovalev, S. A., "Heat Transfer in the Evaporation of Liquid on a Porous Surface," *Teplofizika Vysokikh Temperatur*, Vol. 22, No. 3, 528-536, May/June, 1984.
[S-6] Sugimoto, T. and Matijevic, E., "Formation of Uniform Sperical Magnetite Particles by Crystallization from Ferrous Hydroxide Gels," *Journal of Colloid and Interface Science*, Vol. 74, No. 1, March, 1980.
[S-7] Sukhatme, S. P. and W. M. Rohsenow, "Heat Transfer During Film Condensation of a Liquid Metal Vapor," Journal of Heat Transfer, Vol. 88, No. 1, 19-27, Feb., 1966.
[T-1] Thom, J. R. S., "Prediction of Pressure Drop During Forced Circulation Boiling of Water," *Int. J. Heat Mass Transfer*, Vol. 7, p. 709, 1964.
[T-2] Turner, C., Personal Communication, March 1995.
[T-3] Turner, C., Personal Communication, May 1995.
[T-4] Turner, C., Personal Communication, Nov., 1995.
[T-5] Turner, C., Personal Communication, Feb., 1996.
[T-6] Turner, C., Personal Communication, May, 1996.
[U-1] Udell, K. S., "Heat Transfer in Porous Media Considering Phase Change and Capillarity-- The Heat Pipe Effect,"*International Journal of Heat Transfer*, Vol. 28, No. 2, 485-495, 1985.
[W-1] Whalley, P. B., Boiling Condensation, and Gas-Liquid Flow, Clarendon Press, Oxford, 1987.

Appendix A

Listing of FORTRAN Code to Solve the Model System of Equations

```
c     Boiling Heat Transfer in Steam Generator U-Tube Fouling Deposits
c     Kovalev model, Chen models
c     name:  deposit.for
c     steam/water conditions for 4.0-5.0 MPa, surface tension 4.0-6.0 MPa
c     see description of variable meaning in text following
c     variables arrayed to 500
c     loop increments:  iteration to converge drl 1-100
c                       iteration to converge gql 1-20
c                       to evaluate r(1), hrlc 1-50
c=====================================================================
c
c     VARIABLE DECLARATION
c
c=====================================================================
c     parameters tracked for each distance step
        real g(1:500),r(1:500),dr(1:500),pl(1:500)
        real gp(1:500),tp(1:500),tsk(1:500),q(1:500)
        real pc(1:500),dx(1:500),pv(1:500),x(1:500)
c     parameters tracked during the iteration process
        real tpl(1:20),gql(1:20),gpl(1:20)
        real gml(1:20),gtp(1:20),drl(1:100)
        real*8 tskm(1:20)
c     parameters tracked to match boundary conditions
        real hrc(1:50)
        real ri
c     deposit paramters
        real p,c,pm,rmax,rmin,l
```

```
c     steam and water conditions
        real dl,dv,hfg,t,ml,mv,nl,nv,tcl,tcv,rst,aph,cp,theta
c     boundary heat addition and flow conditions
        real*8 shf
        real press,d,xtt,qual,re,pr,mf,fxtt,oxtt,hfx,retp
        real hmic,hmac,hc,pwall,cpc,hfgc,tclc
c     evaluated in loop iteration
        real tcm,tcd,tsml,stl,gpml,drr,ps,f
        real dcv,dcl,cfr,hrn,hrd,hrl,dpl,nll
        real*8 ifroru,ifrorl,ifror,rml
        real*8 cf,cfu,cfl,pmv,pml,pcml,aml
c     constants or user input
        real gcst,pi,step,gc
c     final conditions
        real rl,dt,hd,tbd
c     integers serve as counts in loops
        integer k,n,j,rmlc,hrlc,dxc,rmldxc
c     character string to write code status to output file
        character*50, fault
c
c=====================================================================
c
c     FORMAT STATEMENTS
c
c=====================================================================
4000  format (a)
5000  format (i5,i5,i5,f15.10,f15.10,f15.12)
6000  format (i5,i5,i5,f15.5,f15.5,f15.12)
7000  format (f30.10,f20.10,f20.10)
9000  format (i5,f15.10,f15.10,f15.10,f25.15,f25.15,f25.15)
```

```
8000   format (f30.25,f30.25,f30.15)
c
c=======================================================================
c
c     OPENING OUTPUT FILE
c
c=======================================================================
      open(unit=100,file='value.dat',access='sequential',
     +  form='formatted')
      print *, 'what is shf?'
      read*, shf
c
c=======================================================================
c
c     INITIALIZING VARIABLES
c
c=======================================================================
      n=1
      hrlc=1
      rmlc=0
      j=1
      k=1
      dxc=1
      rmldxc=1
c
c=======================================================================
c
c     SETTING VARIABLE VALUES
c
c=======================================================================
```

```
c++++++++++++++++++++++++++++++++++++++++++++++++++++++++++++++++
c     STEP SIZE
c++++++++++++++++++++++++++++++++++++++++++++++++++++++++++++++++
        step=1.0e-7
c
c++++++++++++++++++++++++++++++++++++++++++++++++++++++++++++++++
c     DEPOSIT MORPHOLOGY
c++++++++++++++++++++++++++++++++++++++++++++++++++++++++++++++++
        ri=.99
c     R VALUES MUST BE IN METERS
c     B4(7)
c      rmin=0.035e-6
c      rmax=.2e-6
c      p=0.6
c      pm=1.0e-17
c      l=33.0e-6
c      c=pm/(5.952381e5*rmax**3-1.0e7*rmin**3)
c      cfl=1.0e7*rmin**3
c      ifroru=1.166045e6*log(rmax)
c     B4
        rmin=0.035e-6
        rmax=0.2296e-6
        p=0.46
        pm=4.0e-17
        l=38.0e-6
        c=pm/(5.969436e5*rmax**3-4.545455e6*rmin**3)
        cfl=4.545455e6*rmin**3
        ifroru=1.790831e6*log(rmax)
c     B3
c     uniform pore size distribution
```

```
c      rmin=.1e-6
c      rmax=.26e-6
c      p=0.267
c      pm=6.0e-17
c      l=3.0e-6
c      cmm=1.0/(rmax-rmin)
c      c=pm/(cmm*(rmax**3-rmin**3)*(1.0/3.0))
c
c++++++++++++++++++++++++++++++++++++++++++++++++++++++++++++++++++++++
c     PRESSURE, HEAT FLUX AND STEAM/WATER PROPERTIES
c++++++++++++++++++++++++++++++++++++++++++++++++++++++++++++++++++++++
        print*, 'what is hfx'
        read*, hfx
c      hfx=6.14e4
        press=4.3e6
        pi=3.14159
        theta=pi/6
        gcst=462.0
        hfg=1638997+(5.0e6-press)*73200e-6
        dv=25.365-(5.262e-6*(5.0e6-press))
        dl=777.787+(20.971e-6*(5.0e6-press))
        t=263.9-(13.6e-6*(5.0e6-press))+273.0
        tcl=.598051+1.8e-8*(5.0e6-press)
        tcv=.054232-4.646e-9*(5.0e6-press)
        ml=.0001016+5.3e-12*(5.0e6-press)
        mv=.0000180-5.0e-12*(5.0e6-press)
        cp=5033.98-1.6371e-4*(5.0e6-press)
        nl=ml/dl
        nv=mv/dv
c
```

```
c++++++++++++++++++++++++++++++++++++++++++++++++++++++++++++++++
c     CONSTANTS TO EVALUATE VOLUMETRIC HEAT TRANSFER
      COEFFICIENT
c++++++++++++++++++++++++++++++++++++++++++++++++++++++++++++++++
        rst=1.0e-8
c
c++++++++++++++++++++++++++++++++++++++++++++++++++++++++++++++++
c     EVALUATION OF CHEN HEAT TRANSFER COEFFICIENT
c++++++++++++++++++++++++++++++++++++++++++++++++++++++++++++++++
        d=5.8e-3
c       d=.0759
        qual=.05
        mf=250.0
        pr=ml*cp/tcl
        re=mf*(1-qual)*d/ml
        xtt=((1-qual)/qual)**.875*(dv/dl)**.5*(ml/mv)**.125
        oxtt=xtt**(-1)
        if (oxtt .le. .1) then
                fxtt=1.0
        else
                fxtt=2.35*(.213+(1/xtt))**(.736)
        endif
        retp=re*(fxtt**1.25)
        sf=(1+((2.56e-6)*(retp**1.17)))**(-1)
        hmac=fxtt*.023*(tcl/d)*re**(.8)*pr**(.4)*1.0e-3
c
c================================================================
c     SETTING VARIABLES FOR FIRST DISTANCE STEP
c================================================================
        x(1)=0.0
```

```
      dx(1)=step
50    nll=dx(1)+x(1)
      if (nll .gt. l) then
            dx(1)=.9*dx(1)
            go to 50
      endif
      pl(1)=press
      stl=.02016+2.995e-9*(6.0e6-pl(1))
150   r(1)=rmax*ri
      pv(1)=pl(1)+(2.0*stl*cos(theta)/r(1))
175   tsk(1)=t*shf
      pwall=press*exp((1/t-1/tsk(1))*hfg/gcst)
      tclc=tcl*1.0e-3
      hfgc=hfg*1.0e-3
      cpc=cp*1.0e-3
      gc=9.81
      hmic=.00122*((tclc**.79*cpc**.45*dl**.49*gc**.25)/(stl**.5
     + *ml**.29*hfg**.24*dv**.24))*(tsk(1)-t)**.24*(pwall-press)**.75
     + *sf
      hc=(hmic+hmac)
      hc=hc*1.0e3
      q(1)=(tsk(1)-t)*hc
      if (q(1) .gt. hfx) then
            print*, 'q(1) > hfx, drop shf'
            go to 1100
      endif
      g(1)=(hfx-q(1))/hfg
      tcm=100*(.0423-1.37*tsk(1)*1.0e-5)
c     B4(7)
c      if (r(1) .ge. .06e-6) then
```

```
c            ps=1+((r(1)-.2e-6)/.14e-6)*.25
c       else
c            ps=.75+((r(1)-.06e-6)/.025e-6)*.75
c       endif
c       B4
         if (r(1) .ge. .09e-6) then
                  ps=1+((r(1)-.2296e-6)/.1396e-6)*.25
         else
                  ps=.75+((r(1)-.09e-6)/.055e-6)*.75
         endif
c       B3
c       uniform pore size distribution
c        ps=cmm*(r(1)-rmin)
         tcd=.5*((1-p)*tcm+p*(ps*tcl+(1-ps)*tcv))
         tp(1)=-q(1)/tcd
c_____________________________________________________________________
200      if (n .gt. 499) then
                  print*, 'n > 499'
                  go to 1100
         endif
c_____________________________________________________________________
         j=1
         if (n .eq. 1) then
                  gpl(j)=0.0
         else
                  gpl(j)=gp(n-1)
         endif
300      if (j .gt. 20) then
                  print*, 'j > 20'
                  fault='j > 20'
```

```
            write (unit=100, fmt=4000)fault
            go to 1100
        endif
        gql(j)=-gpl(j)*hfg
        gtp(j)=-gql(j)/tcd
c_____________________________________________________________________
c     dependent on dx; j doesn't change
350   tpl(j)=tp(n)-gtp(j)*dx(n)/2.0
        tskm(j)=tsk(n)-tpl(j)*dx(n)/2.0
        g(n+1)=g(n)-gpl(j)*dx(n)
        q(n+1)=q(n)-gql(j)*dx(n)
        gml(j)=g(n)-gpl(j)*(dx(n)/2.0)
        if ((gml(j) .lt. 0.0) .or. (g(n+1) .lt. 0.0)) then
            dx(n)=0.5*dx(n)
            print*, 'gml or g(n+1) < 0, drop dx'
            fault='gml or g(n+1) < 0, drop dx'
            write(unit=100,fmt=4000)fault
            go to 350
        endif
c_____________________________________________________________________
c     dependent on r (or rml); k changes
400   k=1
        if (rmldxc .gt. 1) go to 500
c     setting drl(k)
        if ((n .eq. 1) .and. (j .eq. 1)) then
            drl(k)=4.0e-2
        elseif (j .eq. 1) then
            drl(k)=dr(n-1)
        else
            drl(k)=drr
```

```
        endif
c       drl(k) set to drr from last iteration if j > 1
500     rml=r(n)-drl(k)*(dx(n)/2.0)
        if ((rml .gt. rmax) .or. (rml .lt. rmin)) then
                rmlc=rmlc+1
                if (rmlc .gt. 50) then
                        if (n .eq. 1) then
                                rmlc=0
                                dx(1)=step
                                ri=ri*.98
                                print*, 'rmlc > 50 and n=1'
                                fault='rmlc > 50 and n=1'
                                write(unit=100,fmt=4000)fault
                                go to 150
                        else
                                print*, 'rmlc > 50'
                                fault='rmlc > 50'
                                write(unit=100,fmt=4000)fault
                                go to 1100
                        endif
                endif
                print*, 'rml out of range drop dx'
                fault='rml out of range drop dx'
                write(unit=100,fmt=4000)fault
                dx(n)=0.50*dx(n)
                drl(k)=2.0*dr(n-1)
                rmldxc=rmldxc+1
                go to 350
        endif
c_____________________________________________________________________
```

```
c     rml okay, so evaluate all to do with rml and drl(k)
        rmldxc=1
c     B4(7)
c      if (rml .ge. .06e-6) then
c           f=1.785714e6
c           ps=1.0+.25*(rml-.2e-6)/.14e-6
c           cfu=5.952381e5*rml**3
c           ifrorl=1.166045e6*log(rml)
c      else
c           f=3.0e7
c           ps=.75+.75*(rml-.06e-6)/.025e-6
c           cfu=1.0e7*rml**3
c           ifrorl=3.0e7*log(rml)
c      endif
c      cf=cfu-cfl
c      ifror=ifroru-ifrorl
c     B4
        if (rml .ge. .09e-6) then
              f=1.790831e6
              ps=1.0+.25*(rml-.2296e-6)/.1396e-6
              cfu=5.969436e5*rml**3
              ifrorl=1.790831e6*log(rml)
        else
              f=1.363636e7
              ps=.75+.75*(rml-.09e-6)/.055e-6
              cfu=4.545455e6*rml**3
              ifrorl=1.363636e7*log(rml)
        endif
        cf=cfu-cfl
        ifror=ifroru-ifrorl
```

```
c     B3
c     uniform pore size distribution
c      ps=cmm*(rml-rmin)
c      f=cmm
c      cf=(1.0/3.0)*cmm*((rml**3)-(rmin**3))
c      ifror=cmm*(log(rmax)-log(rml))
        if (ifror .lt. 0) then
                print*, 'ifror < 0', ifror
                print*, rml, ifrorl
                print*, rmax, ifroru
                go to 1100
        endif
        write(unit=100,fmt=8000)rml,rmax, ifror
c     permeability and hrl relations
        dcl=(1.0/(dl*(ps**3)))+(1.0/(dv*((1.0-ps)**3)))
        dcv=(1.0/(dv*((1.0-ps)**2)))-(1.0/(dl*(ps**2)))
        pcml=2.0*stl*cos(theta)/rml
        hrd=(pcml/rml)-(((gml(j)**2)*f/(p**2))*dcl)
        hrn=(gpl(j)*gml(j)/(p**2))*(dcv)+(nl*gml(j)/(c*cf))+
     + (nv*gml(j)/(pm-c*cf))
        hrl=hrn/hrd
c_____________________________________________________________
c Now check the dr* by comparing drl to hrl and iterate
c_____________________________________________________________
c     impossible to have hrl negative
        if(((hrd .lt. 0.0) .or. (hrl .lt. 0.0)).and.(n .eq. 1))then
                print*, 'hrl < 0 on n=1, drop ri'
                fault='hrl < 0 on n=1, drop ri'
                write(unit=100,fmt=4000)fault
                ri=ri*0.98
```

```
                dx(1)=step
                go to 150
        endif
        if ((hrl .lt. 0.0) .or. (hrd .lt. 0.0)) then
                hrc(hrlc)=-hrl
                if ((hrlc .gt. 1) .and. (hrc(hrlc) .gt. hrc(hrlc-1)))
     +          then
                        print*, 'hrl more neg, increase shf'
                        fault='hrl more neg, increase shf'
                        write (unit=100,fmt=4000)fault
                        go to 1100
                endif
                dx(n)=0.9*dx(n)
                print*, 'drop dx for rmin, hrl neg'
                fault='drop dx for rmin, hrl neg'
                write(unit=100,fmt=4000)fault
                hrlc=hrlc+1
                if (hrlc .gt. 50) then
                        print*, 'hrlc > 50'
                        go to 1100
                endif
                go to 350
        endif
c_____________________________________________________________________
c       converging iteration for drl(k) and hrl
        if (drl(k) .gt. (1.0001*hrl)) then
c               write (unit=100,fmt=5000)n,j,k,drl(k),hrl,rml
                k=k+1
                if (k .gt. 100) then
                        print*, 'k > 100'
```

```
                fault='k > 100'
                write (unit=100, fmt=4000)fault
                go to 1100
            endif
            drl(k)=hrl
            go to 500
        endif
        if (drl(k) .lt. (0.9999*hrl)) then
c           write (unit=100,fmt=5000)n,j,k,drl(k),hrl,rml
            k=k+1
            if (k .gt. 100) then
                print*, 'k > 100'
                fault='k > 100'
                write (unit=100, fmt=4000)fault
                go to 1100
            endif
            drl(k)=hrl
            go to 500
        endif
c       fault='r converged to the values: '
c       write (unit=100, fmt=4000)fault
c       write (unit=100,fmt=5000)n,j,k,drl(k),hrl,rml
c       fault=' g values '
c       write (unit=100, fmt=4000)fault
        dpl=(((gml(j)*gpl(j))/(p**2*dl*ps**2)))-(gml(j)*nl/(c*cf))-
     + ((gml(j)**2*f*drl(k))/(p**2*dl*ps**3))
        pml=pl(n)+(dpl*(dx(n)/2))
        pmv=2.0*stl*cos(theta)/rml+pml
        tsml=(1/t-gcst/hfg*(log(pmv)-log(pl(1))))**(-1)
c       tskm < tsml, so no phase change
```

```
      if (tskm(j) .lt. tsml) then
            gpml=0.0
            go to 550
      endif
      aph=sqrt(2/pi)*gcst**(-3/2)*pmv*hfg**2/tsml**(5/2)
      cfr=5.6*(p**2)*sqrt(aph*tcl)*(pi/2.0-atan(sqrt(aph*rst/tcl)))
      aml=ps*ifror*cfr*(1.0/sqrt((rml+rmax)/2))
      gpml=aml*(tskm(j)-tsml)/hfg
      write(unit=100,fmt=7000)aml,tskm(j),tsml
550   if (gpl(j) .gt. (1.001*gpml)) then
            j=j+1
            gpl(j)=gpml
            drr=drl(k)
            go to 300
      elseif (gpl(j) .lt. (.999*gpml)) then
            j=j+1
            gpl(j)=gpml
            drr=drl(k)
            go to 300
      else
c     gp and dr values converged
            xml=x(n)+dx(n)/2
            fault='g and r values converged '
            write (unit=100, fmt=4000)fault
            write (unit=100,fmt=6000)n,j,k,gpl(j),gpml,g(n)
            x(n+1)=x(n)+dx(n)
            gp(n)=gpl(j)
            dr(n)=drl(k)
            tp(n)=tpl(j)
            r(n+1)=r(n)-dr(n)*dx(n)
```

```
                tsk(n+1)=tsk(n)-tp(n)*dx(n)
                tcl=.598051+1.8e-8*(5.0e6-pml)
                tcv=.054232-4.646e-9*(5.0e6-pmv)
                ml=.0001016+5.3e-12*(5.0e6-pml)
                mv=.0000180-5.0e-12*(5.0e6-pmv)
                hfg=1638997+(5.0e6-pmv)*73200e-6
                dv=25.365-(5.262e-6*(5.0e6-pmv))
                dl=777.787+(20.971e-6*(5.0e6-pml))
                nl=ml/dl
                nv=mv/dv
                tcm=100*(.0423-1.37*tsk(n+1)*1.0e-5)
                tcd=.5*((1-p)*tcm+p*(ps*tcl+(1-ps)*tcv))
                tp(n+1)=-q(n+1)/tcd
                dx(n+1)=dx(n)
                stl=.02016+2.995e-9*(6.0e6-pml)
                pl(n+1)=pl(n)+dpl*dx(n)
                pc(n+1)=2.0*stl*cos(theta)/r(n+1)
                pv(n+1)=pl(n+1)+pc(n+1)
        endif
c       now checking to match boundary conditions at x=l
        if (g(n+1) .gt. (0.001*g(1))) then
                if ((r(n+1) .lt. rmin) .or. (x(n+1) .ge. l))then
                        print*,'r < rmin or x(n+1)=l, shf increase'
                        print*, r(n+1), x(n+1), g(1), g(n+1)
                        print*, shf
                        go to 1100
                else
                        dx(n+1)=dx(n)
600               nll=x(n+1)+dx(n+1)
                        if (nll .gt. l) then
```

```
                print*, 'drop dx, nll'
                fault='drop dx, nll '
                write (unit=100, fmt=4000)fault
                dxc=dxc+1
                if (dxc .gt. 1000) then
                        print*, 'dxc .gt. 1000'
                        print*, n, x(n), g(n), r(n)
                        go to 1100
                endif
                dx(n+1)=.9*dx(n+1)
                go to 600
            endif
            n=n+1
            go to 200
        endif
    endif
c   g=0, check to see that x=l or r=rmin
    if ((r(n+1) .gt. rmin) .and. (x(n+1) .lt. (.99*l))) then
        print*, 'g=0, x(n+1) < l and r(n+1) > rmin, drop shf'
        print*, n, shf, g(n+1), x(n+1), l, r(n+1),rmin,tsk(n+1)
        fault= 'g=0, x(n+1) < l and r(n+1) > rmin, drop shf'
        write (unit=100, fmt=4000)fault
        go to 1100
    endif
    if (r(n+1) .eq. rmin) then
        rl=l-x(n+1)
        tcd=.5*((1-p)*tcm+p*tcv)
        tbd=tsk(n+1)+hfx*rl/tcd
        print*, 'dried out at x=', x(n+1)
    else
```

```
            rl=0.0
            tbd=tsk(n+1)
        endif
        dt=tbd-t
        hd=q(1)/hfx
        print*, 'done', n
        print*, 'super heat factor', shf
        print*, 'dried out length', rl
        print*, 'radius', r(n+1)
        print*, 'temperature at n', tsk(n+1)
        print*, 'delta temperature', dt
        print*, 'amount of heat by surface', hd
1100    close(unit=100)
1200    end
```

This file contains a list of the variables used in the program deposit.for.
It briefly states the meaning of the variable and implies its function.

---

real(1:500)
these variables hold the values of the parameters once the equations converge

---

dr change in r (radius)
dx change in x (position)
g mass flux
gp g prime (derivative of mass flux)
q heat flux
r radius
tp temperature prime (derivative of temperature)
tsk temperature of skeleton
x position
pc capillary p
pl p of liquid
pv p of vapor

---

real(1:20)
these variables hold the values of the parameters used in the convergence loop, they are dimensioned by j except drl, which is dimensioned by k

---

drl change in r of the inner loop
gml mean g of the outer loop

gpl g prime of the outer loop

gql gradient of q of outer the loop

gtp gradient of temperature of the outer loop

tskm mean skeletal temperature of the outer loop

tpl temperature prime of the outer loop

---

real

these variables hold the values of parameters in the convergence loop

---

aml mean volumetric heat transfer coefficient of the loop

cf F(r) (see description of model)

cfl lower bound of cf

cfu upper bound of cf

cfr coefficient used in evaluation of aml

dcl density coefficient of liquid used in evaluation of hrl

dcv density coefficient of vapor used in evaluation of hrl

dpl change in p of the liquid of the loop

drr change in r used in the last iteration loop, passed on to new gql

gpml mean g prime of the loop

hrd denominator in the evaluation of hrl

hrl hydrodynamic evaluation of dr, then compared to drl for iteration

hrn numerator in the evaluation of hrl

ifror integral of f(r)/r (see description of model)

ifrorl lower bound of ifror

ifroru upper bound of ifror

nll to determine if the dx increment exceeds the length of the deposit

pcml mean capillary p of the loop

pml mean p of liquid of the loop

pmv mean p of vapor of the loop

ps pore size distribution evaluated at rml

rml mean r of the loop

stl surface tension of the liquid

tcd thermal conductivity of the deposit

tcm thermal conductivity of the magnetite

tsml mean saturation temperature of the loop

---

real

this variable is used to match boundary conditions

---

hrc to obtain the final value of r, the variable hrl is evaluated and assigned to hrc. If after the next iteration, hrc is less than the new value of hrl, heat flux must be changed. hrc is dimensioned by hrlc,(1:50)

ri initial value of r; multiplies rmax

---

real

these variables hold the values of the deposit parameters

---

c coefficient for relative permeability (multiplies absolute permeability by cf)

cmm for uniform pore size distribution, denominator for c

f f(r) pore size distribution

l thickness of the deposit

p porosity

pm permeability

rmax maximum radius

rmin minimum radius

---

real

these variables hold the values of the steam and water parameters

---

aph voulumetric heat transfer coefficient at phase change

cp specific heat of vaporization

dl density of liquid

dv density of vapor

hfg latent heat of vaporization

ml viscosity of liquid

mv viscosity of vapor

nl kinematic viscosity of liquid

nv kinematic viscosity of vapor

rst radius of surface tension interaction

t saturation temperature at pressure of the boundary convective flow

tcl thermal conductivity of liquid

---

real

these variables hold the values of the heat addition and flow/Chen

correlation parameters

---

cpc cp in units for Chen correlation

d hydraulic diameter of the setup

fxtt function of xtt

hc heat transfer coefficient evaluated by Chen model

hfgc hfg in units for Chen correlation

hfx heat flux

hmac macroscopic component of hc

hmic microsopic component of hc

mf mass flux

oxtt reciprocal of xtt

pr prandtl number

pwall saturation p corresponding to twall

qual quality

re reynolds number

sf supression factor

tclc tcl in units for Chen correlation

twall temperature of the wall

xtt Martinelli parameter

---

real

these variables hold the values of constants or user inputs

---

gc gravitational constant

gcst gas constant

pi pi

step distance step

---

real

these variables hold the values at the final conditions

---

dt the difference between t and tbd

hd the fraction of the heat flux that is transferred by hc

rl the dried out portion of the deposit l

tbd temperature of the deposit at the largest x position that
contains liquid

---

integer

these variables serve as counters in the loop iterations

loop

---

hrlc counts the number of reductions of dx to evaluate rmin, ends loop
with an error signal, also dimensions hrc

j outer iteration loop, choice of gql

k inner iteration loop, choice of drl

n number of distance steps taken, dimensions all the variables (1:500)

rmlc counts the number of reductions of dx to rml when nearing rmin,
ends loop with error signal

---

character

these variables write to the ouput file updating the status of the code

---

fault message to the ouput file concerning the change in present conditions

Appendix B

Calculation of the Maximum Pressure Drop in the ID Experiment

The pressure drop in the ID experiment was evaluated with the Thom correlation [T-1] to ensure the validity of the assumption that T_b remained costant along the length of the test section.

The equation for the pressure drop involves the frictional, acceleration and gravitational terms expressed as the first, second and third terms on the RHS of equation B-1, respectively:

$$\Delta P = \frac{f_{lo} G^2 L}{D^2 \rho_l} r_3 + \frac{G^2}{\rho_l} r_2 + L \rho_l g_c \cos\beta r_4, \qquad \text{(B-1)}$$

where f_{lo}, L, β, r_2, r_3 and r_4 are the liquid only friction factor, length of the setup, angle the setup makes with the vertical and the Thom coefficients for acceleration, friction and gravity, respectively. Since the setup was vertical, β=0. The friction factor was determined by the Blasius relation for one phase liquid flow in a smooth tube:

$$f_{lo} = 0.316\, Re^{-0.25}. \qquad \text{(B-2)}$$

The maximum pressure drop of 6.9 kPa occurred with the largest mass flux and exit quality of 273 kg/m^2-s and 0.30, respectively. This pressure drop corresponds to a 0.09 °C change in saturation temperature along the length of the u-tube. The approximation of constant T_b was therefore valid.

Appendix C

Derivation of Equation 5.15

In section 5.3.3.1, several substitutions were made before the final form of the hydrodynamic relation of countercurrent liquid and vapor flow in porous media, equation 5.15, was obtained. The following outlines the details of the derivation.

Equation 5.9 relates the capillary pressure to R*, the radius defining the boundary between liquid and vapor phases in the deposit:

$$P_c(x)=P_v(x)-P_l(x)=\frac{2\sigma\cos\theta}{R^*(x)}. \tag{5.9}$$

The liquid and vapor equations of motion are:

$$\frac{\rho_l}{\Pi^2}v_l\frac{dv_l}{dx}=-\frac{dP_l}{dx}-\frac{\mu_l}{K_l}v_l, \tag{5.10}$$

$$\frac{\rho_v}{\Pi^2}v_v\frac{dv_v}{dx}=-\frac{dP_v}{dx}-\frac{\mu_v}{K_v}v_v. \tag{5.11}$$

Differentiation of equation 5.9 yields:

$$\frac{dP_c}{dx}=-\frac{2\sigma\cos\theta}{(R^*)^2}\frac{dR^*}{dx}. \tag{C-1}$$

Subtracting equation 5.11 from 5.10 yields:

$$\frac{dP_c}{dx}=\frac{\rho_l}{\Pi^2}v_l\frac{dv_l}{dx}-\frac{\rho_v}{\Pi^2}v_v\frac{dv_v}{dx}+\frac{\mu_l}{K_l}v_l-\frac{\mu_v}{K_v}v_v. \tag{C-2}$$

Substitution of equation C-1 into C-2 and rearranging yields:

$$\frac{\rho_l}{\Pi^2}v_l\frac{dv_l}{dx}-\frac{\rho_v}{\Pi^2}v_v\frac{dv_v}{dx}=-\frac{2\sigma\cos\theta}{(R^*)^2}\frac{dR^*}{dx}-\frac{\mu_l}{K_l}v_l+\frac{\mu_v}{K_v}v_v. \tag{5.12}$$

The liquid and vapor velocities are expressed by:

$$v_l(x) = -\frac{G(x)}{\rho_l \varphi(R^*)}, \tag{5.13}$$

$$v_v(x) = \frac{G(x)}{\rho_v (1-\varphi(R^*))}, \tag{5.14}$$

where $\varphi(R^*)$ is the cumulative pore size distribution of the deposit evaluated at $r=R^*$. Differentiation of equations 5.13 and 5.14 result in equation C-3 and C-4, respectively:

$$\frac{dv_l}{dx} = -\frac{dG/dx}{\rho_l \varphi(R^*)} + \frac{G(x) f(R^*)}{\rho_l \varphi^2(R^*)} \frac{dR^*}{dx}, \tag{C-3}$$

$$\frac{dv_v}{dx} = \frac{dG/dx}{\rho_v (1-\varphi(R^*))} + \frac{G(x) f(R^*)}{\rho_v (1-\varphi(R^*))^2} \frac{dR^*}{dx}. \tag{C-4}$$

The derivative of $\varphi(R^*)$ with respect to r yields $f(R^*)$, the incremental pore size distribution of the deposit evaluated at $r=R^*$.

Substitution of equations 5.13, 5.14, C-3 and C-4 into 5.12 and rearranging yields:

$$\frac{dR^*}{dx}\left\{\frac{2\sigma\cos\theta}{R^*(x)^2} - \frac{G^2(x) f(R^*)}{\Pi^2}\left(\frac{1}{\rho_l \varphi^3(R^*)} + \frac{1}{\rho_v (1-\varphi(R^*))^3}\right)\right\} = \frac{G(x)}{\Pi^2}\frac{dG}{dx} * \left[\frac{1}{\rho_v (1-\varphi(R^*))^2} - \frac{1}{\rho_l \varphi^2(R^*)}\right] + \frac{\nu_l G(x)}{CF(R^*)} + \frac{\nu_v G(x)}{K - CF(R^*)}, \tag{5.15}$$

where $F(R^*)$ is equivalent to:

$$F(R^*) = \int_{r_{min}}^{R^*} r^2 f(r) dr, \tag{5.16}$$

and C is a constant relating the permeability of the deposit, K, to the average value of r^2:

$$K = C \int_{r_{min}}^{r_{max}} r^2 f(r) dr. \tag{5.17}$$

C can be found by comparing the measured permeability to the value of the integral on the RHS of equation 5.17. K_l and K_v are expressed by equations 5.18 and 5.19, respectively:

$$K_l \varphi(R^*) = C \int_{r_{min}}^{R^*} r^2 f(r) dr, \tag{5.18}$$

$$K_v (1 - \varphi(R^*)) = C \int_{R^*}^{r_{max}} r^2 f(r) dr. \tag{5.19}$$

Appendix D

Experimental and Theoretical Values of Deposit Thermal Conductivity as a Function of Porosity

Subcooled forced convection measurements were taken to evaluate the thermal conductivity of the deposit, k_d, when saturated with subcooled liquid, as described in Chapter 6. The results are plotted in Figure D-1 along with the values predicted by equation 6.2, and the values of liquid and magnetite thermal conductivity. The term, k_d, is expressed by:

$$k_d = (k_l \Pi + [1 - \Pi] k_m)/2, \qquad (6.2)$$

where k_l, k_m and Π are the thermal conductivity of the liquid, magnetite and the deposit porosity, respectively.

This expression represents one-half the value of the liquid and magnetite conductivities in parallel. This approach was adopted, as the data from this study and that taken by Turner agree reasonably well with the calculations [T-4]. Data were taken at porosities of 0.46 and 0.60 in this study and from 0.20 to 0.30 by Turner. Due to the limited amount of data, it is uncertain if equation 6.2 applies to all porosities ranging from 0 to 1. Certainly, at a value of 0 and 1, k_d is equivalent to the thermal conductivity of the magnetite (3.69 W/m-K) and liquid (0.69 W/m-K), respectively. Equation 6.2 predicts one-half these values, and therefore, equation 6.2 is not valid at the limits of porosity.

However, it was determined that the boiling heat transfer model does not depend on porosity (Figure 6.), and porosities of real steam generator u-tube deposits range from 0.20 to 0.60, a range over which equation 6.2 has been validated. Therefore, it is presumed that the use of equation 6.2 at all values of porosity does not hinder the accuracy of the model.

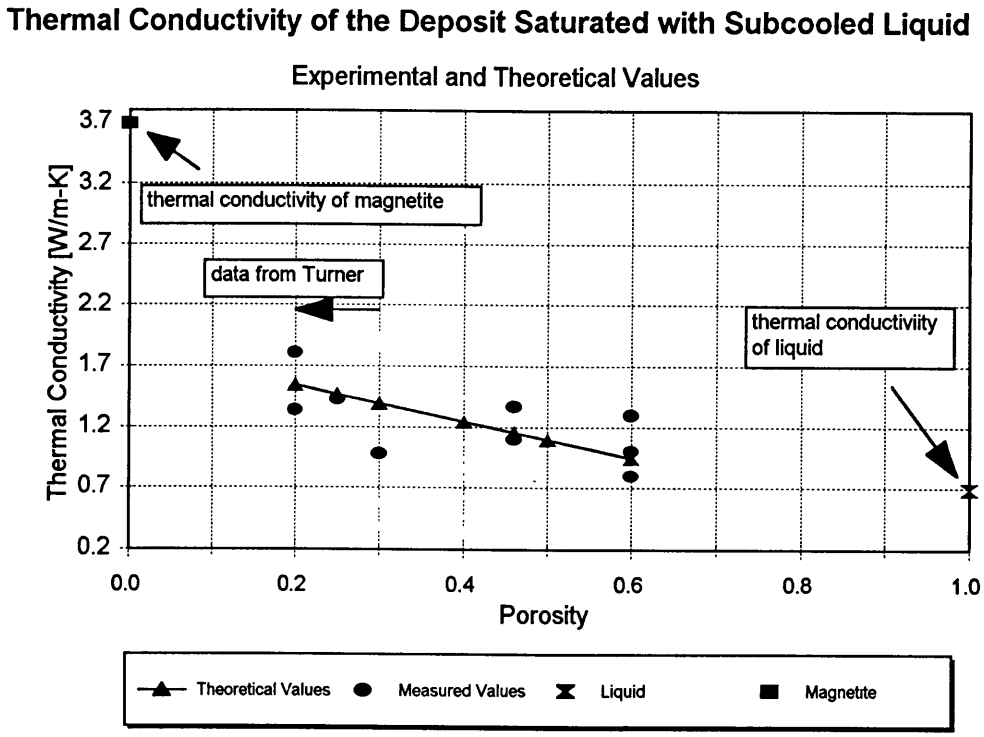

Figure D-1: Experimental and Theoretical Values of Deposit Thermal Conductivity when Saturated with Subcooled Liquid Versus Porosity